ULTRAFAST AND INCOHERENT RAMAN STUDIES OF OPTICAL PHONONS OF DIFFERENT SYMMETRIES IN Sb, Bi, Bi_2Te_3 AND Bi_2Se_3

by

Jingjing Li

A dissertation submitted in partial fulfillment
of the requirements for the degree of
Doctor of Philosophy
(Physics)
in The University of Michigan
2012

Doctoral Committee:

Professor Robert D. Merlin, Chair
Professor Paul R. Berman
Professor Theodore B. Norris
Professor Duncan G. Steel
Associate Professor Çagliyan Kurdak

Water from an ample source

flows incessantly day and night,

proceeds forward only after the hollows are filled,

and finally embraces the sea.

— Mentius

源泉混混

不舍昼夜

盈科而后进

放乎四海

— 孟子

To my parents,

Junli Huang and Bin Li

ACKNOWLEDGEMENTS

The journey to getting a PhD is long. Now when I look back, this passage is glittering with numerous vivid and precious moments spent with the people who helped me. It is these experiences, together with the knowledge and skills harvested along the way, that makes the study in graduate school a really memorable and worthwhile one.

I was very fortunate to meet my advisor, Professor Roberto Merlin. I would like to thank him for offering me the chance to work in his group, and for his continuous support and encouragement during every phase of my PhD study. He is always there to help, with infinite patience and high spirit. My understanding and intuition of physics has been deepened significantly during my PhD study by his enlightening explanations and penetrating interpretations. What is more, I learnt not only knowledge from him, but also the right approach and attitude for solving problems not limited to research, which has benefited and will surely continue to benefit me greatly in my future life. I am also indebted to Professor David Reis and Professor Stephen Fahy for the inspiring discussion in both experiments and theories about our collaborative work in semimetals. I want to thank Professor Çagliyan Kurdak for his advice when I was looking for a research group and his generous help in my job searching process. I also want to thank other members of my defense committee, Professor Paul Berman, Professor Duncan Steel and Professor Theodore Norris for valuable discussions and suggestions about my research. I really appreciate Professor Carl Akerlof's encouragement about my teaching ability, and his help in my job searching. I am grateful to Professor Ctirad Uher for helpful discussions about semimetals and topological insulators, as well as the nice samples he provided.

I would like to thank all the group members, for their talented, friendly and witty minds, which made working in this group such a pleasant experience. I am grateful to Andrea Bianchini, who has influenced me a lot during more than five years, for his help in almost every aspect in the lab. I really appreciate Paul Jacobs' guidance and training when I first joined the group. Thanks to Ilya Vulgmeyster for his help with monochromators, profilometers, leak detectors and sample preparation. Thanks to Jessica Ames for her help with the laser systems, as well as the interesting conversations that lighted up the life in a lab without windows. Thanks to my collaborator, Jian Chen, for his kind support and helpful discussions in the semimetal experiment. Thanks to Prashant Padmanabhan for his instructions and tips about operating an OPA. Thanks to Alex Toulouse for his assistance with SPEX and his suggestions on presentations. Thank to Steve Young for his help with thin film fabrication and inspiring discussion about topological insulators. Thanks to Ibrahim Boulares for his help with the chiller for the Argon laser and Raman spectrometer. Thanks to Ben Isaacoff for his assistance with optical microscope imaging. Also thanks to other group members Greg Affeldt and Meredith Henstridge. Special thanks go to native speakers in the group who meticulously proof-read my thesis and personal statements, and kindly provided daily language consultation. I also owed much help from Dong Sun, who kept giving me practical advices as a senior fellow, Lei Jiang for his suggestions on programming, Vladimir Stoica for useful technical tips, Mariano Trigo for his instructions on telescopes and cryostats, Meng Cui for his guidance at the beginning of my research, Cynthia Aku-Leh and Daimian Wang for their advices on career opportunities, and Jimin Zhao for his view on being a motivated researcher. I would also like to thank Steve Katnik for taking good care of the lasers.

At the same time, I am thankful to my friends in Ann Arbor, who have made the life here colorful and heartwarming. I want to acknowledge Yu Jin, who is not only a very capable travel companion, but more a friend indeed who I could turn to in difficult times.

Appreciations also go to Yiying Zhao, Hailing Cheng, Chenxi Shen, Chun Xu, Yuxing Yun, Wei Wu, Nengfeng Zhou, Junyi Zhang, Xuhuai Zhang, Bo Zhang, Guan Huang, and other people whom I have not mentioned here, for all the happiness they brought to me.

Finally, I want to express my greatest gratitude to my parents, Junli Huang and Bin Li, for their love, trust, encouragement and understanding. They taught me the importance of diligence and appreciation, and most importantly, how to be a happy person in the first place. They are always my vital source of strength and reassurance.

TABLE OF CONTENTS

LIST OF FIGURES

Figure

CHAPTER 1

Introduction

Since its discovery in the 1928 by C. V. Raman, Raman scattering has found increasingly wide applications that allow for better understanding of fundamental material properties thanks to the development of light sources and detection techniques. With sunlight as the source, and his eyes as the detector, Raman was the first to successfully observe the sideband pair of the incident frequency in light scattered by several liquids [1,2]. However, due to the low intensity of the scattered radiation, the study of light scattering proceeded at a slow pace until the invention of continuous wave lasers in the 1960's. The laser served as a monochromatic, intense, highly polarized, highly collimated light source and quickly replaced the traditional mercury arcs [1,2]. These powerful new sources produced a renaissance of light-scattering studies [2]. At the same time, photoelectric detection techniques superseded the photographic recording methods with the much higher sensitivity of photomultipliers compared to photographic plates [1,3]. The introduction of double monochromators, triple monochromators and holographic gratings further improved the Raman instruments with their higher resolution and efficient stray light rejection [1,3]. Continuously tunable dye lasers and later Ti:sapphire solid state lasers offered the possibility to characterize resonance Raman scattering in even more details, as well as to discriminate unfavorable fluorescence [2]. Charge-coupled devices (CCDs) have also been used increasingly since the early 1990's owing to their high quantum efficiency, low dark signal and multichannel advantage, greatly reducing the time for signal collection [1,4]. All these advances constitute the current state-of-the-art Raman instrumentation.

The advent of various lasers also allowed the extension of Raman scattering into the field of coherent Raman spectroscopy (CRS) [5]. Coherent Raman spectroscopy has advantages over standard incoherent Raman spectroscopy (RS) due to its high conversion efficiency, spectral and spatial discrimination against fluorescence and low incident average power [6]. With the introduction of a theoretical framework for nonlinear optics in 1965 [7], stimulated Raman spectroscopy (SRS) [8], coherent antistokes Raman spectroscopy (CARS) and Raman induced Kerr effect spectroscopy (RIKES) [9] were subsequently developed in the mid 1960's based on the intense laser sources. This field expanded further with the availability of tunable dye laser sources in the early 1970's [6]. CARS has nowadays become one of the most powerful tools available for investigations in physics, chemistry and biology [10]. In the meanwhile, development of ultrafast lasers provided researchers with a novel, time-resolved perspective to study coherent Raman processes. Progress in generating picosecond pulses in the late 1960's enabled the investigations of dynamics of vibrational relaxation processes in liquids and solids, a technique referred to as transient stimulated Raman scattering (TSRS) [11]. The sub-100fs output of the colliding pulse mode-locked (CPM) laser developed in 1981 [12] and later the 60fs pulsed output of Ti:sapphire arriving in 1991 [13] finally granted adequate time resolution for the sub-cycle observation of lattice vibrations, a method called impulsively stimulated Raman scattering (ISRS) [11]. Pump-probe spectroscopy is now one of the most widely used ultrafast spectroscopies to study ISRS.

Research presented in this dissertation is based on both standard spontaneous Raman spectroscopy and pump-probe spectroscopy. Despite the exhaustive studies of RS and extensive application of pump-probe spectroscopy to studying many materials including semiconductors [14], high T_c superconductors [15] and semimetals [16], discussions and discoveries concerning the various forms and origins of the driving forces for coherent phonons in different materials has been an active field for a long time [11,17-19]. One of the open questions concerns the generation mechanism of coherent

optical phonons in opaque materials such as Sb and Bi. Different from the impulsive form in transparent materials, driving forces in opaque materials are of a displacive nature [20]. Previous theoretical and experimental work proved that the ratio between the initial amplitudes of two modes in the same material in stimulated Raman scattering is the same as the ratio between corresponding Raman scattering cross sections in spontaneous Raman scattering [21,22]. In Chapter 4, I will show through ISRS experiments on Sb and Bi that the A_{1g} and E_g modes have different temperature dependent behaviors, and that the ratio increases with temperature, a feature different from the case in RS. The discrepancy implies that the driving force of E_g symmetry has a lifetime around 10fs, a time much shorter than that of the A_{1g} force, which is usually a few picoseconds. The ultrashort E_g lifetime is attributed to the fast redistribution of carriers between equivalent **k** points in the Brillouin zone, which destroys the E_g symmetry. The contribution of my experimental work here adds to the existing theoretical framework that the lifetime of the driving force influences the initial amplitude of coherent phonons. In Chapter 5, I will further extend this topic to the case of comparison between two modes of A_{1g} symmetry. By performing temperature dependent ISRS and RS experiments on Bi_2Te_3 and Bi_2Se_3, I was able to validate that the driving forces for the two A_{1g} modes have similar lifetimes, both much longer than the periods of coherent phonons that they excite. Lifetimes of the E_g driving forces similar with the ones in Sb and Bi were obtained, confirming the conclusion about the ultrashort lifetime of the E_g symmetry.

Phenomena under high laser fluences have become a popular topic in recent years due to the capability of high fluence radiation to produce high density plasma and photo-induced transient phase transitions [23-26]. In the second part of Chapter 4, I will discuss my research on the fluence dependent behaviors of coherent A_{1g} and E_g modes in Sb. At high fluences, both modes manifest time dependent frequencies, a phenomenon usually called “chirped phonon”, which is attributed to the screening by a diffusive

photoexcited plasma [27]. The results also manifest nonlinear growth of the phonon amplitudes and increased lattice anharmonicity. These experimental data provide useful information for future theoretical work in understanding anisotropic lattice-carrier interactions and lattice-radiation interactions in uniaxial crystals.

Bi_2Te_3 and Bi_2Se_3 have been receiving increasing interest recently due to their peculiar property as topological insulators. These materials have a narrow bandgap in the bulk and metallic states on the boundary, protected by time-reversal symmetry [28]. In addition to their fundamental interest, topological insulators are predicted to be useful for applications involving spintronics and quantum computation [28]. I will present my attempts to fabricate and characterize ultrathin Bi_2Te_3 films in Chapter 5 using mechanical exfoliation, optical microscopy, AFM and Raman spectroscopy. Since the thinnest pieces found were 10nm, an analysis based on transfer matrices was performed to aid in the identification of pieces below 10nm. In the Raman experiments, an additional peak was found which may be related to the breaking of symmetry in ultrathin films.

References

[1] J. R. Ferraro, K. Nakamoto and C. W. Brown, *Introductory Raman Spectroscopy* (Academic Press, San Diego, CA, 2003)

[2] W. Hayes and R. Loudon, *Scattering of Light by Crystals* (John Wiley & Sons, Inc., New York, 1978).

[3] B. Schrader, *Infrared and Raman Spectroscopy, Methods and Applications*, edited by B. Schrader (VCH Verlagsgesellschaft mbH, Weinheim, 1995).

[4] R. L. McCreery, in *Modern Techniques in Raman Spectroscopy*, edited by J. J. Laserna (John Wiley & Sons, Inc., New York, 1996).

[5] H. Vogt, in *Light Scattering in Solids II*, edited by M. Cardona and G. Güntherodt, Topics in Applied Physics Vol. 50 (Springer, Berlin, 1982).

[6] R. F. Begley, A. B. Harvey and R. L. Byer, Applied Physics Letters, **25**, 387 (1974).

[7] N. Bloembergen, *Nonlinear Optics* (W. A. Benjamin, Reading, Massachusetts, 1965).

[8] N. Bloembergen, American Journal of Physics **35**, 989 (1967).

[9] P. D. Maker, R. W. Terhune, Physical Review **137**, A801 (1965).

[10] A. M. Zheltikov, Journal of Raman Spectroscopy **31**, 653 (2000).

[11] R. Merlin, Solid State Communications **102**, 207 (1997).

[12] R. L. Fork, B. I. Greene and C. V. Shank, Applied Physics Letter **38**, 671 (1981).

[13] D. E. Spence, P. N. Kean and W. Sibbett, Optics Letters **16**, 42 (1991).

[14] G. C. Cho, W. Kütt and H. Kurz, Physical Review Letters **65**, 764 (1990).

[15] J. M. Chwalek, C. Uher, J. F. Whitaker, G. A. Mourou and J. A. Agostinelli, Applied Physics Letters **58**, 980 (1991).

[16] T. K. Cheng, S. D. Borson, A. S. Kazeroonian, J. S. Moodera, G. Dresselhaus, M. S. Dresselhaus and E. P. Ippen, Applied Physics Letters **57**, 1004 (1990).

[17] G. A. Garrett, A. G. Rojo, A. K. Sood, J. F. Whitaker and R. Merlin, Science **275**, 1638 (1997).

[18] J. K. Wahlstrand and R. Merlin, Physical Review B **68**, 054301 (2003).

[19] M. Först, C. Manzoni, S. Kaiser, Y. Tomioka, Y. Tokura, R. Merlin and A. Cavalleri, Nature Physics **7**, 854 (2011).

[20] T. K. Cheng, J. Vidal, H. J. Zeiger, G. Dresselhaus, M. S. Dresselhaus, and E. P. Ippen, Applied Physics Letters **59**, 1923 (1991).

[21] T. E. Stevens, J. Kuhl, and R. Merlin, Physical Review B **65**, 144304 (2002).

[22] G. A. Garrett, T. F. Albrecht, J. F. Whitaker, and R. Merlin, Physical Review Letters **77**, 3661 (1996).

[23] A. Cavalleri, Cs. Tóth, C. W. Siders, J. A. Squier, F. Ráksi, P. Forget and J. C. Kieffer, Physical Review Letters **87**, 237401 (2001).

[24] C. W. Siders and A. Cavalleri, Science **300**, 591 (2003).

[25] C. Kübler, H. Ehrke, R. Huber, R. Lopez, A. Halabica, R. F. Haglund, Jr. and A. Leitenstorfer, Physical Review Letters **99**, 116401 (2007).

[26] H. Ichikawa, S. Nozawa, T. Sato, A. Tomita, K. Ichiyanagi, M. Chollet, L. Guerin, N. Dean, A. Cavalleri, S. Adachi, T. Arima, H. Sawa, Y. Ogimoto, M. Nakamura, R. Tamaki, K. Miyano and S. Koshihara, Nature Materials 10, 101 (2011).

[27] S. Fahy and D. A. Reis, Physical Review Letters **93**, 109701 (2004).

[28] M. Z. Hasan and C. L. Kane, Reviews of Modern Physics **82**, 3045 (2010).

CHAPTER 2

Theories on Light Scattering by Optical Phonons

Phonons are quasiparticles which characterize the elementary excitation of lattice vibrations in a crystal. They influence the optical, electrical, thermal properties of a solid [1,2,3]. For example, many materials show strong absorption or reflection of light in the infrared spectral region due to the interaction with infrared active phonons [2,3]. Another example, phonons are known as an important source for the heat capacity and heat conductivity of an insulator or semiconductor [1,3]. Phonons can be investigated by various techniques such as light scattering, infrared absorption, neutron scattering, X-ray scattering, etc [4,5]. The works in this dissertation focus on light scattering by optical phonons.

This chapter reviews the mathematical derivation of phonon modes as well as theoretical foundation underlying two commonly used optical detection techniques of optical phonons. Section 2.1 first introduces the physical pictures of acoustic and optical phonon modes in a simple diatomic chain. Then generalization to a three-dimensional crystal with n atoms in each unit cell is made. Section 2.2 explains the theoretical base of spontaneous Raman scattering (RS) from macroscopic and microscopic perspectives. In section 2.3, theories for impulsively stimulated Raman scattering (ISRS) are presented. In contrast to RS, ISRS involves two distinct Raman tensors, which are derived in this section using the electron density matrix. A summary is given in section 2.4.

2.1 Normal modes in a crystal

A crystal is composed of periodically arranged groups of atoms which fluctuate around their equilibrium sites. Despite the variety of atomic forces (metallic, ionic, valent, van der Waals) that hold the crystal together, the environment surrounding a single atom can always be portrayed as a potential well. To the second order expansion of the potential well around the atomic equilibrium position, an approach usually called the harmonic approximation, the motion of an atom can be modeled by a harmonic oscillator. In a crystal, the behaviors of a collection of these oscillators are coupled with each other. By transforming from atom coordinates to phonon coordinates, a more mathematically and physically convenient expression can be achieved, in the form of a set of independent normal modes describing the collective atomic movements. With its motion decoupled from others, each normal mode is individually formulated and quantized. A phonon is an energy quantum of these normal modes for lattice vibrations.

2.1.1 Phonon modes in a one-dimensional diatomic chain

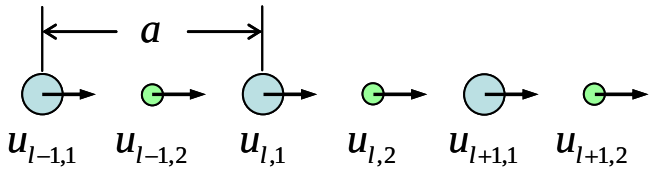

Figure 2.1. A diatomic chain with masses M and m. The size of a unit cell is a and the force constant between neighboring atoms is k. Note that the length and direction of the arrows do not stand for the actual magnitudes of displacements.

Consider a one-dimensional diatomic chain composed of N unit cells, each having two atoms with mass M and m, as shown in Fig. 2.1. The distance between neighboring unit cells is a and the spring constant is k. Newton's equations of motion for the two atoms in the l th cell are

$$\begin{aligned} M\ddot{u}_{l,1} &= k(u_{l,2} - u_{l,1}) - k(u_{l,1} - u_{l-1,2}) \\ m\ddot{u}_{l,2} &= k(u_{l+1,1} - u_{l,2}) - k(u_{l,2} - u_{l,1}) \end{aligned} \tag{2.1}$$

where $u_{l,1}$ is the displacement of the atom with mass M in the lth cell from its equilibrium position, and $u_{l,2}$ is the displacement of the atom with mass m. Plane wave solutions to these equations are

$$\begin{aligned} u_{l,1} &= Q_1(q)e^{i(qla-\Omega t)} \\ u_{l,2} &= Q_2(q)e^{i(qla-\Omega t)} \end{aligned} \tag{2.2}$$

where q is the wavevector and Ω is the frequency. Substituting Eq. (2.2) into Eq. (2.1), I have

$$\begin{aligned} (M\Omega^2 - 2k)Q_1(q) + k(1+e^{-iqa})Q_2(q) &= 0 \\ k(1+e^{iqa})Q_1(q) + (m\Omega^2 - 2k)Q_2(q) &= 0 \end{aligned} \tag{2.3}$$

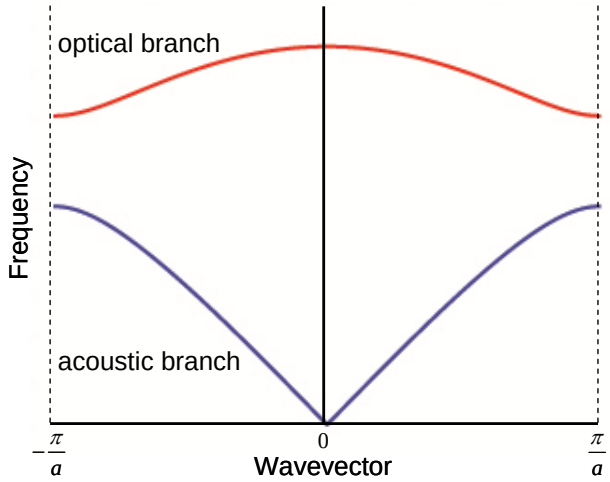

Figure 2.2. Dispersion curves for optical and acoustic branches in the first Brillouin zone.

To get non-trivial solutions to the linear equations, I set the determinant of the coefficients to zero

$$\begin{vmatrix} M\Omega^2 - 2k & k(1+e^{-iqa}) \\ k(1+e^{iqa}) & m\Omega^2 - 2k \end{vmatrix} = 0 \tag{2.4}$$

Solve the equation and get

$$\Omega_{\pm}^2 = k\frac{M+m}{Mm}\left\{1 \pm \left[1 - \frac{4Mm}{(M+m)^2}\sin^2\left(\frac{qa}{2}\right)\right]^{1/2}\right\} \tag{2.5}$$

$$-\frac{\pi}{a} < q \le \frac{\pi}{a} \quad \text{and} \quad q = \frac{2\pi}{a}\frac{h}{N} \qquad h \text{ is an integer}$$

The second expression about q above is required by the periodic boundary condition of the diatomic chain. Solutions given by Eq. (2.4) depict dispersion relations of two phonon branches. The one given by Ω_- is called the acoustic phonon branch and the one given by Ω_+ is called the optical phonon branch. There are in total N modes on each branch within the first Brillouin zone. When N becomes very large, those discrete modes can be treated as continuous. Fig. 2.2 is an example of the dispersion curves in the first Brillouin zone.

Due to the requirement of phase matching, light usually interacts with phonons at the long wavelength limit where $q \approx 0$. For the acoustic branch, $\Omega_- \approx a\sqrt{\frac{k}{2(M+m)}}q$ and $\left[\frac{Q_1(0)}{Q_2(0)}\right]_- \approx 1$, which means that both atoms in the same unit cell move with the same amplitude and phase [2]. Note that under this limit, the dispersion relation is almost linear, as seen from the zone center in Fig. 2.2, and the slope corresponds to the sound velocity in a solid. For the optical branch, $\Omega_+ \approx \sqrt{\frac{2k(M+m)}{Mm}}$ and $\left[\frac{Q_1(0)}{Q_2(0)}\right]_+ \approx -\frac{m}{M}$. This describes the scenario when the two atoms are oscillating out of phase while keeping the center of mass of the unit cell unchanged [2]. The optical phonon can hence carry a dipole moment and couple to infrared radiation. The dispersion curve is almost flat at the zone center, as seen from Fig. 2.2.

2.1.2 Phonon modes in a three-dimension crystal

Consider a crystal with N unit cells, each with n atoms inside. An equation similar to Eq. (2.1) can be written to describe the motion of each atom, and there are in

total $3n$ linear equations. Using solutions having the same form as Eq. (2.2), a secular function like Eq. (2.4) is solved to get the $3n$ branches which depict dispersion relations in three dimensions.

Here, I approach the problem from another aspect by starting from the Hamiltonian of the system since the result can conveniently lead to the quantization of lattice waves. The procedure follows relevant chapters in Ref. [2] and Ref. [6].

The potential energy of the entire crystal can be expanded as a function of the small displacement of each atom as

$$U = U_0 + \sum_{l}^{N}\sum_{\alpha}^{n}\sum_{i}^{x,y,z}\left(\frac{\partial U}{\partial x_i^{\alpha}(l)}\right)_0 u_i^{\alpha}(l) + \frac{1}{2}\sum_{l,l'}^{N}\sum_{\alpha,\beta}^{n}\sum_{i,j}^{x,y,z}\left(\frac{\partial^2 U}{\partial x_i^{\alpha}(l)\partial x_j^{\beta}(l')}\right)_0 u_i^{\alpha *}(l)u_j^{\beta}(l') + \ldots \quad (2.6)$$

where $x_i^{\alpha}(l)$ represents one of the three components of the vector describing the position of the α th atom in the l th unit cell, and $u_i^{\alpha}(l)$ is the deviation of the specific atom from its equilibrium position such that $u_i^{\alpha}(l) = x_i^{\alpha}(l) - x_i^{\alpha}(l)_0$. U_0 is the cohesive energy of the crystal and is usually set as zero. The second term is by definition zero around equilibrium because it represents the slope at the minimum of the potential energy well. So the third term is the non-zero leading term for the potential energy of the crystal. Neglecting higher order terms, I have

$$U = \frac{1}{2}\sum_{l,l'}^{N}\sum_{\alpha,\beta}^{n}\sum_{i,j}^{x,y,z}\left(\frac{\partial^2 U}{\partial x_i^{\alpha}(l)\partial x_j^{\beta}(l')}\right)_0 u_i^{\alpha *}(l)u_j^{\beta}(l') \quad (2.7)$$

Similarly, I can also write down the kinetic energy of the whole crystal as

$$K = \frac{1}{2}\sum_{l}^{N}\sum_{\alpha}^{n}\sum_{i}^{x,y,z} m^{\alpha}(l)\,\dot{u}_i^{\alpha *}(l)\dot{u}_i^{\alpha}(l) \quad (2.8)$$

where $m^{\alpha}(l)$ is the mass of the α th atom in the l th unit cell. Define the reduced displacements

$$\omega_i^{\alpha}(l) = \sqrt{m^{\alpha}(l)}\,u_i^{\alpha}(l) \quad (2.9)$$

as well as a dynamical matrix in real space

$$D_{ij}^{\alpha\beta}(l,l') = \frac{1}{\sqrt{m^{\alpha}(l)m^{\beta}(l')}}\left(\frac{\partial^2 U}{\partial x_i^{\alpha}(l)\partial x_j^{\beta}(l')}\right)_0 \tag{2.10}$$

Considering the translational symmetry of the crystal, $D_{ij}^{\alpha\beta}(l,l')$ only depends on the relative position of the two atoms, so it can be rewritten as $D_{ij}^{\alpha\beta}(l-l')$. Substituting Eq. (2.9) and Eq. (2.10) in Eq. (2.7) and Eq. (2.8), I have

$$U = \frac{1}{2}\sum_{l,l'}^{N}\sum_{\alpha,\beta}^{n}\sum_{i,j}^{x,y,z}\omega_i^{\alpha *}(l)D_{ij}^{\alpha\beta}(l-l')\omega_j^{\beta}(l') \tag{2.11}$$

$$K = \frac{1}{2}\sum_{l}^{N}\sum_{\alpha}^{n}\sum_{i}^{x,y,z}\dot{\omega}_i^{\alpha *}(l)\dot{\omega}_i^{\alpha}(l) \tag{2.12}$$

Perform Fourier transform on $\omega_i^{\alpha}(l)$ and get

$$\omega_i^{\alpha}(l) = \frac{1}{\sqrt{N}}\sum_{\mathbf{q}}^{N}\omega_i^{\alpha}(\mathbf{q})\,e^{i\mathbf{q}\cdot\mathbf{x}(l)_0} \tag{2.13}$$

where $\mathbf{q}$ is a wavevector in the reciprocal space spanned by the basis vectors of the reciprocal lattice $\mathbf{b}_1$, $\mathbf{b}_2$, $\mathbf{b}_3$. It satisfies the three-dimensional periodic boundary conditions such that

$$\mathbf{q} = \frac{h_1}{N_1}\mathbf{b}_1 + \frac{h_2}{N_2}\mathbf{b}_2 + \frac{h_3}{N_3}\mathbf{b}_3 \tag{2.14}$$

where $N_1 \times N_2 \times N_3 = N$, and h_1, h_2, h_3 are integers. $\mathbf{x}(l)_0$ is the equilibrium position of an arbitrary reference atom in the lth unit cell. Substituting Eq. (2.13) in Eq. (2.11), I have

$$U = \frac{1}{2N}\sum_{l,l'}^{N}\sum_{\alpha,\beta}^{n}\sum_{i,j}^{x,y,z}\sum_{\mathbf{q},\mathbf{q}'}^{N}\omega_i^{\alpha *}(\mathbf{q})e^{-i\mathbf{q}\cdot\mathbf{x}(l)_0}D_{ij}^{\alpha\beta}(l-l')\omega_j^{\beta}(\mathbf{q}')e^{i\mathbf{q}'\cdot\mathbf{x}(l')_0}$$

$$= \frac{1}{2N}\sum_{l,l'}^{N}\sum_{\alpha,\beta}^{n}\sum_{i,j}^{x,y,z}\sum_{\mathbf{q},\mathbf{q}'}^{N}\omega_i^{\alpha *}(\mathbf{q})e^{-i(\mathbf{q}-\mathbf{q}')\cdot\mathbf{x}(l)_0}D_{ij}^{\alpha\beta}(l-l')\omega_j^{\beta}(\mathbf{q}')e^{i\mathbf{q}'\cdot[\mathbf{x}(l')_0-\mathbf{x}(l)_0]}$$

$$= \frac{1}{2N} \sum_{l,(l'-l)}^{N} \sum_{\alpha,\beta}^{n} \sum_{i,j}^{x,y,z} \sum_{\mathbf{q},\mathbf{q}'}^{N} \omega_i^{\alpha*}(\mathbf{q}) e^{-i(\mathbf{q}-\mathbf{q}')\cdot\mathbf{x}(l)_0} D_{ij}^{\alpha\beta}(l-l') \omega_j^{\beta}(\mathbf{q}') e^{i\mathbf{q}'\cdot\mathbf{x}(l'-l)_0} \tag{2.15}$$

In the last line, I rewrite $[\mathbf{x}(l')_0 - \mathbf{x}(l)_0]$ as $\mathbf{x}(l'-l)_0$ since it only depends on the relative position of the two unit cells. Using the orthonormality of wavevectors

$$\frac{1}{N} \sum_{l}^{N} e^{i(\mathbf{q}'-\mathbf{q})\cdot\mathbf{x}(l)_0} = \delta_{\mathbf{q}\mathbf{q}'} \tag{2.16}$$

where $\delta_{\mathbf{q}\mathbf{q}'}$ is the Kronecker delta function. Eq. (2.15) is thus written as

$$U = \frac{1}{2} \sum_{l'-l}^{N} \sum_{\alpha,\beta}^{n} \sum_{i,j}^{x,y,z} \sum_{\mathbf{q},\mathbf{q}'}^{N} \omega_i^{\alpha*}(\mathbf{q}) \delta_{\mathbf{q}\mathbf{q}'} D_{ij}^{\alpha\beta}(l-l') \omega_j^{\beta}(\mathbf{q}') e^{i\mathbf{q}'\cdot\mathbf{x}(l'-l)_0}$$

$$= \frac{1}{2} \sum_{l'-l}^{N} \sum_{\alpha,\beta}^{n} \sum_{i,j}^{x,y,z} \sum_{\mathbf{q}}^{N} \omega_i^{\alpha*}(\mathbf{q}) D_{ij}^{\alpha\beta}(l-l') \omega_j^{\beta}(\mathbf{q}) e^{i\mathbf{q}\cdot\mathbf{x}(l'-l)_0}$$

$$= \frac{1}{2} \sum_{\alpha,\beta}^{n} \sum_{i,j}^{x,y,z} \sum_{\mathbf{q}}^{N} \omega_i^{\alpha*}(\mathbf{q}) D_{ij}^{\alpha\beta}(\mathbf{q}) \omega_j^{\beta}(\mathbf{q}) \tag{2.17}$$

where $D_{ij}^{\alpha\beta}(\mathbf{q})$ is the Fourier transform of $D_{ij}^{\alpha\beta}(l)$ such that

$$D_{ij}^{\alpha\beta}(\mathbf{q}) = \sum_{l}^{N} D_{ij}^{\alpha\beta}(l) e^{-i\mathbf{q}\cdot\mathbf{x}(l)_0} \tag{2.18}$$

Now I have a sum of N independent functions labeled by $\mathbf{q}$. For the $3n \times 3n$ dynamic matrix $\mathbf{D}(\mathbf{q})$, I can find its $3n$ eigenvalues and corresponding eigenvectors by solving the secular equations

$$\sum_{\beta}^{n} \sum_{j}^{x,y,z} D_{ij}^{\alpha\beta}(\mathbf{q}) \varepsilon_j^{\beta}(\mathbf{q},\gamma) = \Omega^2(\mathbf{q},\gamma) \varepsilon_i^{\alpha}(\mathbf{q},\gamma) \tag{2.19}$$

where γ labels one of the $3n$ phonon branches. $\Omega(\mathbf{q},\gamma)$ is the eigenvalue that gives the dispersion relation and $\boldsymbol{\varepsilon}(\mathbf{q},\gamma)$ is the corresponding eigenvector. The eigenvectors have the relations below

$$\sum_{\alpha}^{n}\sum_{i}^{x,y,z}\varepsilon_i^{\alpha*}(\mathbf{q},\gamma)\varepsilon_i^{\alpha}(\mathbf{q},\gamma')=\delta_{\gamma\gamma'} \tag{2.20}$$

Define phonon coordinates as

$$Q(\mathbf{q},\gamma)=\sum_{\alpha}^{n}\sum_{i}^{x,y,z}\varepsilon_i^{\alpha*}(\mathbf{q},\gamma)\omega_i^{\alpha}(\mathbf{q}) \tag{2.21}$$

$$\omega_i^{\alpha}(\mathbf{q})=\sum_{\gamma}^{3n}\varepsilon_i^{\alpha*}(\mathbf{q},\gamma)Q(\mathbf{q},\gamma) \tag{2.22}$$

Substitute Eq. (2.22) into Eq. (2.17), I have

$$\begin{aligned}U&=\frac{1}{2}\sum_{\alpha,\beta}^{n}\sum_{i,j}^{x,y,z}\sum_{\mathbf{q}}^{N}\sum_{\gamma,\gamma'}^{3n}\varepsilon_i^{\alpha}(\mathbf{q},\gamma)Q^{*}(\mathbf{q},\gamma)D_{ij}^{\alpha\beta}(\mathbf{q})\varepsilon_j^{\beta*}(\mathbf{q},\gamma')Q(\mathbf{q},\gamma')\\&=\frac{1}{2}\sum_{\alpha}^{n}\sum_{i}^{x,y,z}\sum_{\mathbf{q}}^{N}\sum_{\gamma,\gamma'}^{3n}\varepsilon_i^{\alpha}(\mathbf{q},\gamma)Q^{*}(\mathbf{q},\gamma)\Omega^{2}(\mathbf{q},\gamma')\varepsilon_i^{\alpha*}(\mathbf{q},\gamma')Q(\mathbf{q},\gamma')\\&=\frac{1}{2}\sum_{\mathbf{q}}^{N}\sum_{\gamma,\gamma'}^{3n}Q^{*}(\mathbf{q},\gamma)\Omega^{2}(\mathbf{q},\gamma')Q(\mathbf{q},\gamma')\delta_{\gamma\gamma'}\\&=\frac{1}{2}\sum_{\mathbf{q}}^{N}\sum_{\gamma}^{3n}\Omega^{2}(\mathbf{q},\gamma)Q^{*}(\mathbf{q},\gamma)Q(\mathbf{q},\gamma)\end{aligned} \tag{2.23}$$

Eq. (2.19) and Eq. (2.20) are used to get the second and the third lines. The potential energy is now decomposed into $3nN$ independent phonon modes, each indexed by the phonon branch number γ and wavevector $\mathbf{q}$. There are in total $3n$ phonon branches (some of which can be degenerate) for a crystal with n atoms in each unit cell and N modes on each branch. Within the $3n$ branches, there are 3 acoustic phonon branches and $3n-3$ optical phonon branches.

The kinetic energy can be expressed in terms of normal modes, too. Substitute Eq. (2.13) into Eq. (2.12) and use Eq. (2.16) to get

$$K=\frac{1}{2N}\sum_{l}^{N}\sum_{\alpha}^{n}\sum_{i}^{x,y,z}\sum_{\mathbf{q}}^{N}\dot{\omega}_i^{\alpha*}(\mathbf{q})e^{-i\mathbf{q}\cdot\mathbf{x}(l)}\sum_{\mathbf{q}'}^{N}\dot{\omega}_i^{\alpha}(\mathbf{q}')e^{i\mathbf{q}'\cdot\mathbf{x}(l)}$$

$$= \frac{1}{2}\sum_{\alpha}^{n}\sum_{i}^{x,y,z}\sum_{\mathbf{q}}^{N}\dot{\omega}_i^{\alpha *}(\mathbf{q})\dot{\omega}_i^{\alpha}(\mathbf{q}) \tag{2.24}$$

Substituting Eq. (2.22) into Eq. (2.24) and using Eq. (2.20),

$$K = \frac{1}{2}\sum_{\alpha}^{n}\sum_{i}^{x,y,z}\sum_{\mathbf{q}}^{N}\sum_{\gamma,\gamma'}^{3n}\varepsilon_i^{\alpha}(\mathbf{q},\gamma)\dot{Q}^{*}(\mathbf{q},\gamma)\varepsilon_i^{\alpha *}(\mathbf{q},\gamma')\dot{Q}(\mathbf{q},\gamma')$$

$$= \frac{1}{2}\sum_{\mathbf{q}}^{N}\sum_{\gamma,\gamma'}^{3n}\dot{Q}^{*}(\mathbf{q},\gamma)\dot{Q}(\mathbf{q},\gamma')\delta_{\gamma\gamma'}$$

$$= \frac{1}{2}\sum_{\mathbf{q}}^{N}\sum_{\gamma}^{3n}\dot{Q}^{*}(\mathbf{q},\gamma)\dot{Q}(\mathbf{q},\gamma) \tag{2.25}$$

The Hamiltonian is therefore the sum of those of $3nN$ independent harmonic oscillators. In this way, the complicated lattice vibration can be investigated by studying the decoupled normal modes. The real atomic displacements $u_i^{\alpha}(l)$ and phonon amplitudes $Q(\mathbf{q},\gamma)$ are connected by Eq. (2.9), Eq. (2.13) and Eq. (2.22). After second quantization, the energy of the crystal is

$$E = \sum_{j}^{3nN}(n_j + \frac{1}{2})\hbar\Omega_j \tag{2.26}$$

where j is a shorthand for the mode indexed by $(\mathbf{q},\gamma)$. The energy quantum $\hbar\Omega_j$ is called a phonon and n_j is the number of phonons in mode j.

To get the dispersion curve described by Eq. (2.19), the force constants $\partial^2 U / \partial x_i^{\alpha}(l)\partial x_j^{\beta}(l')$ are needed. Examples of different models taking into account the influences of neighboring atoms, Coulomb interactions and screenings are presented in Ref. [5]. The parameters in the model are then adjusted to fit experimental quantities. After that, numerical calculations are performed to solve Eq. (2.19) in order to obtain phonon frequencies [5].

2.2 Light scattering by optical phonons

When light is incident on a solid, inelastic scattering takes place due to the spatial or temporal fluctuations in the electric susceptibility of the material. The typical frequency shift by acoustic phonons around $1cm^{-1}$ or less is called Brillouin scattering [7], in which case a Fabry-Perot interferometer is often used for detection. For the frequency shift larger than $10cm^{-1}$ and often in the range $100\text{-}1000cm^{-1}$ associated with optical phonons [7], a diffraction-grating based Raman spectrometer is employed. The process in this frequency domain is called Raman scattering.

Based on whether an energy quantum $\hbar\Omega$ is created or absorbed, inelastic light scattering can be classified as Stokes scattering and anti-Stokes scattering, as shown in Fig. 2.3. In Stokes scattering, a phonon is created and the light is red shifted. In anti-Stokes scattering, a phonon is absorbed and the light is blue shifted. In a transparent material, momentum and energy are conserved in both cases. In an opaque material, the restriction on the momentum conservation is relaxed by $2/\Delta z$, where Δz is the penetration depth of the light [8].

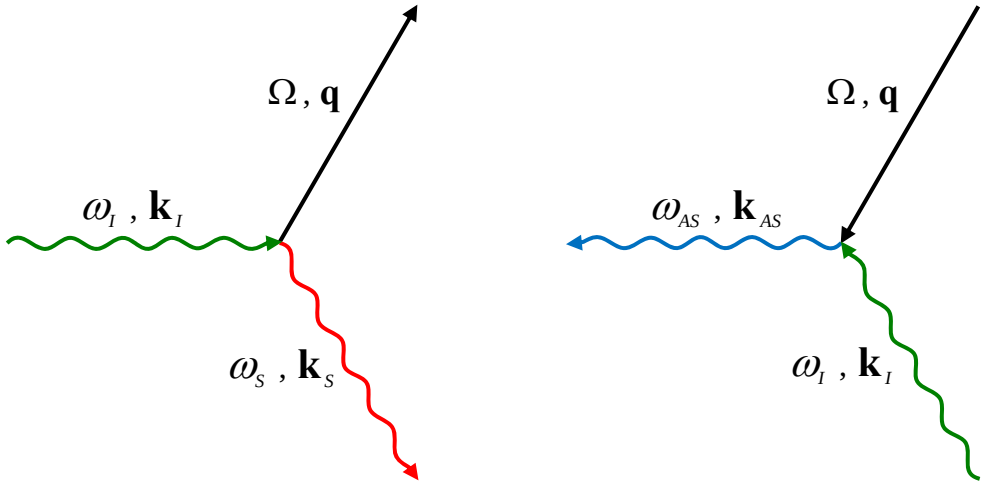

Figure 2.3. Vector diagrams for Stokes scattering (left) and anti-Stokes scattering (right).

For a material with refractive index 1.5, the typical wavevector available for a light scattering experiment is $0 < q < 3\times10^{7}\,m^{-1}$. Compared with the range of Brillouin zone

on the order of $3\times10^{10}\,m^{-1}$, the method of light scattering is actually probing phonons with wavevectors close to the center of the Brillouin zone [7]. In this region, the optical branch is dispersionless. It is only when phonon-polaritons are involved that dispersion needs to be considered, which concerns transverse infrared active modes in a polar material [5,8].

2.2.1 Macroscopic description of spontaneous Raman scattering

A spontaneous Raman scattering (RS) experiment usually measures the relative frequency shift of the scattered light from the excitation light. The incident electric field excites an ensemble of oscillating dipole moments which emit radiation that adds up incoherently, at a frequency shifted Ω away from the incident light frequency by the optical phonons.

Macroscopically, that effect is incorporated in the electric susceptibility as a nonlinear correction term. The electric susceptibility of a material is $\chi \simeq \chi_0 + \frac{\partial \chi}{\partial Q} Q$, where $Q = Q_0 e^{-i\Omega t} + Q_0^* e^{i\Omega t}$, Q_0 is the complex phonon amplitude, χ_0 is the linear susceptibility and $\chi^R \equiv \frac{\partial \chi}{\partial Q}$ is the Raman susceptibility. For an monochromatic incident electric field $E(t) = E_0 e^{-i\omega t} + E_0^* e^{i\omega t}$, the polarization is

$$P(t) = \chi E(t) = \left[\chi_0 + \chi^R \left(Q_0 e^{-i\Omega t} + Q_0^* e^{i\Omega t} \right) \right] \left(E_0 e^{-i\omega t} + E_0^* e^{i\omega t} \right)$$

$$= \chi_0 \left(E_0 e^{-i\omega t} + E_0^* e^{i\omega t} \right) + \chi^R \left[E_0 Q_0^* e^{-i(\omega-\Omega)t} + E_0^* Q_0 e^{i(\omega-\Omega)t} \right] + \chi^R \left[E_0 Q_0 e^{-i(\Omega+\omega)t} + E_0^* Q_0^* e^{i(\Omega+\omega)t} \right]$$

(2.27)

The first term describes elastic scattering; the second term describes Stokes scattering at frequency $\omega - \Omega$, and the third term describes anti-Stokes scattering at frequency $\omega + \Omega$.

Another important physical quantity for the scattered light is its intensity. Scattering

cross sections are commonly used to characterize the efficiency of scattering. The differential cross section for Stokes scattering into a unit solid angle is defined as [7]

$$\frac{d^2\sigma}{d\Omega_{solid}d\omega_s} \equiv \frac{\omega_I \upsilon}{\omega_S L}\frac{d^2 I_S}{d\Omega_{solid}d\omega_s}\frac{1}{I_I} \tag{2.28}$$

where ω_I and ω_S are the frequencies of the incident and Stoke scattered light respectively, I_I and I_S are the incident and scattered light intensity, υ and L are the volume and length of the part in the material that contributes to the scattered light. By substituting the second term of Eq. (2.27), which is the Stokes polarization, in the source term of Maxwell's wave equations for the scattered electric field E_S, the latter can be derived to calculate I_S. I then have [7]

$$\frac{d^2\sigma}{d\Omega_{solid}d\omega_s} = \frac{\omega_I \omega_S^3 \upsilon V n_S \left\langle \mathbf{e}_S \cdot \mathbf{P}_S \mathbf{e}_S \cdot \mathbf{P}_S \right\rangle_{\omega_S}}{(4\pi\varepsilon_0)^2 c^4 n_I \left|\mathbf{E}_I\right|^2} \tag{2.29}$$

where $\mathbf{E}_I$ is the incident electric field, $\mathbf{P}_S$ is the Stokes polarization, $\left\langle \mathbf{e}_S \cdot \mathbf{P}_S \mathbf{e}_S \cdot \mathbf{P}_S \right\rangle_{\omega_S}$ is called the power spectrum of the polarization fluctuations and is averaged over the fluctuation probability distribution, n_I and n_S are the refractive indices for the incident and scattered light, $\mathbf{e}_I$ and $\mathbf{e}_S$ are the corresponding light polarization unit vectors. According to the fluctuation-dissipation theory [7], the power spectrum is related to the imaginary part of the linear-response function of the system, which can be expressed in the form of the distribution probability and the lineshape function of phonons. I have [7]

$$\frac{d^2\sigma}{d\Omega_{solid}d\omega_S} = \frac{\hbar \omega_I \omega_S^3 \upsilon V n_S \left|\sum_{kl} e_S^k \chi_{kl}^R e_I^l\right|^2 \left[n(\Omega)+1\right]}{(4\pi)^2 2c^4 n_I N \Omega} g_\Omega(\omega) \tag{2.30}$$

where $\omega = \omega_I - \omega_S$, N/V is the atomic density and the indices k and l sum over x, y and z, $g_\Omega(\omega)$ is the lineshape function of the phonons with frequency Ω. For

damped harmonic oscillators, $g_\Omega(\omega)$ has a Lorentzian lineshape with full width half maximum (FWHM) W such that

$$g_\Omega(\omega) = \frac{W/2\pi}{(\omega-\Omega)^2 + (W/2)^2} \tag{2.31}$$

$n(\Omega)$ is the Bose-Einstein factor given by

$$n(\Omega) = \frac{1}{\exp(\hbar\Omega/k_B T) - 1} \tag{2.32}$$

where T is the sample temperature and k_B is the Boltzmann's constant. More details of the derivation of the Raman scattering cross section can be found in Ref [7].

A similar expression for an anti-Stokes scattering cross section can be obtained by replacing $[n(\Omega)+1]$ in Eq. (2.30) by $n(\Omega)$. A simple relationship between the Stokes and anti-Stokes scattering cross sections is [7]

$$\frac{\left(\frac{d^2\sigma}{d\Omega_{solid}\, d\omega}\right)_S}{\left(\frac{d^2\sigma}{d\Omega_{solid}\, d\omega}\right)_{AS}} = \frac{\omega_S^2 n_S^2 [n(\Omega)+1]}{\omega_I^2 n_I^2 n(\Omega)} \tag{2.33}$$

which is sometimes used to estimate the sample temperature.

The Raman susceptibility is often written in the form of a tensor called the Raman tensor. The positions of non-zero elements and elements of related values in a Raman tensor are determined by the symmetry properties of the crystal as well as the specific mode that the tensor depicts.

The macroscopic description of RS is convenient because it can be easily related to quantities measured in experiments and physical parameters of the materials. On the other hand, the microscopic description of RS is useful in predicting how the cross section changes with experimental parameters [7].

2.2.2 Microscopic description of spontaneous Raman scattering

Loudon [9,10] derived the microscopic expression for Raman tensors in diamond lattice and zinc blende lattice crystals. Analogies of the conclusion can be easily drawn for crystals with other structures by modifying the effective mass associated with the optical phonons.

Considering a system consisting of the quantized radiation field, electrons and quantized phonon field, the spontaneous Raman scattering cross section is proportional to the transition rate from the ground state with N_I incident photons at frequency ω_I and n phonons at Ω to the excited state with (N_I+1) photons at ω_I, one scattered photon at ω_S and $(n+1)$ phonons. Based on third-order time-dependent perturbation theory, the transition rate is [10]

$$\frac{1}{\tau}=\frac{2\pi}{\hbar^6}\sum_{\mathbf{q},\mathbf{k}_S}\left|\sum_{\alpha,\beta}\frac{\langle N_I-1,1;n+1;0|H_{\text{int}}|\alpha\rangle\langle\alpha|H_{\text{int}}|\beta\rangle\langle\beta|H_{\text{int}}|N_I,0;n;0\rangle}{(\omega_\alpha-\omega_I)(\omega_\beta-\omega_I)}\right|^2 \times\delta(\omega_I-\Omega-\omega_S) \tag{2.34}$$

where the first three parameters N_I, 0 and n in the ket for the initial state are the initial numbers of incident photons, scattered photons and optical phonons; the last 0 stands for the electronic ground state; $|\alpha\rangle$ and $|\beta\rangle$ are the intermediate states with energies $\hbar\omega_\alpha$ and $\hbar\omega_\beta$. The sum over $\mathbf{k}_S$ is confined within the solid angle Ω_{solid} subtended by the collecting lens. The interaction Hamiltonian $H_{\text{int}}=H_{EL}+H_{ER}$, where the first term is the electron-lattice interaction and the second term is the electron-radiation interaction. After substituting the specific forms of H_{EL} and H_{ER} in Eq. (2.34), an expression for a Raman tensor is obtained such that [9,11]

$$R_{kl}(-\omega_I,\omega_S,\Omega)=\frac{1}{V}\sum_{\alpha,\beta}\left\{\frac{\Delta^k_{0\beta}\Delta^l_{\beta\alpha}\Xi_{\alpha 0}}{(\omega_\beta+\Omega-\omega_I)(\omega_\alpha+\Omega)}+\frac{\Delta^l_{0\beta}\Delta^k_{\beta\alpha}\Xi_{\alpha 0}}{(\omega_\beta+\Omega+\omega_S)(\omega_\alpha+\Omega)}\right.$$
$$+\frac{\Delta^k_{0\beta}\Xi_{\beta\alpha}\Delta^l_{\alpha 0}}{(\omega_\beta+\Omega-\omega_I)(\omega_\alpha-\omega_I)}+\frac{\Delta^l_{0\beta}\Xi_{\beta\alpha}\Delta^k_{\alpha 0}}{(\omega_\beta+\Omega+\omega_S)(\omega_\alpha+\omega_S)} \qquad (2.35)$$
$$\left.+\frac{\Xi_{0\beta}\Delta^k_{\beta\alpha}\Delta^l_{\alpha 0}}{(\omega_\beta+\omega_S-\omega_I)(\omega_\alpha-\omega_I)}+\frac{\Xi_{0\beta}\Delta^l_{\beta\alpha}\Delta^k_{\alpha 0}}{(\omega_\beta+\omega_S-\omega_I)(\omega_\alpha+\omega_S)}\right\}$$

where Ξ is the deformation potential that characterizes the strength of electron-lattice coupling, accounting for the scenario that when a phonon is created, the related atomic displacements perturb the periodic potential that electrons are experiencing, thus leading to an electron-lattice interaction energy [9]. The delta function in Eq. (2.34) should be replaced by a Lorentzian function of the same form as Eq. (2.31) if the lifetime of the phonon is considered and phonon anharmonic interactions are used to obtain the line width W [9].

Note that according to Eq. (2.30) and Eq. (2.35), all the terms in a Raman tensor are added together and then squared to get the scattering cross section measured in an experiment. It is thus possible that quantum pathways will interfere with others constructively or destructively depending on their relative signs [5]. Such phenomenon was observed in CdS, Si and GaAs [12,13], and was also recently found in graphene with its G mode and 2D mode [14].

When the energy of incident light approaches that of the electronic resonance, the virtual intermediate states in Eq. (2.34) become real ones and resonant Raman scattering occurs. The material usually shows an enhanced scattering efficiency. In this case, a complex energy is needed for $\hbar\omega_\alpha$ or $\hbar\omega_\beta$ to guarantee the convergence of Eq. (2.35). Details of the treatment for that case are included in Section 2.3.2.

2.3 Impulsively stimulated Raman scattering

When two laser beams with frequency difference $\omega_1-\omega_2=\Omega$ are incident on a

solid, a coherent macroscopic phonon field can be created, a process called stimulated Raman scattering (SRS). SRS signals are intense and highly directional, in contrast with the RS experiment which has relatively weak light scattered in all directions. The coherent phonon field attenuates the intensity at ω_1 and amplifies the intensity at ω_2. It can also generate a coherent anti-Stokes Raman field at $2\omega_1 - \omega_2$, which is the base for coherent anti-Stokes Raman spectroscopy (CARS), or intensity induced birefringence and dichroism, which is the base for Raman induced Kerr effect spectroscopy (RIKES) [15].

Shen and Bloembergen derived the theoretical explanation for SRS by solving a coupled-wave problem [16]. They added nonlinear polarization terms describing effects of the phonon field in the wave equations of the laser, Stokes and anti-Stokes fields. At the same time, the coherent phonon field is driven by a force provided by pairs of the radiation fields. In this way, four coupled wave equations can be formulated and solved with appropriate boundary and initial conditions.

SRS is sometimes studied with a femtosecond pulsed laser instead of two continuous wave lasers. The phenomenon is called impulsively stimulated Raman scattering (ISRS) owing to the short timescale of the pulse. The pulse has a broad enough spectral bandwidth so that it provides numerous frequency pairs separated by Ω, as shown in Fig. 2.4, and wavevector conservation is automatically satisfied in the forward direction.

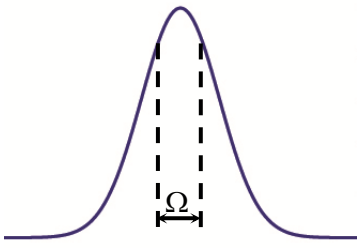

Figure 2.4. Illustration of one of the frequency pairs with a frequency separation Ω within the pulse spectrum.

Experimentally, a coherent phonon field is created by a pump pulse, and the

modulation of the optical properties of the sample induced by the phonon is monitored by a probe pulse that follows behind. By changing the time delay between the pump and probe pulses, the time domain evolution of the coherent phonon field can be obtained.

2.3.1 Impulsively stimulated Raman scattering in transparent materials

The equation of motion for a coherent phonon field with an amplitude $Q(t)$, frequency Ω and decay rate b is

$$\frac{d^2Q(\mathbf{r},t)}{dt^2} + 2b\frac{dQ(\mathbf{r},t)}{dt} + \Omega^2 Q(\mathbf{r},t) = F(\mathbf{r},t) \tag{2.36}$$

where $F(\mathbf{r},t)$ is a coherent driving force provided by the pump pulse. Neglecting the depletion of the pump, in a transparent material, $F(\mathbf{r},t)$ is proportional to the pump field intensity such that [8]

$$F(\mathbf{r},t) = \frac{1}{2}\sum_{kl}\chi_{kl}^{R}E_k E_l^* \tag{2.37}$$

where the summation of k and l runs over all three Cartesian coordinates and $\mathbf{E}$ is the pump electric field. Using Green's function method, the solution to Eq. (2.36) is

$$Q(\mathbf{r},t) = \int_{-\infty}^{t}\frac{\sin[\Omega(t-\tau)]}{\Omega}e^{-b(t-\tau)}F(\mathbf{r},\tau)d\tau \tag{2.38}$$

For a Gaussian pulse propagating along z, $\mathbf{E}(u) = \mathbf{E}_0\exp\left[-\left(u^2/2\tau_0^2\right)\right]\cos(\omega_0 u)$ and $u = t - zn/c$, where $\mathbf{E}_0$, τ_0 and ω_0 are the electric field amplitude, pulsewidth and central frequency of the pulse, n is the refractive index. With Eq. (2.37) and Eq. (2.38), I have [8]

$$Q(u) \approx \frac{\pi^{1/2}\tau_0}{4\Omega}\left|E_0\right|^2 e^{-\Omega^2\tau_0^2/4}\left(\sum_{kl}\chi_{kl}^{R}\cos(\alpha_k)\cos(\alpha_l)\right)e^{-bu}\sin(\Omega u) \tag{2.39}$$

where $\cos(\alpha_k)$ and $\cos(\alpha_l)$ are the direction cosines of the pump. The effect of the coherent phonon on the probe is to modulate the refractive index, which is manifested as

a nonlinear polarization term in the wave equation of the probe electric field e_m [8]

$$\nabla^2 e_m = \frac{1}{c^2} \times \frac{\partial^2}{\partial t^2} \left(n^2 e_m + 4\pi \sum_p \chi^R_{mp} Q(\mathbf{r},t) e_p \right) \tag{2.40}$$

Solving the wave equation above, I can get the relative change of probe intensity [8]

$$\begin{aligned} \Delta T / T = & -\frac{\pi^{3/2} \tau_0 L}{2nc} \left| E_0 \right|^2 e^{-b\Delta t} \cos(\Omega \Delta t) e^{-\Omega^2 \tau_0^2 / 2} \\ & \times \sum_{kl,mp} \left(\chi^R_{kl} \cos(\alpha_k) \cos(\alpha_l) \right) \left(\chi^R_{mp} \cos(\beta_m) \cos(\beta_p) \right) \end{aligned} \tag{2.41}$$

where $\cos(\beta_m)$ and $\cos(\beta_p)$ are the direction cosines of the probe beam. Δt is the time delay between the pump and probe pulses. L is the thickness of the sample. Eq. (2.41) represents the bulk contribution of the phonon field.

By taking into account the influence of boundaries at $z = 0$ and $z = L$, an interface contribution should be added, which modulates both transmittance and reflectance of the probe such that [8]

$$\begin{aligned} \Delta T / T = & \frac{\pi^{3/2} \tau_0 (n-1)}{\Omega n^2 (n+1)} \left| E_0 \right|^2 e^{-b\Delta t} \sin(\Omega \Delta t) e^{-\Omega^2 \tau_0^2 / 2} \\ & \times \sum_{kl,mp} \left(\chi^R_{kl} \cos(\alpha_k) \cos(\alpha_l) \right) \left(\chi^R_{mp} \cos(\beta_m) \cos(\beta_p) \right) \end{aligned} \tag{2.42}$$

$$\begin{aligned} \Delta R / R = & -\frac{2\pi^{3/2} \tau_0}{\Omega n (n-1)(n+1)} \left| E_0 \right|^2 e^{-b\Delta t} \sin(\Omega \Delta t) e^{-\Omega^2 \tau_0^2 / 2} \\ & \times \sum_{kl,mp} \left(\chi^R_{kl} \cos(\alpha_k) \cos(\alpha_l) \right) \left(\chi^R_{mp} \cos(\beta_m) \cos(\beta_p) \right) \end{aligned} \tag{2.43}$$

Eq. (2.42) and Eq. (2.43) are the derivatives of transmittance and reflectance of the probe intensity with respect to n.

2.3.2 The theory of two stimulated Raman tensors

While the behavior of coherent phonons in transparent materials is well understood, the answer to whether the generation mechanisms involved in opaque materials are related to Raman processes or not had been inconclusive. That led to the proposal of a

microscopic view of the pump-probe process, which suggested two different stimulated Raman tensors involved in the generation and scattering processes in a pump-probe experiment [17]. The specific form of the tensors also revealed the difference of Raman processes between a transparent material and an opaque material. This section is a brief review of the theory based on Ref [17] and Ref [18] using the density matrix formalism.

With a semiclassical method which treats the radiation field as classical and crystal as quantized, the Hamiltonian of the system can be written as

$$\hat{H} = \frac{1}{2}\hat{P}^2 + \frac{1}{2}\Omega_0^2\hat{Q}^2 + \hat{H}_e + \hat{H}_{\text{int}} \tag{2.44}$$

$$\hat{H}_{\text{int}} = -\hat{\Xi}\hat{Q} - \hat{\Delta}\cdot\mathbf{E}(t) \tag{2.45}$$

where $\hat{H}_e$ is the Hamiltonian of the electron subsystem with $\hat{H}_e|n\rangle = \omega_n|n\rangle$. $\hat{H}_{\text{int}}$ is the interaction Hamiltonian containing the phonon-electron interaction $-\hat{\Xi}\hat{Q}$ and the electron-radiation interaction $-\hat{\Delta}\cdot\mathbf{E}(t)$. $\hat{P}$ and $\hat{Q}$ are the operators for the canonical momentum and coordinate of the phonon field. $\hat{\Xi}$ and $\hat{\Delta}$ are the operators for the deformation potential and dipole-moment.

Based on time-dependent perturbation theory, with $\mathbf{E}(t) = \sum_p \mathbf{E}(\omega_p)e^{-i\omega_p t}$ and $Q(t) = \sum_p Q(\omega_p)e^{-i\omega_p t}$, I can derive the density matrix as follows [18]. For the unperturbed density matrix

$$\rho_{nm}^{(0)} = 0 \quad n \neq m \tag{2.46}$$

where $\sum_n \rho_{nn}^{(0)} = 1$. For the first order contribution

$$\rho_{nm}^{(1)} = \int_{-\infty}^{t} \frac{-i}{\hbar}[\hat{H}_{\text{int}}(t'), \rho^{(0)}]_{nm} e^{(i\omega_{nm}+\gamma_{nm})(t'-t)}dt'$$

$$= \frac{1}{\hbar}(\rho_{mm}^{(0)} - \rho_{nn}^{(0)})\sum_p [\mathbf{\Delta}_{nm}\cdot\mathbf{E}(\omega_p) + \Xi_{nm}Q(\omega_p)]\frac{e^{-i\omega_p t}}{(\omega_{nm}-\omega_p) - i\gamma_{nm}} \tag{2.47}$$

where γ_{nm} is the damping rate of the ρ_{nm} coherence, $\mathbf{\Delta}_{nm} = \langle n|\hat{\mathbf{\Delta}}|m\rangle$, $\Xi_{nm} = \langle n|\hat{\Xi}|m\rangle$

and $\omega_{nm} = \omega_n - \omega_m$. For the second order contribution

$$\rho_{nm}^{(2)} = \int_{-\infty}^{t} \frac{-i}{\hbar} [\hat{H}_{\text{int}}(t'), \rho^{(1)}]_{nm} e^{(i\omega_{nm} + \gamma_{nm})(t'-t)} dt' \tag{2.48}$$

where

$$\begin{aligned}
&[\hat{H}_{\text{int}}(t), \rho^{(1)}]_{nm} \\
&= -\sum_{\nu} \frac{1}{\hbar} (\rho_{mm}^{(0)} - \rho_{\nu\nu}^{(0)}) \sum_{p,q} [\boldsymbol{\Delta}_{n\nu} \cdot \mathbf{E}(\omega_q) + \Xi_{n\nu} Q(\omega_q)][\boldsymbol{\Delta}_{\nu m} \cdot \mathbf{E}(\omega_p) + \Xi_{\nu m} Q(\omega_p)] \frac{e^{-i(\omega_p + \omega_q)t}}{(\omega_{\nu m} - \omega_p) - i\gamma_{\nu m}} \\
&+ \sum_{\nu} \frac{1}{\hbar} (\rho_{\nu\nu}^{(0)} - \rho_{nn}^{(0)}) \sum_{p,q} [\boldsymbol{\Delta}_{\nu m} \cdot \mathbf{E}(\omega_q) + \Xi_{\nu m} Q(\omega_q)][\boldsymbol{\Delta}_{n\nu} \cdot \mathbf{E}(\omega_p) + \Xi_{n\nu} Q(\omega_p)] \frac{e^{-i(\omega_p + \omega_q)t}}{(\omega_{n\nu} - \omega_p) - i\gamma_{n\nu}}
\end{aligned} \tag{2.49}$$

With these terms, I can proceed to calculate the physical quantities related to coherent phonons.

Since $\hat{Q}$ does not contain t explicitly, I have

$$\frac{d^2 \langle \hat{Q} \rangle}{dt^2} = -\frac{1}{\hbar^2} \left\langle \left[\left[\hat{Q}, \hat{H} \right], \hat{H} \right] \right\rangle \tag{2.50}$$

which gives

$$\frac{d^2 \langle \hat{Q} \rangle}{dt^2} + \Omega_0^2 \langle \hat{Q} \rangle = \langle \hat{\Xi} \rangle \equiv F(t) \tag{2.51}$$

From the expression for $F(t)$ in Eq. (2.37), only terms proportional to $E_k E_l$ in $\rho_{nm}^{(2)}$ contribute to the driving force

$$F(t) = \sum_{mn} \Xi_{mn} \rho_{nm}^{(2)EE} \tag{2.52}$$

where the superscript EE indicates terms proportional to $E_k E_l$ in the second order density matrix. Substituting Eq. (2.48) and Eq. (2.49) in Eq. (2.52), and assuming the system is originally at the ground state such that $\rho_{kk}^{(0)} = \delta_{k0}$, I get

$$\begin{aligned}
&F(t) = \frac{1}{2\pi\hbar^2} \sum_{mn} \int_{-\infty}^{+\infty} d\omega \int_{-\infty}^{+\infty} d\Omega \exp(-i\Omega t) \times \\
&\left\{ \frac{\Xi_{0m} [\boldsymbol{\Delta}_{mn} \cdot \mathbf{E}(\omega)][\boldsymbol{\Delta}_{n0} \cdot \mathbf{E}^*(\omega - \Omega)]}{(\omega_m - \Omega - i\gamma_m)(\omega_n + \omega - \Omega - i\gamma_n)} + \frac{1}{2} \frac{\Xi_{mn} [\boldsymbol{\Delta}_{n0} \cdot \mathbf{E}(\omega)][\boldsymbol{\Delta}_{0m} \cdot \mathbf{E}^*(\omega - \Omega)]}{(\omega_m - \omega + \Omega + i\gamma_m)(\omega_n - \omega - i\gamma_n)} \right\} + c.c.
\end{aligned} \tag{2.53}$$

For the polarization related to the phonon field, only terms proportional to $E_k Q_l$ in

$\rho_{nm}^{(2)}$ contribute, as in Eq. (2.27). Define the Raman polarization

$$\mathbf{P}^R(t) = \frac{1}{N\upsilon_c}\langle \boldsymbol{\Delta} \rangle^R = \frac{1}{N\upsilon_c}\sum_{mn} \boldsymbol{\Delta}_{mn}\rho_{nm}^{(2)EQ} \tag{2.54}$$

where N is the number of unit cells and υ_c is the volume of each unit cell. Following similar steps as the ones for $F(t)$, I get

$$\begin{aligned}\mathbf{P}^R(t) = {} & \frac{1}{2\pi\hbar^2 N\upsilon_c}\sum_{mn}\int_{-\infty}^{+\infty} d\omega \int_{-\infty}^{+\infty} d\Omega \exp[-i(\omega-\Omega)t]Q^*(\Omega)\times \\ & \left\{ \frac{\boldsymbol{\Delta}_{0m}\Xi_{mn}[\boldsymbol{\Delta}_{n0}\cdot\mathbf{E}(\omega)]}{(\omega_m-\omega+\Omega-i\gamma_m)(\omega_n-\omega-i\gamma_n)} + \frac{\boldsymbol{\Delta}_{0m}[\boldsymbol{\Delta}_{mn}\cdot\mathbf{E}(\omega)]\Xi_{n0}}{(\omega_m+\Omega-\omega-i\gamma_m)(\omega_n+\Omega-i\gamma_n)} \right. \\ & \left. + \frac{\boldsymbol{\Delta}_{nm}[\boldsymbol{\Delta}_{m0}\cdot\mathbf{E}(\omega)]\Xi_{0n}}{(\omega_n-\Omega+i\gamma_n)(\omega_m-\omega-i\gamma_m)} \right\} + c.c.\end{aligned} \tag{2.55}$$

Define two stimulated Raman tensors π^R and χ^R as

$$F(t) = \frac{N\upsilon_c}{4\pi}\sum_{kl}\int_{-\infty}^{+\infty} d\omega \int_{-\infty}^{+\infty} d\Omega \exp(-i\Omega t)E_k^*(\omega-\Omega)E_l(\omega)\pi_{kl}^R(\omega,\omega-\Omega) \tag{2.56}$$

$$P_k^R(t) = \frac{1}{2\pi}\sum_{l}\int_{-\infty}^{+\infty} d\omega \int_{-\infty}^{+\infty} d\Omega \exp[-i(\omega-\Omega)t]Q^*(\Omega)E_l(\omega)\chi_{kl}^R(\omega,\omega-\Omega) \tag{2.57}$$

Comparing Eq. (2.53), Eq. (2.56), Eq. (2.55) and Eq. (2.57), I have

$$\begin{aligned}\pi_{kl}^R(\omega,\omega-\Omega) = {} & \frac{1}{\hbar^2 N\upsilon_c}\sum_{mn}\left[\frac{\Xi_{0m}\Delta_{mn}^l\Delta_{n0}^k}{(\omega_m-\Omega-i\gamma_m)(\omega_n+\omega-\Omega-i\gamma_n)} \right. \\ & + \frac{\Xi_{0m}\Delta_{mn}^k\Delta_{n0}^l}{(\omega_m-\Omega-i\gamma_m)(\omega_n-\omega-i\gamma_n)} + \frac{\Xi_{mn}\Delta_{n0}^l\Delta_{0m}^k}{(\omega_m-\omega+\Omega+i\gamma_m)(\omega_n-\omega-i\gamma_n)} \\ & + \frac{\Xi_{m0}\Delta_{nm}^l\Delta_{0n}^k}{(\omega_m+\Omega+i\gamma_m)(\omega_n-\omega+\Omega+i\gamma_n)} + \frac{\Xi_{m0}\Delta_{nm}^k\Delta_{n0}^l}{(\omega_m+\Omega+i\gamma_m)(\omega_n+\omega+i\gamma_n)} \\ & \left. + \frac{\Xi_{nm}\Delta_{0n}^l\Delta_{m0}^k}{(\omega_m+\omega-\Omega-i\gamma_m)(\omega_n+\omega+i\gamma_n)} \right]\end{aligned} \tag{2.58}$$

$$\chi_{kl}^{R}(\omega,\omega-\Omega)=\frac{1}{\hbar^2 N\upsilon_c}\sum_{mn}\Bigg[\frac{\Delta_{0m}^{k}\Xi_{mn}\Delta_{n0}^{l}}{(\omega_m-\omega+\Omega-i\gamma_m)(\omega_n-\omega-i\gamma_n)}$$
$$+\frac{\Delta_{0m}^{k}\Delta_{mn}^{l}\Xi_{n0}}{(\omega_m+\Omega-\omega-i\gamma_m)(\omega_n+\Omega-i\gamma_n)}+\frac{\Xi_{0n}\Delta_{nm}^{k}\Delta_{m0}^{l}}{(\omega_n-\Omega+i\gamma_n)(\omega_m-\omega-i\gamma_m)}$$
$$+\frac{\Delta_{m0}^{k}\Xi_{nm}\Delta_{0n}^{l}}{(\omega_m+\omega-\Omega+i\gamma_m)(\omega_n+\omega+i\gamma_n)}+\frac{\Delta_{m0}^{k}\Delta_{nm}^{l}\Xi_{0n}}{(\omega_m-\Omega+\omega+i\gamma_m)(\omega_n-\Omega+i\gamma_n)}$$
$$+\frac{\Xi_{n0}\Delta_{mn}^{k}\Delta_{0m}^{l}}{(\omega_n+\Omega-i\gamma_n)(\omega_m+\omega+i\gamma_m)}\Bigg] \tag{2.59}$$

Note that the tensor χ^R actually corresponds to the case when complex energies are used in Eq. (2.35), and it is thus the same as the Raman tensor in RS.

In transparent materials where $\gamma_m \to 0$ and $\gamma_n \to 0$, $\pi^R = \chi^R$, so the two Raman tensors are the same, both equal to the one in RS. However, in some opaque materials, π^R and χ^R can be quite different. In a resonant two-band process, considering only contributions from terms with two resonant denominators, which are the third term in Eq. (2.58) and the first term in Eq. (2.59), I have

$$\pi_{kl}^{R}(\omega,\omega-\Omega)=\sum_{n}\frac{\Delta_{0n}^{k}\Xi_0\Delta_{n0}^{l}}{\hbar^2 N\upsilon_c}\frac{1}{(\omega_n-\omega+\Omega+i\gamma_n)(\omega_n-\omega-i\gamma_n)} \tag{2.60}$$

$$\chi_{kl}^{R}(\omega,\omega-\Omega)=\sum_{n}\frac{\Delta_{0n}^{k}\Xi_0\Delta_{n0}^{l}}{\hbar^2 N\upsilon_c}\frac{1}{(\omega_n-\omega+\Omega-i\gamma_n)(\omega_n-\omega-i\gamma_n)} \tag{2.61}$$

Here I am assuming a constant deformation potential in the same band $\Xi_{nn}=\Xi_0$. Note the difference in the signs of γ's in the denominators. In some opaque materials, it is this sign difference that brings about quite different behaviors in RS and ISRS for the same sample.

A relationship can be drawn to relate the two stimulated Raman tensors with the relative permittivity of a material. With first order density matrix elements in Eq. (2.47), the relative permittivity is expressed as [18]

$$\varepsilon_{kl}(\omega) = 1 + 4\pi \sum_n \frac{\Delta_{0n}^k \Delta_{n0}^l}{\hbar N \upsilon_c} \frac{1}{\omega_n - \omega - i\gamma_n} \tag{2.62}$$

At the same time, I can rewrite Eq. (2.60) and Eq. (2.61) with

$$\frac{1}{(\omega_n - \omega + \Omega + i\gamma_n)(\omega_n - \omega - i\gamma_n)} = -\frac{1}{\Omega + i2\gamma_n}\left(\frac{1}{\omega_n - \omega + \Omega + i\gamma_n} - \frac{1}{\omega_n - \omega - i\gamma_n}\right) \tag{2.63}$$

$$\frac{1}{(\omega_n - \omega + \Omega - i\gamma_n)(\omega_n - \omega - i\gamma_n)} = -\frac{1}{\Omega}\left(\frac{1}{\omega_n - \omega + \Omega - i\gamma_n} - \frac{1}{\omega_n - \omega - i\gamma_n}\right) \tag{2.64}$$

Under the assumption that $\gamma_n \to 0$ and $|\Omega/\omega| \ll 1$, I have

$$\pi^R(\omega, \omega - \Omega) = \frac{\Xi_0}{4\pi\hbar}\left\{\frac{d\,\mathrm{Re}[\varepsilon(\omega)]}{d\omega} + i\frac{2\,\mathrm{Im}[\varepsilon(\omega)]}{\Omega}\right\} \tag{2.65}$$

$$\chi^R(\omega, \omega - \Omega) = \frac{\Xi_0}{4\pi\hbar}\left\{\frac{d\,\mathrm{Re}[\varepsilon(\omega)]}{d\omega} + i\frac{d\,\mathrm{Im}[\varepsilon(\omega)]}{d\omega}\right\} \tag{2.66}$$

Note that Eq. (2.65) and Eq. (2.66) are for fully symmetric modes. For modes of other symmetries, similar relationships can be derived [17].

In Sb and Bi at 800nm, $\left|d\,\mathrm{Re}[\varepsilon(\omega)]/d\omega\right|$~7-10eV^{-1}, $\left|d\,\mathrm{Im}[\varepsilon(\omega)]/d\omega\right|$~30-40eV^{-1} and $2\,\mathrm{Im}[\varepsilon(\omega)]/\Omega$~3000-4000eV^{-1} [19,20]. As a result, these crystals which give weak RS signals manifest large oscillations in a pump-probe experiment.

2.3.3 Coherent phonons in opaque materials and lifetime of the driving force

As concluded in Section 2.3.2, in an opaque material, the magnitude of the driving force for a coherent phonon field is determined by a different tensor from the one in RS. Another important implication of the theory lies in the specific temporal profile of the driving force. In a transparent material, the driving force is provided by the instantaneous electronic response to the incoming light, and thus has the same temporal shape as the pulse in Eq. (2.37). On the other hand, in an opaque material, the form of the driving force does not necessarily resemble the shape of the pulse. Instead, it has a displacive nature [17].

In a material which has $2\,\mathrm{Im}[\varepsilon(\omega)]/\Omega \gg \left| d\,\mathrm{Re}[\varepsilon(\omega)]/d\omega \right|$, substitute the expression of π^R in Eq. (2.65) back into Eq. (2.56) and get

$$F(t) = \frac{N\upsilon_c\,\mathrm{Im}(\varepsilon)\Xi_0}{4\pi\hbar}\int_{-\infty}^{t} |\,E_0(t')\,|^2\,dt' \tag{2.67}$$

This is a displacive force with an infinite lifetime. Now I add a decaying factor Γ to account for the finite lifetime such that

$$F(t) = \frac{N\upsilon_c\,\mathrm{Im}(\varepsilon)\Xi_0}{4\pi\hbar}\int_{-\infty}^{t} |\,E(t')\,|^2\,e^{-\Gamma(t-t')}dt' \tag{2.68}$$

where Γ is the decay rate of the force. The driving force is a convolution between the pump pulse intensity and a decaying response that follows it. For a Gaussian pulse

$$I(t) = \left|E(t)\right|^2 = (I_0/\sqrt{\pi}\tau_0)e^{-t^2/\tau_0^2} \tag{2.69}$$

I have

$$F(t) = VI_0\,\frac{\mathrm{Im}(\varepsilon)\Xi_0}{8\pi\hbar}\,\mathrm{erfc}\left(\frac{\Gamma\tau_0}{2} - \frac{t}{\tau_0}\right)\exp\left(\frac{\Gamma^2\tau_0^2}{4} - \Gamma t\right) \tag{2.70}$$

where $V = N\upsilon_c$. Fig. 2.5 shows the temporal evolution of driving forces with different Γ's generated by a Gaussian pulse arriving at $t = 0$. When Γ is small, the force looks like a step function with its rising edge broadened by the pulsewidth τ_0 and lasting as long as $1/\Gamma$. When Γ increases, the force gradually transforms to a Gaussian-like shape with its amplitude inversely related to the magnitude of Γ.

Using the solution provided by the Green's function given in Eq. (2.38), I can obtain a numerical solution for $Q(t)$, which is a set of damped oscillations with angular frequency Ω and decay rate b superimposed on a decaying background $\sim e^{-\Gamma t}$. Fig. 2.6 shows simulation results of $Q(t)$ for an oscillator with $\Omega = 2\pi \times 1.86\,\mathrm{THz}$ and $b = 0.21\,/\mathrm{ps}$ at $\Gamma = 0.1/\,ps$ and $\Gamma = 100/\,ps$. There is a significant drop by a factor of

9 in the phonon amplitude when the decay rate of the driving force increases by a factor of 1000.

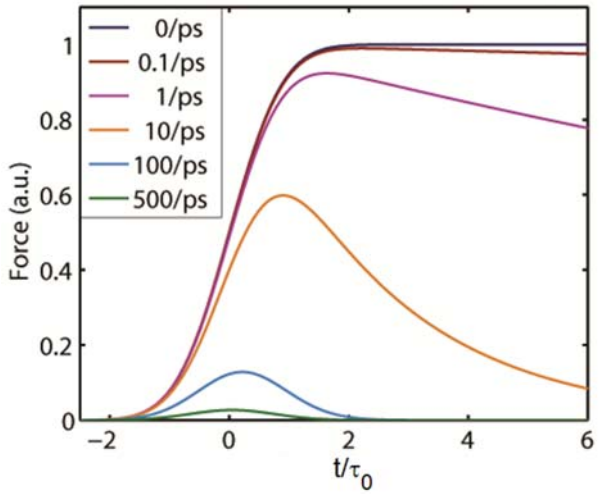

Figure 2.5. Simulation results of temporal evolution of driving forces with different decay rates generated by a Gaussian pulse with $\tau_0 = 42\text{fs}$ whose peak arrives at $t = 0$. Legends show different values of Γ used.

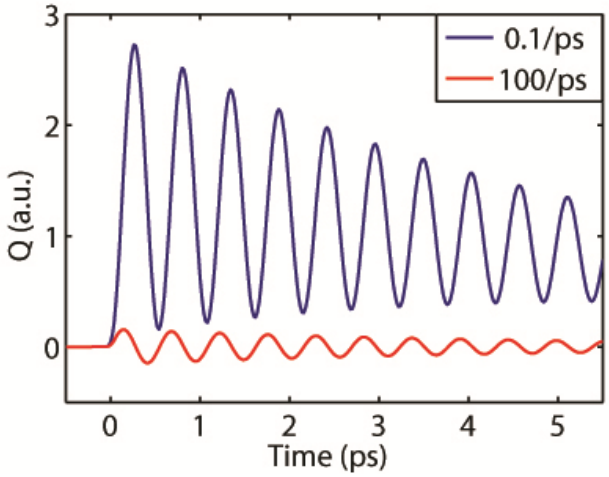

Figure 2.6. Simulation results of $Q(t)$ for an oscillator with $\Omega = 2\pi \times 1.86\ \text{THz}$ and $b = 0.21\,/\text{ps}$ when $\Gamma = 0.1/\ ps$ and $\Gamma = 100\,/\ ps$.

Another feature of the dependence of the initial phonon amplitude Q_0 on the decay

rate of the driving force is its different response sensitivities within different decay rate ranges. Fig. 2.7 shows the relationship between Q_0 and Γ for the same oscillator. It is noted that when Γ is much smaller than Ω, Q_0 is insensitive to the change of Γ. The amplitude is almost constant when Γ increases from 0 to 1/ps. However, when Γ is comparable to or larger than Ω, the increase of Γ brings down Q_0 drastically.

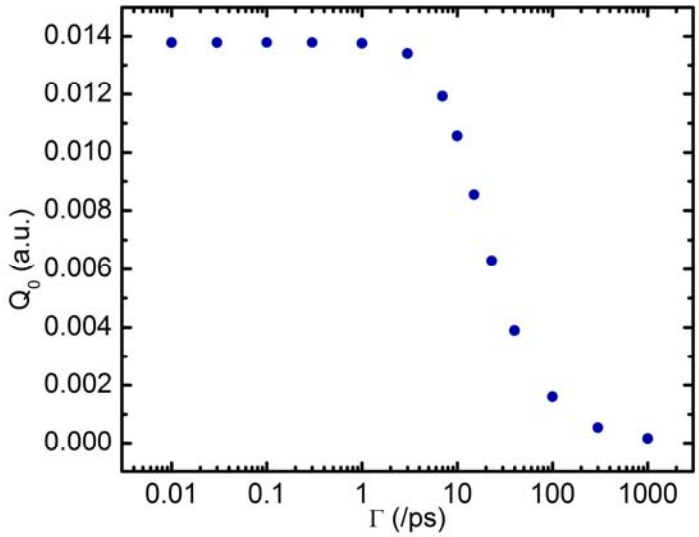

Figure 2.7. Initial amplitude of the oscillatory part of a phonon field with $\Omega = 2\pi \times 1.86\,\text{THz}$ and $b = 0.21\,/\text{ps}$ versus Γ.

Note that when $\Gamma \to 0$ and $b \ll \Omega$, a good approximation can be made for Q_0 as

$$Q_0 \approx VI_0 \frac{\text{Im}(\varepsilon)\Xi_0}{4\pi\hbar\Omega^2} e^{-\Omega^2\tau_0^2/4} \tag{2.71}$$

which is consistent with Eq. (12) in Ref [17]. Comparing Eq. (2.39) and Eq. (2.71), the magnitudes of Q_0 in an impulsive case and an extremely displacive case differ by a factor of Ω for their dependence on the phonon frequency.

If the pulsewidth is very short such that $\tau_0 \to 0$, Eq. (2.69) becomes

$$I = I_0 \delta(t) \tag{2.72}$$

and Eq. (2.70) becomes

$$F(t) = VI_0 \frac{\mathrm{Im}(\varepsilon)\Xi_0}{4\pi\hbar} \exp(-\Gamma t) H(t) \tag{2.73}$$

where $H(t)$ is the Heaviside step function. The force represented by Eq. (2.73) has a shape similar to those in Fig. 2.5 but with a sharper rising edge. With Eq. (2.73), I can achieve an analytical solution for $Q(t)$:

$$Q(t) = \frac{F_0 e^{-\Gamma t}}{\Omega^2 + (\Gamma - b)^2} - \frac{F_0 e^{-bt} \cos(\Omega t + \varphi)}{\Omega \sqrt{\Omega^2 + (\Gamma - b)^2}} \tag{2.74}$$

where

$$\tan\varphi = (\Gamma - b)/\Omega \tag{2.75}$$

and $F_0 = VI_0 \frac{\mathrm{Im}(\varepsilon)\Xi_0}{4\pi\hbar}$. In this limit, it is easy to see that the coherent phonon signal is a superposition of a decaying background and a damping oscillator, and the analytical form of Q_0 can be directly extracted. Moreover, the dependence of Q_0 on Γ as shown in Fig. 2.7 is clearly revealed by the denominator of the second term. Also, in the limit that $\Gamma \to 0$ and $b \ll \Omega$, the initial amplitude of the second term is reduced to Eq. (2.71) with the difference of a factor $e^{-\Omega^2\tau_0^2/4}$ which accounts for the pulsewidth.

For opaque materials, differential reflectance of a probe beam is usually measured, and it follows from Eq. (11) in Reg. [17]

$$\frac{\Delta R}{R} \approx \frac{1}{R}\frac{\partial R}{\partial E_c} \Xi_0 e^{-\Omega^2\tau_0^2/4} Q(\Delta t) \tag{2.76}$$

where E_c is the central frequency of the probe pulse. The factor $e^{-\Omega^2\tau_0^2/4}$ is a correction for the pulsewidth of the probe beam similar to the correction in Eq. (2.71).

2.4 Summary

The mathematics that formulates lattice vibrations into quantized phonons within the

framework of harmonic oscillators was presented in this chapter. The macroscopic and microscopic theoretical treatments for spontaneous Raman scattering and impulsively stimulated Raman scattering were reviewed, too. I also discussed the differences in the behaviors of coherent phonon fields in transparent and opaque materials, which originates from the virtual and real charge densities fluctuations in the optical excitations. Excitations below and above the bandgap induce different forms of Raman tensors that influence both the amplitude and the temporal profile of a driving force. Those fundamental theories are crucial for reasonable comparison and interpretation of experimental data from RS and ISRS experiments in following chapters.

References

[1] C. Kittel, *Introduction to Solid State Physics* (John Wiley & Sons, Inc., New York, 1986).

[2] M. Born and K. Huang, *Dynamical Theory of Crystal Lattices* (Clarendon Press, Oxford, 1956).

[3] M. Fox, *Optical Properties of Solids* (Oxford University Press, Oxford, 2001).

[4] R. E. Peierls, *Quantum Theory of Solids* (Clarendon Press, Oxford, 1955).

[5] P. Y. Yu and M. Cardona, *Fundamentals of Semiconductors* (Springer, Berlin, 1996).

[6] G. A. Garrett, Ph.D. thesis, University of Michigan, 2001.

[7] W. Hayes and R. Loudon, *Scattering of Light by Crystals* (John Wiley & Sons, Inc., New York, 1978).

[8] R. Merlin, Solid State Communications **102**, 207 (1997).

[9] R. Loudon, Proceeding of the Royal Society of London A **275**, 218 (1963).

[10] R. Loudon, Advances in Physics 13, 42382 (1964).

[11] W. Richter, in *Solid State Physics*, edited by G. Höhler, Springer Tracts in Modern Physics Vol. 78 (Springer, Berlin, 1976).

[12] J. M. Ralston, R. L. Wadsack and R. K. Chang, Physical Review Letters **25**, 814 (1970).

[13] J. Menéndez and M. Cardona, Physical Review Letters **51**, 1297 (1983).

[14] C.-F. Chen, C.-H. Park, B. W. Boudouris, J. Horng, B. Geng, C. Girit, A. Zettl, M. F. Crommier, R. A. Segalman, S. G. Louie and F. Wang, Nature 471, 617 (2011).

[15] H. Vogt, in *Light Scattering in Solids II*, edited by M. Cardona and G. Güntherodt, Topics in Applied Physics Vol. 50 (Springer, Berlin, 1982).

[16] Y. R. Shen and N. Bloembergen, Physical Review **137**, A1787 (1965).

[17] T. E. Stevens, J. Kuhl and R. Merlin, Physical Review B **65**, 144304 (2002).

[18] R. W. Boyd, *Nonlinear Optics* (Academic Press, San Diego, CA, 2003).

[19] M. Cardona and D. L. Greenaway, Physical Review **133**, A1685 (1964).

[20] J. B. Renucci, W. Richter, M. Cardona and E. Schönherr, Physica Status Solidi (b) **60**, 299 (1973).

CHAPTER 3

Experimental Techniques

This chapter discusses the experimental equipments and techniques that have been extensively used in the lab. The working principle and structure of various continuous wave (CW) lasers and ultrafast systems are introduced in section 3.1. Raman spectroscopy and pump-probe spectroscopy are presented in section 3.2 and section 3.3 respectively. Some other methods such as pulsewidth characterization, cryogenic technique and linear prediction are considered in section 3.4-3.6.

3.1 Lasers

Lasers are the key parts of all the experimental setups referenced in this dissertation. To investigate spontaneous Raman scattering (RS) and stimulated Raman scattering, both continuous wave lasers and ultrafast laser systems are used.

3.1.1 Argon ion laser

RS experiments are performed using the output from a CW Argon ion laser (Spectra Physics Beamlok 2060). RS in the visible range is performed using the single-line output from the Argon laser, while RS in the near infrared range is performed with a Ti:sapphire solid-state laser pumped by the multi-line output from the Argon laser.

An electric discharge is used to pump the Argon laser. The transitions in an Argon laser follow a typical 4-level lasing scheme, a simplified diagram of which is shown in Fig. 3.1 (a). An Ar atom is excited to a 4p state by two collisions with electrons: the first collision ionizes the Ar atom, and the second collision excites Ar^+ ion directly to its 4p

state or to higher energy levels which quickly cascade to 4p. Then transitions between 4p and 4s give several wavelengths in the visible range, between 400nm and 600nm. A spectrum of the atomic transitions frequencies is shown in Fig. 3.1 (b). The ion finally transitions from the 4s state to its ground state by emitting a photon in the UV range (~74nm) [1,2].

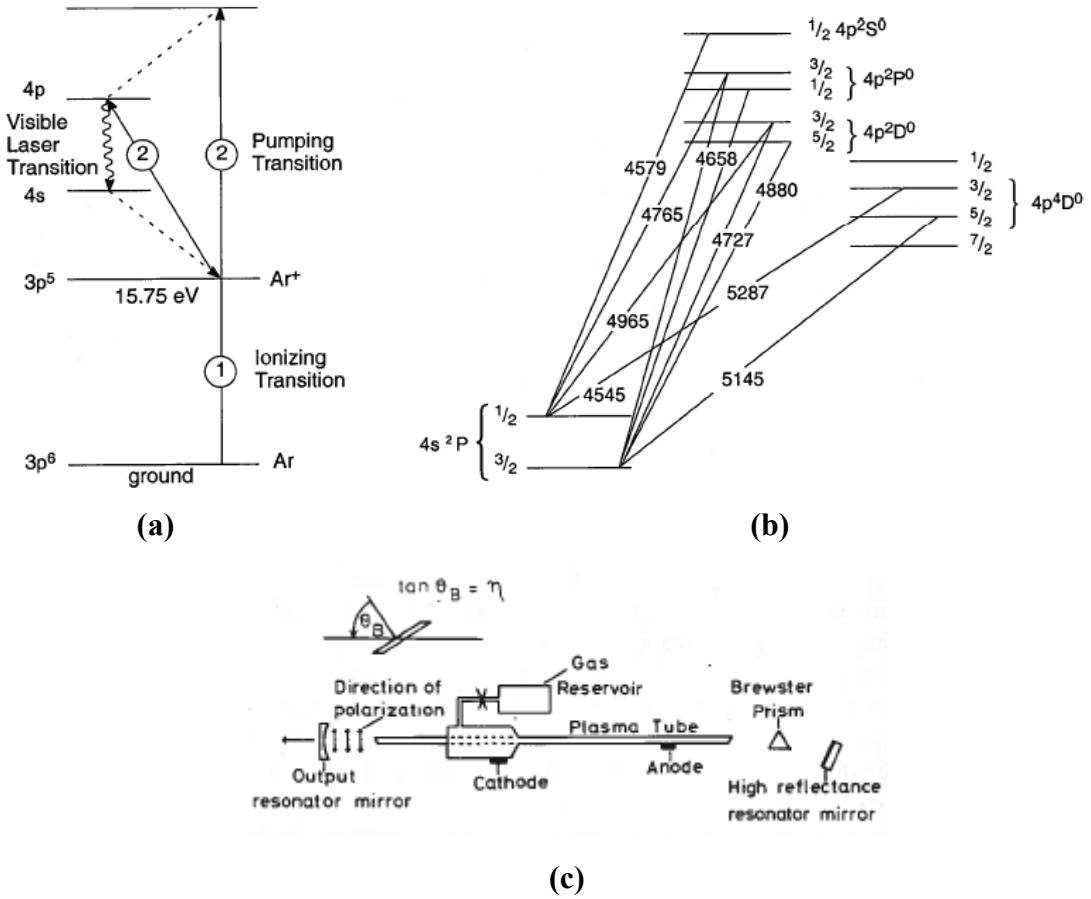

Figure 3.1. Working principle for an Argon gas laser. (a) The 4-level atomic transition scheme in an Argon laser [1]. (b) Energy levels of the 4p-4s Argon laser transitions in the visible range [1,2]. (c) Schematic graph of a gas laser. The insert shows the Brewster angle θ_B [3].

The end windows of the plasma tube are aligned in the Brewster angle so that the output of the laser is polarized in the plane of incidence, as in the insert of Fig. 3.1 (c).

When operating in the visible range, a prism is inserted in the cavity. This is called "single-line" setup since due to the dispersion of the prism, there is only one wavelength perfectly aligned with the high reflector and thus preferentially amplified. By adjusting the tilt of the high reflector, different wavelengths can be selected. When more power is needed in order to pump a Ti:sapphire laser, the prism is replaced by a broadband high reflector covering wavelength in the range 454.5nm-514.5nm. This "multi-line" setup allows lasing at several wavelengths simultaneously and provides more output power. A gas fill reservoir automatically detects and keeps the optimum pressure inside the plasma tube [1].

3.1.2 Neodymium-doped Yttrium Orthovanadate (Nd:YVO_4) solid state laser

A Nd:YVO_4 solid state laser (Coherent Verdi V-5/V-10) is usually used for pumping a Ti:sapphire oscillator or a regenerative amplifier. A schematic graph of the laser cavity is shown in Fig. 3.2.

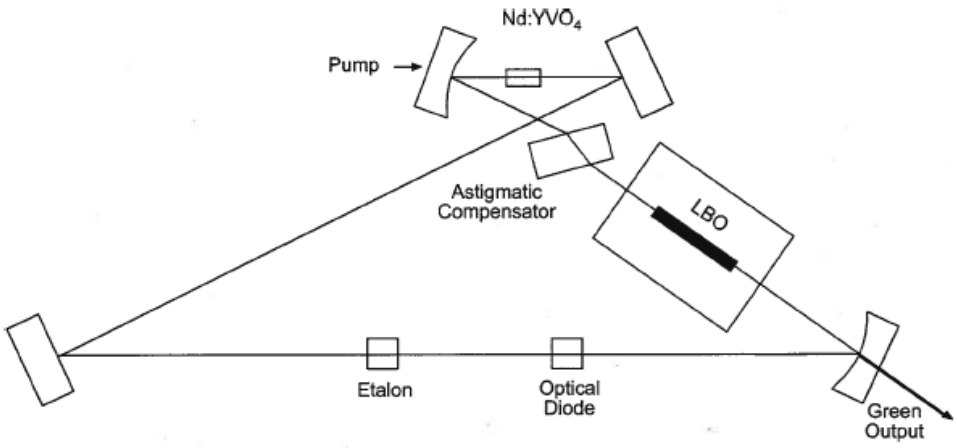

Figure 3.2. Schematic graph of an end-pumped ring laser cavity of a Nd:YVO_4 laser [4].

The Nd:YVO_4 laser is pumped by laser light around 808nm delivered by optical fibers from semiconductor laser diode bar modules (FAP-I^{TM}) located in the power supply. The gain medium is an Nd^{3+}-doped YVO_4 crystal. The transition from $^4F_{3/2}$ to $^4I_{11/2}$ produces light at a wavelength around 1064nm [5]. An optical diode guarantees that

the beam gets amplified in one direction in the cavity and hence guarantees single frequency operation, which is reinforced by an etalon. The 1064nm beam is converted to 532nm beam by second harmonic generation after passing a type I non-critically phase matched lithium triborate (LBO) doubling crystal. The fundamental and frequency-doubled beams travel collinearly until a dichromatic mirror reflects the 1064nm beam and transmits the 532nm beam as the output [4].

3.1.3 Ti: sapphire mode-locked ultrafast oscillator

The Ti:sapphire mode-locked ultrafast oscillator (Coherent Mira Seed Laser) is a solid state laser usually used for seeding a regenerative amplifier. It utilizes Kerr lens passive mode-locking technique to generate laser pulses with repetition rate 76MHz, pulsewidth 70fs, and tunable wavelength from 780 to 840nm. The wavelength usually used is 800nm and pulses typically have a bandwidth around 30nm. A schematic graph of the oscillator cavity is shown in Fig. 3.3.

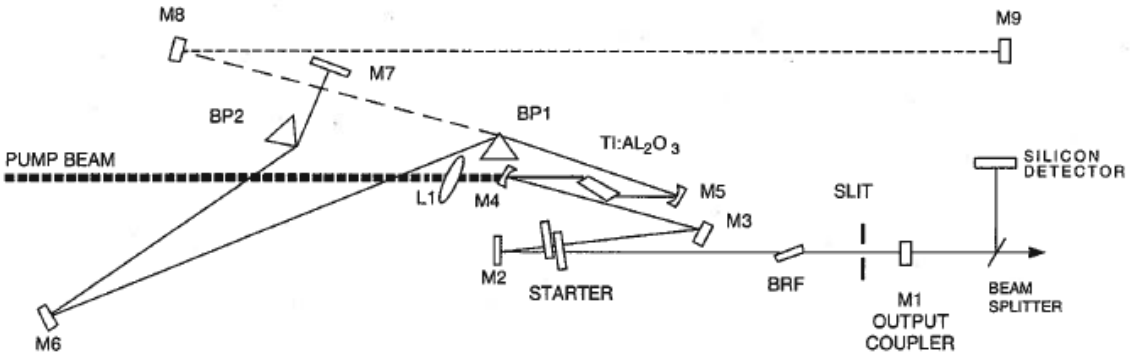

Figure 3.3. Schematic graph of a Mira seed laser [6].

The Ti:sapphire oscillator uses Ti^{3+} doped sapphire crystal as the gain medium pumped by the frequency-doubled CW output at 532nm from a Nd:YVO_4 solid state laser (Coherent Verdi V-5). The broad gain curve of Ti:sapphire amplifies light from 680nm to 1100nm. Cavity end mirrors and a birefringent filter narrow the spectrum to around 30nm. There is a glass starter in the optical path. By rocking the starter and thus

changing the effective cavity length, more than one longitudinal mode can be made to lase simultaneously, hence inducing transient power fluctuation big enough to cause the Kerr lens effect. That is how the mode-locking starts. After the pulses are initiated, the starter oscillation is halted and prism BP2 is adjusted to optimize the GVD and to provide a stable power output. Due to the nonlinear self-focusing effect in the sapphire crystal, laser pulses have a smaller diameter where a hard aperture sits, and thus passes through the aperture with lower round-trip loss; CW signals suffers from spatial beam-loss due to their low peak intensity and larger spot size. Pulsed output is significantly amplified in this way. A fused silica prism pair (BP1 and BP2) is used to compensate for the positive intracavity group velocity dispersion (GVD) as well as the chirp induced by self-phase modulation (SPM) in the crystal. The repetition rate, 76MHz, is determined by the time that a pulse takes to finish one round-trip in the laser cavity [6].

3.1.4 Ti: sapphire regenerative amplifier

The Ti: sapphire regenerative amplifier (Coherent RegA 9000) provides μJ pulse energy at 800nm and high repetition rate up to 250kHz. It is desirable for white-light continuum generation and experiments that require high pulse energy. A schematic of RegA is shown in Fig. 3.4 (a).

The RegA is seeded by a Mira oscillator and pumped by a CW frequency-doubled Nd:YVO4 solid state laser (Coherent Verdi V-10) at 532nm. Population inversion is created in the Ti: sapphire crystal while lasing is inhibited by an 80MHz radio-frequency (RF) modulated TeO_2 Q-switch. The acoustic wave in the TeO_2 crystal is aligned at the Bragg angle so that it diffracts part of the beam out of the cavity when the acousto-optic modulation is on. In this way, the loss of the cavity is high and most of the pumped energy is accumulated in the Ti:sapphire crystal instead of participating in lasing. It is only immediately before a cavity dumper lets in a seeding pulse until immediately after the cavity dumper lets out an amplified pulse that the Q-switch is held off so that light amplification takes place inside the cavity. The cavity dumper is a 380MHz RF

modulated Brewster angled SiO_2 crystal. When an RF pulse is sent to the cavity dumper, the acoustic wave inside the crystal diffracts a stretched seeding optical pulse into the cavity. After 25 to 30 round trips, another RF pulse is sent and the amplified pulse is diffracted out. The acoustic pulse is so short that only one pulse out of the 76MHz pulse train is injected each time. The timing schematic for the Q-switch and cavity dumper is shown in Fig. 3.4 (b). A dispersion compensated Faraday isolator is present in the way of the seeding pulses to stop the back reflected pulses from going back to Mira. The repetition rate 250kHz is limited by the storage time of the gain medium, which is 2.5 μ s for Ti:sapphire at room temperature [7].

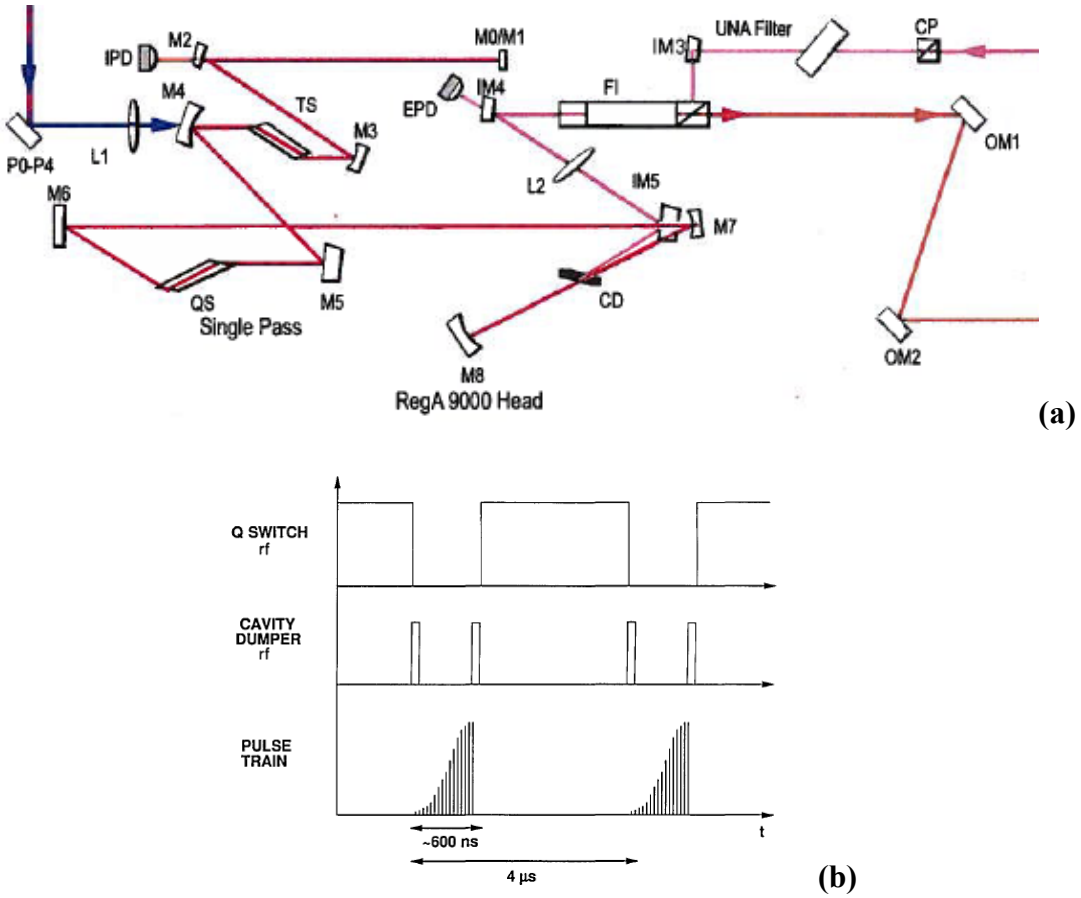

Figure 3.4. Schematic graph of a regenerative amplifier. (a) Ti:sapphire regenerative amplifier optical schematic. QS: Q-switch, TS: Ti:sapphire, CD: cavity dumper, FI: Faraday isolator, CP: cube polarizer [7]. (b) Timing sequence of the Q-switch, cavity dumper and intracavity optical pulse train [8].

Chirped-pulse amplification is used to amplify the energy in each pulse. The pulse train from Mira is sent to a 4-pass holographic diffraction grating expander before being injected into the RegA. The pulsewidth is stretched to 10-100ps in order to reduce undesirable nonlinear effects such as gain saturation and SPM in the process of pulse amplification. After amplified by the RegA, pulses are sent to another 4-pass grating compressor to be converted to an ultrafast pulse train with 70fs pulsewidth. The GVD of a light beam passing through a grating pair, no matter positive or negative, is determined by the same expression. A setup for pulse compression uses a positive distance between the grating pair and hence gains a negative GVD; to get a positive GVD as in a grating pulse expander, the image of the first grating that is behind the second grating is made use of so that a negative distance can be achieved.

3.1.5 Optical parametric amplifier

The optical parametric amplifier (Coherent OPA 9400) provides continuously tunable pulsed output with visible signal from 480nm to 700nm and infrared idler from 933nm to 2300nm. The repetition rate is 250kHz and output power is around 30mW. A schematic of the OPA is shown in Fig. 3.5.

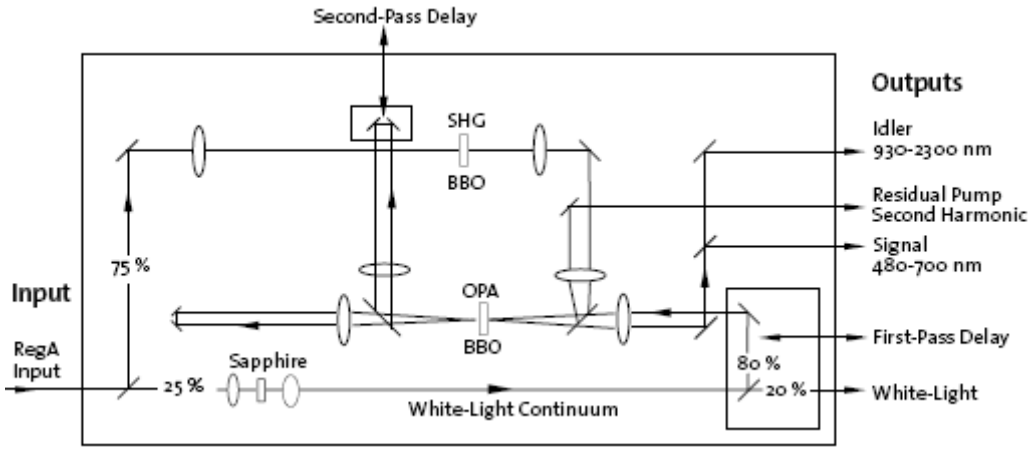

Figure 3.5. Schematic graph of an OPA [10].

The 800nm horizontally polarized output from RegA is split into two beams upon arriving in the OPA. One beam with 25% of the power is focused on a sapphire crystal to generate a white light continuum. The high intensity of the Gaussian beam induces a Kerr lens due to self-focusing modulation (SFM). The focused beam collapses into a symmetric Gaussian filament with the size close to the wavelength when the effect of diffraction balances that of SFM. The high intensities in the collapsed filament causes self-phase modulation (SPM). It generates a frequency and phase sweep exceeding the fundamental laser wavelength, which extends from ultraviolet to near infrared. Both SFM and SPM are due to the third-order susceptibility $\chi^{(3)}$ which contributes to a intensity dependent refractive index $n = n_0 + n_2 I$, where n_0 is the weak-field refractive index, n_2 is called the second-order index of refraction, and I is the time-averaged intensity of the optical field [11]. For SFM, when n_2 is positive, according to the Gaussian spatial profile of a beam, the refractive index at the center is higher than at the periphery. As a result, a positive lens is formed and the beam is focused. In the case of SPM, the strong field also induces a nonlinear phase change when the beam propagates, given by $\phi_{NL}(t) = -n_2 I(t)\omega_0 L / c$, where ω_0 is the optical angular frequency, L is the distance light travels in the material, and c is the speed of light. It adds an instantaneous variation to the original optical angular frequency ω_0 given by $\delta\omega = d\phi_{NL}(t)/dt$ [11]. Due to the specific shape of a Gaussian pulse, the leading part of the pulse induces lower frequencies and thus extends to IR, while the tailing induces higher frequencies and extends to UV. In this way, the high laser intensity introduces new frequencies and broadens the spectrum of the beam.

The other beam with 75% of the power is sent to a 1mm thick type I Beta-Barium Borate (BBO) and converted to a second harmonic generated (SHG) beam at 400nm with

a vertical polarization. SHG involves the second-order susceptibility $\chi^{(2)}$ and is a special case of sum-frequency generation. The nonlinear polarization has twice the frequency of the incoming field $P(t) = \chi^{(2)} E^2 e^{-i2\omega_0 t} + c.c.$, where E is the amplitude of the fundamental electric field [11].

The white-light continuum, usually called the seed, and the second harmonic 400nm beam, called the pump, are then both focused on a type I BBO crystal. When phase-matching for certain wavelength within the continuum is satisfied, the high frequency 400nm beam is converted into a beam at that specific wavelength and another beam called the idler. The intensities of seed and idler beams grow when they passes through the crystal. This difference frequency generation process is known as optical parametric amplification, which is also a $\chi^{(2)}$ process. Fig. 3.6 (a) shows the amplification geometry and 3.6 (b) the energy levels involved.

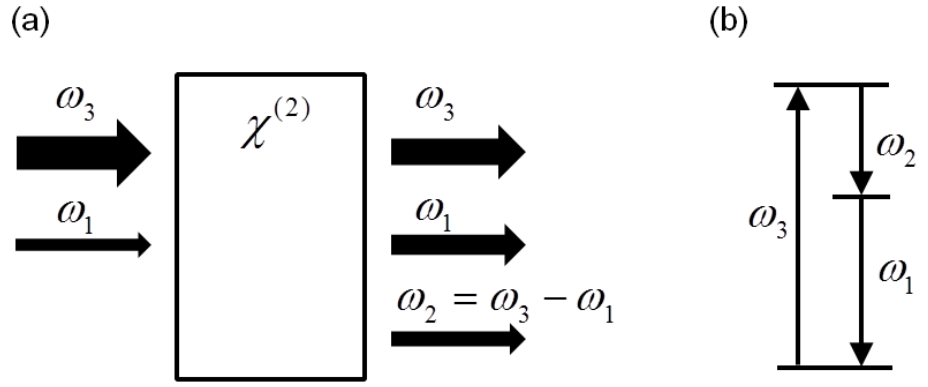

Figure 3.6. (a) Geometry schematic of the optical parametric amplification interaction. A pump beam with frequency ω_3 is converted to a seed beam with ω_1 and an idler with ω_2. (b) Energy level description of the process.

Phase-matching is realized by angle-tuning of the OPA BBO crystal. It utilizes the birefringence of the crystal to compensate for the normal dispersion of light in materials.

Equations which describe conservation of energy and momentum are

$$\omega_3 = \omega_1 + \omega_2 \tag{3.1}$$

$$k_3 = k_1 + k_2 \tag{3.2}$$

where ω_3, ω_1, and ω_2 are the frequencies for the pump, the seed and the idler, and k_3, k_1, and k_2 are the corresponding wavevectors. ω and k are related by $k = n\omega / c$. In the normal dispersion regime of a isotropic crystal, n is an increasing function of ω, so phase-matching conditions Eq. (3.1) and Eq. (3.2) are hard to achieve simultaneously. The difficulty is overcome by making use of the birefringence of BBO. In the case of BBO, which is a negative uniaxial crystal, Eq. (3.2) can be rewritten as

$$n_3^e(\theta)\omega_3 = n_1^o\omega_1 + n_2^o\omega_2 \tag{3.3}$$

where n^o is ordinary refractive index and $n^e(\theta)$ the extraordinary refractive index. The optic axis of BBO is in the plane of incidence, which is vertical. The seed and idler are both polarized in the horizontal direction and have refractive indices independent of the crystal orientation. On the other hand, the vertically polarized pump experiences a variable refractive index when the crystal orientation is changed [12]

$$\frac{1}{n_3^e(\theta)^2} = \left(\frac{\cos\theta}{n_3^o}\right)^2 + \left(\frac{\sin\theta}{\overline{n}_3^e}\right)^2 \tag{3.4}$$

where $\overline{n}^e$ is the principal value of the extraordinary refractive index and θ is the angle between the optic axis and k_3. In practice, by tuning the BBO orientation, different wavelengths that satisfy the phase-matching condition are selected and amplified. As shown in Fig. 3.5, optimal bandwidth and power are achieved by sending both beams through the BBO crystal twice [13]. Positions of the delay stages in the two passes can be adjusted to match the lengths of the optical paths of the pump and the seed in order to maximize the output power.

3.2 Raman scattering spectroscopy

A Raman spectrometer is a conventional tool for characterizing optical phonons as well as photoluminescence in the frequency domain. It has the advantage of high resolution, high sensitivity and convenience of operation. As a result, it serves as a quick and reliable way for testing the orientation of samples, selection rules, etc.

3.2.1 SPEX Raman spectrometer

The Raman spectrometer SPEX (0.85m double SPEX 1404) contains two 1800 grooves/mm holographic gratings, two alternative entrances, a water cooled photomultiplier tube (PMT) for signal detection, several relay curve mirrors and four slits. It has spectral coverage 175-1040nm and resolution 0.005nm. Fig. 3.7 shows the standard setup for a double-grating SPEX Raman spectrometer.

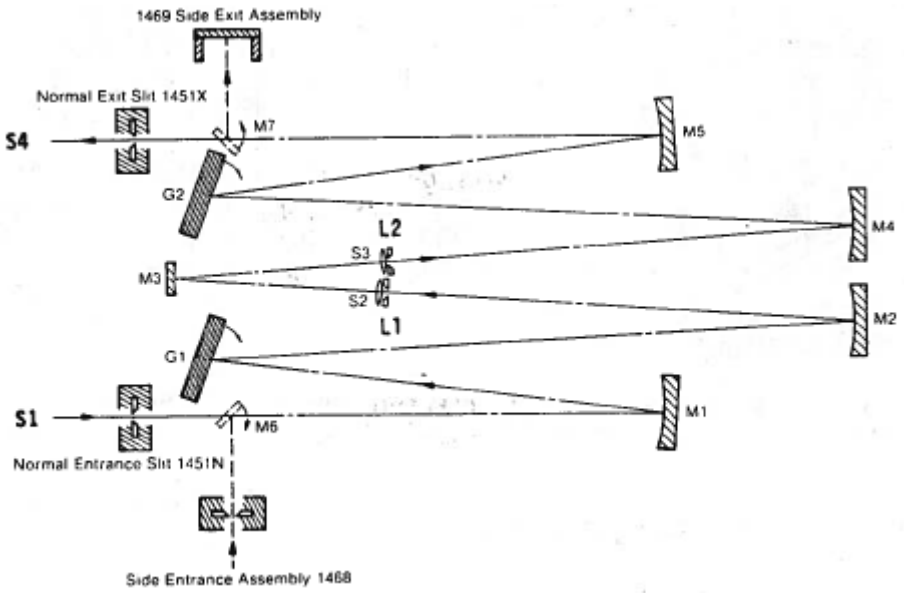

Figure 3.7. Schematic for SPEX. G1 and G2 are gratings, M1, M2, M3 and M4 are curve mirrors [14].

The scattered light from the samples are collected and focused on the entrance slit S1. After the diffraction by grating G1, the dispersed spectrum is sent through L1 and L2,

which are important at shielding off the strong laser line. The beam is then sent to another grating G2 and gets diffracted again. The selected wavelength is sent through an exit slit S4 and into a PMT. The spectrometer has a high resolution due to the use of two grating for spectrum dispersion. The resolution is determined by the sizes of slit S1 and S4, which are normally set equal. S2 and S3 are usually 20% wider than S1 and S4. Two rods are used to control S2 and S3 respectively. When they are pulled out, S2 and S3 are fully open. When they are pushed in, the widths of S2 and S3 are controlled by the micrometers outside the SPEX. A swingaway mirror M5 is used to switch between the two entrances.

3.2.2 Dilor Raman spectrometer

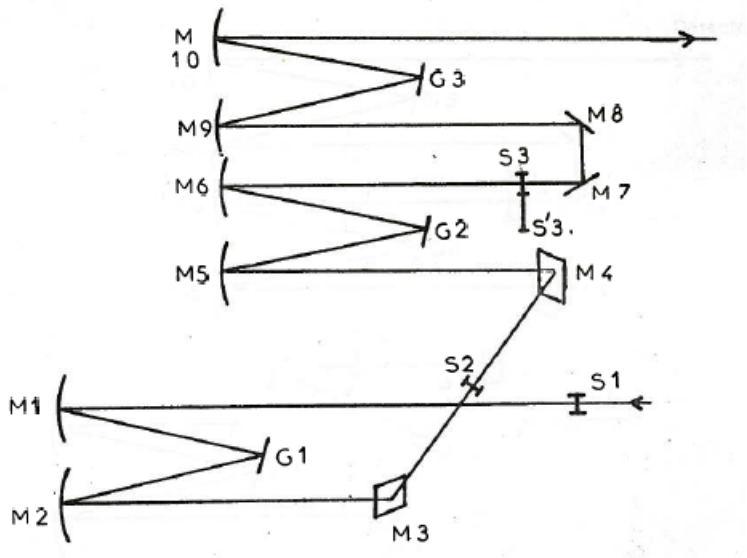

Figure 3.8. Dilor setup at multichannel normal mode [15].

Dilor XY (JY Horiba) has the advantage of high efficiency over SPEX because it can take data over a frequency range instead of at a single frequency at one time. This is because Dilor uses a charge-coupled device (CCD) camera for signal detection, referred as "multichannel" detection. It contains a 1024×256 pixel array and averages signals from pixels on the same column at each frequency. The liquid nitrogen cooled CCD has a

low background noise. However, the CCD camera is less sensitive than a PMT, and the Dilor has lower resolution than the SPEX due to the single grating diffraction scheme it uses. A schematic of Dilor with "normal mode" setup is shown in Fig. 3.8.

Scattered light from a sample is collimated by a lens outside Dilor and sent to the entrance. There is an internal lens that focuses the light on slit S1. The beam is then diffracted by grating G1, goes through a widely open slit S2, and then another grating G2, which is conjugate to G1 and regroups different wavelengths at slit S3. G1 and G2 are controlled by the same motor and always kept coupled. They constitute the "premonochromator" part that functions as a bandpass filter that selects a spectrum range via S2. Grating G3, which constitutes the "spectrograph" part, is controlled by another motor. It diffracts the light coming from S3 to the CCD camera. The resolution of Dilor is limited by the width of S1 and S3.

3.2.3 Raman spectroscopy

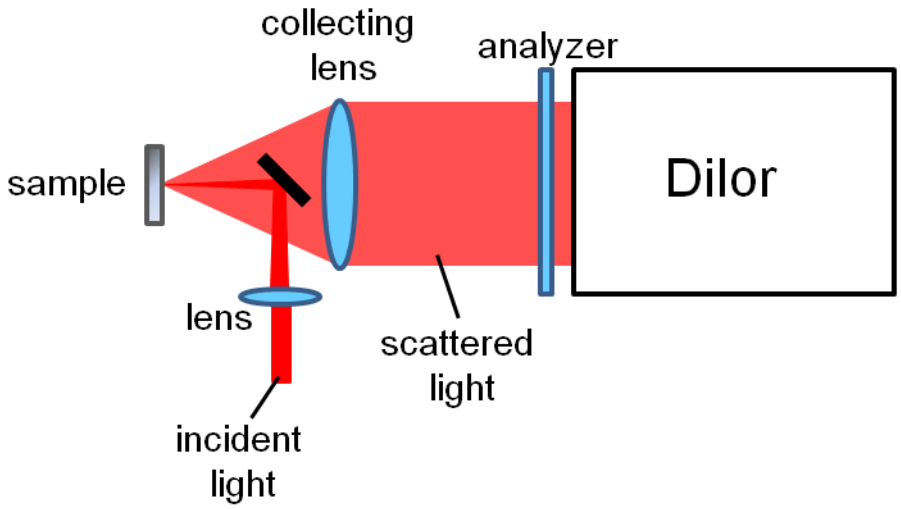

Figure 3.9. Standard setup for Raman backscattering geometry using Dilor. The different colors used for incident light and scattered light are only for illustration clarity.

For opaque materials, backscattering geometry is usually used. With this geometry, the focused incident light comes in a direction very close to the normal of the sample

surface. The sample sits at the focus of a collecting lens so that the scattered light is collimated and sent to the spectrometer. A polarizer usually called an analyzer is placed in front of the spectrometer to pick up light of certain polarization. Fig. 3.9 shows a standard setup for Raman backscattering geometry using Dilor.

The input to S1 of the SPEX should be a focused point of the scattered light, so either a focusing lens is needed between the collecting lens and SPEX, or the collecting lens and focusing lens are replaced by a single lens that carries out the functions of both. In either case, the lens should be carefully chosen to match the f/# of the SPEX. A mirror target mask is available and can be placed over M1 as a reference point to facilitate precise alignment of the optical path outside the spectrometer.

For transparent materials, in addition to backscattering, other geometries such as forward scattering and right-angle scattering can be employed to meet the requirement of the phenomena of interest and corresponding selection rules. Multiple reflections of light inside the sample should be taken into account when one calculates cross sections and phase matching conditions [16,17].

The conventional notation used to describe the scattering geometry in an RS experiment is $\mathbf{k}_I(\mathbf{e}_I,\mathbf{e}_S)\mathbf{k}_S$, where $\mathbf{k}_I$ and $\mathbf{k}_S$ are the directions of incident and scattered light, $\mathbf{e}_I$ and $\mathbf{e}_S$ are the corresponding polarizations [18].

3.3 Ultrafast pump-probe spectroscopy

Ultrafast pump-probe spectroscopy has been widely used to depict temporal behavior of fundamental excitations such as optical phonons, acoustic phonons, magnons, polaritons and photoexcited carriers [19-25]. A pump beam is used to excite these phenomena in a sample, and a probe that follows behind is used to detect the change of the optical properties induced by these phenomena, usually in the form of spectra shift, change of reflectance or transmittance, or change of the polarization of the probe beam.

An example of the most commonly used standard degenerate pump-probe setup in reflection detection geometry is shown in Fig. 3.10 (a). The 800nm pulsed beam from a Ti:sapphire regenerative amplifier with 70fs pulsewidth and 250kHz repetition rate is split into a pump beam and a probe beam. An optical chopper is used to modulate the intensity of the pump beam at 2kHz. A beamsplitter is inserted in the probe beam to split it into a reference beam and a detection probe beam. Both the pump and the detection probe beam are focused at the same spot on the sample. The reflected detection probe beam and the reference beam are sent to the two channels of a balanced photodetector, where the difference between the two intensities is taken. The output of the photodetector is sent through a 10kHz low-pass pre-amplifier and then into a lock-in amplifier with the same reference frequency as the optical chopper. Since the optical path of the probe beam involves a delay stage, the temporal delay between a pump pulse and a probe pulse can be controlled by changing the position of the delay stage by step sizes as small as $0.1\ \mu\text{m}$. Depending on the specific requirement of an experiment, parameters such as the polarizations and wavelengths of the pump and probe beam can be adjusted as needed.

One of these modifications is the detection of anisotropic signals in the reflection geometry, as shown in Fig. 3.10 (b). It is usually referred to as Kerr geometry since it detects the rotation of the polarization of the probe beam [26]. In this setup, instead of a beamsplitter, a half waveplate is inserted in the probe beam to change its polarization to 45^{o}, while the polarization of the pump beam is kept horizontal. No reference beam is used. The reflected probe beam is split by a polarizing cube beamsplitter into two beams with vertical and horizontal polarizations, and then sent to the two channels of a balanced photodetector. This setup is especially useful in isolating small anisotropic signals from a large isotropic background, since vertically and horizontally polarized parts of the probe beam see different modulations induced by the anisotropic excitation but the same modulations induced by the isotropic excitation.

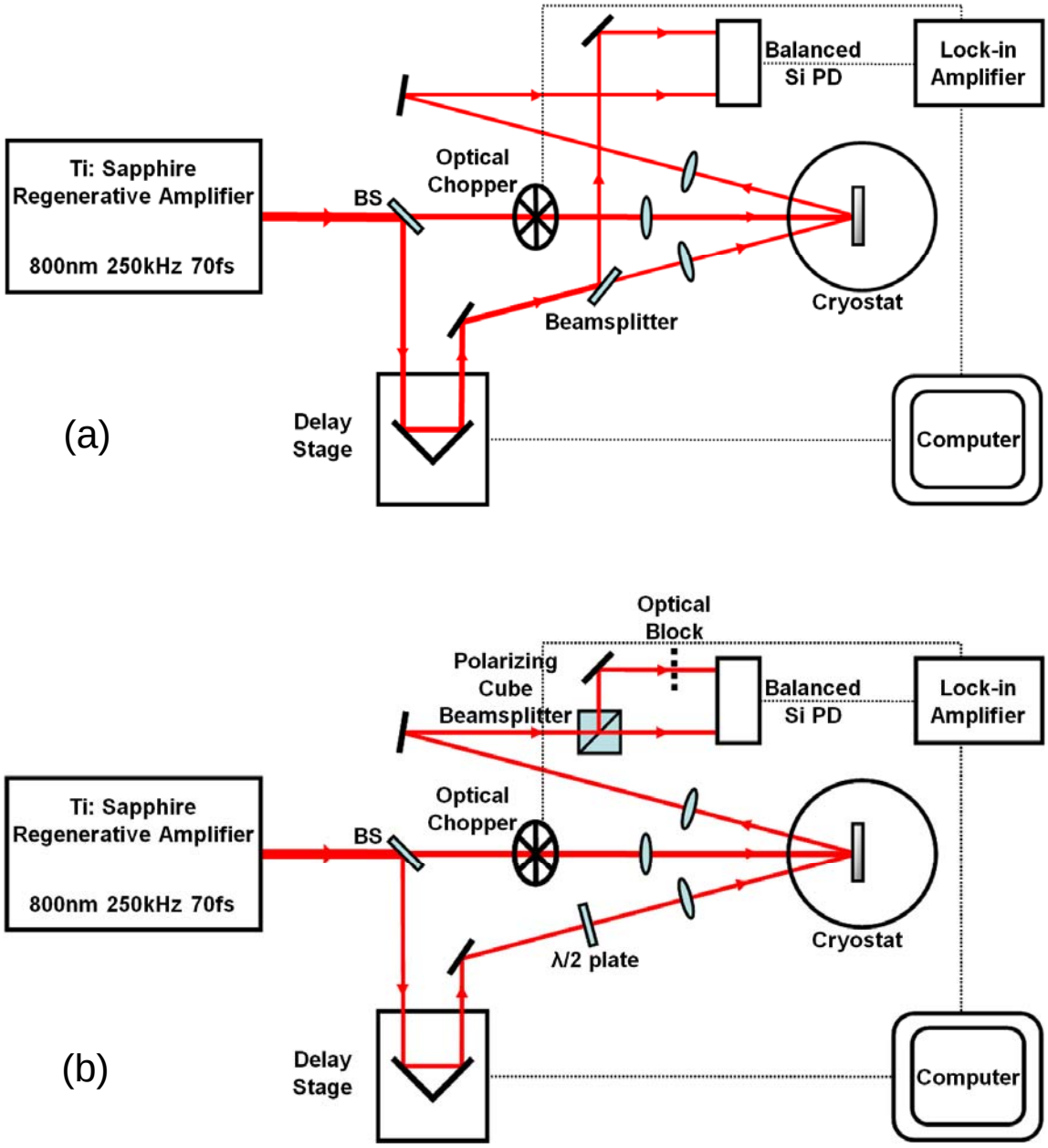

Figure 3.10. (a) Standard degenerate pump-probe setup in the reflection detection geometry. (b) Degenerate pump-probe setup for detection of anisotropic signals in the Kerr reflection geometry.

An analogy can be drawn when transmission from the sample is of interest. In this case, the major effect of coherent optical phonons is to shift the spectrum of the beam. As a result, if a photon counter is used as the detection device, the spectrally integrated

signal can be small since there is no change in the total number of photons. To get signals of good quality, a spectral filter or a grating is placed in the path of the transmitted probe to sample a portion of the spectra [19,27].

3.4 Pulsewidth characterization

Pulsewidth is an important factor that influences the efficiency of coherent phonon generation as well as the temporal resolution of a pump-probe experiment. One of the techniques that characterize pulsewidth is the crosscorrelation between the pump and the probe beams. A noncollinear setup similar to Fig. 3.9 (a) in the transmission geometry is used and a BBO crystal is placed where the sample sits. A photodetector is put behind the BBO to detect the transmitted crosscorrelation signal generated by SHG. By changing the time delay between the two beams, a temporal profile of the second harmonic generated light is obtained.

Assuming the two beams have the same temporal profile, the intensity of the SHG signal is

$$I^{(2)}(\Delta t) = C\int_{-\infty}^{+\infty} I(t)I(t-\Delta t)dt \tag{3.5}$$

where Δt is the temporal separation of the two beams, and C is the conversion efficiency. Assuming a Gaussian pulse

$$I(t) = I_0 e^{-t^2/\tau_0^2} \tag{3.6}$$

we have

$$I^{(2)}(\Delta t) = I_0^{(2)} e^{-(\Delta t)^2/2\tau_0^2} \tag{3.7}$$

where $I_0^{(2)} = C\tau_0 I_0^2\sqrt{\pi}/\sqrt{2}$.

The pulsewidth τ_p is conventionally defined as the full width at half maximum (FWHM) of the pulse intensity envelope in Eq. (3.6), so that

$$\tau_p = 2\sqrt{\ln 2}\tau_0 \tag{3.8}$$

Note that the FWHM $\tau_{FWHM}^{(2)}$ of the autocorrelated signal in Eq. (3.7) is $\sqrt{2}$ times that of the individual pulse intensity

$$\tau_{FWHM}^{(2)} = \sqrt{2}\tau_p \tag{3.9}$$

3.5 Cryostat

All the temperature dependent experiments in this thesis were carried out with the samples placed inside a flow-helium cryostat (Janis ST-300) under vacuum around 2×10^{-6} Torr. With the combination of a cold finger sample mount cooled by liquid helium and a heater placed close to the mount, a very stable temperature can be achieved from 10K to room temperature.

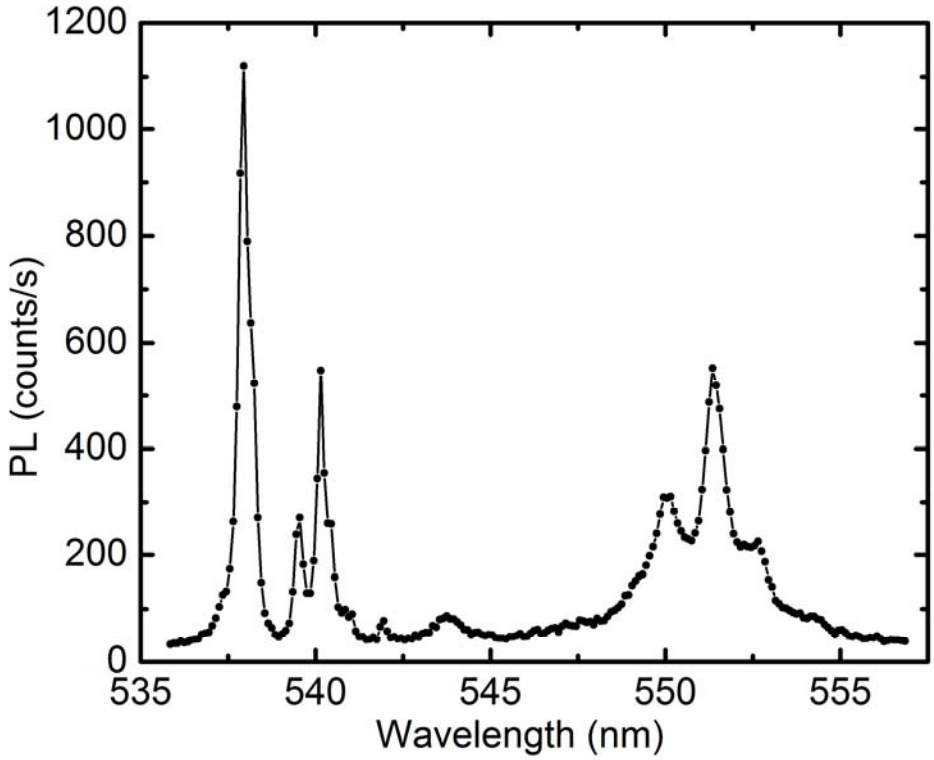

Figure 3.11. Photoluminescence spectrum of a CaF_2 window in the range 535nm-557.5nm taken with SPEX with excitation wavelength 514.5nm.

Scattering from the CaF_2 windows on the outer jacket of the cryostat is rarely a problem, since the focus of the collecting lens in an RS experiment does not rest on the window and the reflected beams from the window and the sample are spatially separated in an ISRS experiment. However, in an RS experiment, if the sample is mounted very close to the window or the signal from the sample is quite weak, care should be taken concerning the photoluminescence (PL) from the CaF_2 window. Fig. 3.11 shows part of the PL spectrum of the CaF_2 window taken with SPEX with an excitation wavelength of 514.5nm at room temperature. CaF_2 is well known for its large bandgap around 12eV [28] and is thus widely used in making optical windows and lenses in the visible and IR range. The PL peaks from the windows coincide with transitions of ionic impurities in the CaF_2 crystal [29].

3.6 Data analysis: linear prediction method

Typical data from a pump-probe experiment is in the form of differential reflectance or transmittance x_n as a function of time with the same step size Δt. The signal is usually a sum of several damping harmonic oscillatory modes, electronic background and noise. Due to the finite time window of the experimental data, fast Fourier transform (FFT) suffers from limited frequency resolution [30]. What is more, oscillations are usually accompanied by some decaying electronic background, which in frequency domain shows up as a low frequency signal with a tail that distorts the peaks of interest [27].

A singular value decomposition based linear prediction (LPSVD) procedure is used to extract oscillators from the signal with high frequency resolution and high numerical stability. At the same time, it also provides other information about the oscillations such as decay rate, initial amplitude and initial phase. LPSVD method needs no initial values to carry out the fitting process. The following section explains the mathematical principle of LP method described in Ref. [30].

For a time sequential signal representing K oscillators of the form

$$x_n \equiv x(n\Delta t) = \sum_{k=1}^{K} c_k e^{-b_k n\Delta t} \cos(\omega_k n\Delta t + \varphi_k) + w_n \tag{3.10}$$

where c_k, b_k, ω_k and φ_k are the initial amplitude, decay rate, angular frequency and initial phase of the k th oscillator, w_k is the noise. Backward LPSVD prediction assumes that the n th point can be expressed as a linear combination of its following M points such that [31]

$$x_n = a_1 x_{n+1} + a_2 x_{n+2} + \cdots + a_M x_{n+M} \tag{3.11}$$

where the linear coefficients $a_1 \cdots a_M$ are independent of n. If the noise is zero, $M = 2K$. However, with noise, M can far exceed $2K$. In the LPSVD program, we use $M = N/2$. We can thus write $N - M$ functions of the same form as Eq. (3.11) and solve the linear problem

$$\mathbf{X}_{(N-M)\times M}\mathbf{a}_{M\times 1} = \mathbf{x}_{(N-M)\times 1} \tag{3.12}$$

The solution is

$$\mathbf{a} = \mathbf{V}\tilde{\mathbf{\Lambda}}^{-1}\tilde{\mathbf{U}}\mathbf{x} \tag{3.13}$$

where $\mathbf{U}$ and $\mathbf{V}$ are orthogonal matrices, $\mathbf{\Lambda}$ is a diagonal matrix, and $\tilde{\mathbf{U}}$ denotes transposition of $\mathbf{U}$. Note that $\tilde{\mathbf{\Lambda}}^{-1}$ is defined as

$$\mathbf{\Lambda}\tilde{\mathbf{\Lambda}}^{-1} = \begin{vmatrix} \mathbf{E}_l & 0 \\ 0 & 0 \end{vmatrix} \tag{3.14}$$

where $\mathbf{E}_l$ is a unit matrix with dimension $l \times l$, the meaning of l to be explained later. The matrices are got from singular value decomposition (SVD) of $\mathbf{X}$

$$\mathbf{X}_{(N-M)\times M} = \mathbf{U}_{(N-M)\times(N-M)}\mathbf{\Lambda}_{(N-M)\times M}\tilde{\mathbf{V}}_{M\times M} \tag{3.15}$$

The diagonal entries λ's of $\mathbf{\Lambda}$ are called singular values (SV's) of $\mathbf{X}$. Without noise, there are $2K$ non-zero SV's. The noise adds to the matrix more non-zero but very small

SV's, which make the condition number $\lambda_{\max} / \lambda_{\min}$ high and renders a numerically unstable problem [32]. As a result, truncation is performed to get the largest l SV's, which are the values actually used to solve Eq. (3.13).

Once $\mathbf{a}$ is solved, its components are used to form a M th order equation

$$z^M - a_1 z^{M-1} - \cdots - a_M = 0 \tag{3.16}$$

The k th complex root z_k of Eq. (3.15) is related to the parameters of an oscillator

$$b_k = \ln\left[\mathrm{mod}(z_k)\right] / \Delta t \tag{3.17}$$

$$\omega_k = \pm \arg(z_k) / \Delta t \tag{3.18}$$

z_k larger than unity in Eq. (3.17) and a proper sign in Eq. (3.18) should be chosen to guarantee positive decay rates and frequencies. Sorting is usually performed over all the roots at this stage and only l roots with the largest moduli are retained to achieve physically meaningful solutions [30].

Once we have b's and ω's, they are inserted back to Eq. (3.10). We then get N linear equations about $c_k \cos\varphi_k$ and $c_k \sin\varphi_k$ with coefficients $d_{n,2k-1} = e^{-b_k n\Delta t}\cos(\omega_k n\Delta t)$ and $d_{n,2k} = -e^{-b_k n\Delta t}\sin(\omega_k n\Delta t)$. By solving the equations with another linear least square procedure, we can derive c's and φ's from pairs of solutions.

References

[1] *BeamLok 2060/2080 User's Manual* (Spectra-Physics, A Division of Newport Corporation, Mountain View, California, 1997).

[2] W. B. Bridges, Applied Physics Letters **4**, 128 (1964).

[3] W. Hayes and R. Loudon, *Scattering of Light by Crystals* (John Wiley & Sons, Inc., New York, 1978).

[4] *Operator's Manual Verdi^{TM} V-2/V-5/V-6 Diode-Pumped Lasers* (Coherent, Inc., Santa Clara, California, 2002).

[5] A. W. Tucker, M. Birnbaum, C. L. Fincher and J. W. Erler, Journal of Applied Physics **48**, 4907 (1977).

[6] *Operator's Manual The Coherent Mira Seed Laser* (Coherent, Inc., Santa Clara, California, 2005).

[7] *Operator's Manual RegA Model 9000 Laser* (Coherent, Inc., Santa Clara, California, 1997).

[8] T. B. Norris, Optics Letters **17**, 1009 (1992).

[9] O. E. Martinez, IEEE Journal of Quantum Electronics **QE-23**, 59 (1987).

[10] *Operator's Manual The Coherent Model 9400 Optical Parametric Amplifier (OPA)* (Coherent, Inc., Santa Clara, California, 1998).

[11] R. W. Boyd, *Nonlinear Optics* (Academic Press, San Diego, CA, 2003).

[12] A. Yariv and P. Yeh, *Optical Waves in Crystals: Propagation and Control of Laser Radiation* (John Wiley & Sons, Inc., New York, 1984).

[13] M. K. Reed, M. K. Steiner-Shepard, M. S. Armas and D. K. Negus, Journal of the Optical Society of America B **12**, 2229 (1995).

[14] *SPEX Operation & Maintenance Instructions* (Industries, Inc., Metuchen, New Jersey, 1981).

[15] *User Manual Dilor XY Modular Laser Raman Spectrometer* (Instruments S. A. Jobin Yvon, Edison New Jersey).

[16] W. Richter, in *Solid State Physics*, edited by G. Höhler, Springer Tracts in Modern Physics Vol. 78 (Springer, Berlin, 1976).

[17] A. Bianchini, Ph.D. thesis, University of Michigan, 2012.

[18] P. Y. Yu and M. Cardona, *Fundamentals of Semiconductors* (Springer, Berlin, 1996).

[19] R. Merlin, Solid State Communications **102**, 207 (1997) and references therein.

[20] J. Zhao, A. V. Bragas, D. J. Lockwood and R. Merlin, Physical Review Letters **93**, 107203 (2004).

[21] D. M. Wang, Y. H. Ren, X. Liu, J. K. Furdyna, M. Grimsditch and R. Merlin, Physical Review B **75**, 233308 (2007).

[22] M. Trigo, T. A. Eckhause, J. K. Wahlstrand, R. Merlin, M. Reason and R. S. Goldman, Applied Physics Letters **91**, 023115 (2007).

[23] T. E. Stevens, J. K. Wahlstrand, J. Kuhl and R. Merlin, Science **291**, 627 (2001).

[24] W. Z. Lin, R. W. Schoenlein, J. G. Fujimoto and E. P. Ippen, IEEE Journal of Quantum Electronics **24**, 267 (1988).

[25] J. Shah, *Ultrafast Spectroscopy of Semiconductors and Semiconductor Nanostructures* (Springer, Berlin 1999) and references therein.

[26] S. A. Crooker, D. D. Awschalom and N. Samarth, IEEE Journal of Selected Topics in Quantum Electronics **1**, 1082 (1995).

[27] J. K. Wahlstrand, Ph.D. thesis, University of Michigan, 2005.

[28] G. W. Rubloff, Physical Review B **5**, 662 (1972).

[29] C. S. Kartha, T. Ramachandran, V. P. N. Nampoori and K. Sathianandan, Solid State Communications **59**, 461 (1986).

[30] H. Barkhuijsen, R. D. Beer, W. M. M. J. Bovée and D. V. Ormondt, Journal of Magnetic Resonance **61**, 465 (1985).

[31] Eqn. (2) in Ref. [30] is for forward prediction.

[32] L. N. Trefethen and D. Bau, III, Numerical Linear Algebra (SIAM: the Society for Industrial and Applied Mathematics, Philadelphia, 1997).

CHAPTER 4

Temperature and Fluence Dependence of Coherent Optical Phonons in Semimetals

Ultrafast lasers have been widely used to characterize phonons with THz frequencies in a variety of materials [1-5]. Based on the diverse phenomena under study, different generation mechanisms of coherent phonon oscillations were identified and theoretically formulated [5-11]. For example, impulsively stimulated Raman scattering (ISRS) is well-known for exciting phonons in transparent or molecular crystals [2,12,13]; LO phonons in certain semiconductors such as GaAs are initiated by screening of the surface electric field by photoexcited carriers [11,14,15]. Among all the discussions, one topic over which has been debated for a long time is the nature of the generation mechanism for lattice vibrations in certain opaque materials with low crystal symmetry [8,10,16-19].

The question originated from the first few ultrafast time-resolved experiments in Sb, Bi, Te and Ti_2O_3 [16,17], when large oscillations of A_1 (or A_{1g}) modes were seen while other modes observable in spontaneous Raman scattering (RS) were missing in the pump-probe experiments performed. The results led to the subsequent proposal of the theory of displacive excited coherent phonons (DECP) [6], which claimed that coherent phonons in those materials are generated by a different process from those in Raman scattering. It was argued that lattice vibrations are initiated because of a displaced quasiequilibrium coordinate of the nuclear system set by the photoexcited carriers, and this mechanism only applies to breathing modes which do not change the symmetry of the crystal. Later, experimental observation of E_g modes in Sb [8] and Bi [18], and the related

theoretical development [8] proved that the generation process involved in these semimetals is actually a particular case of coherent stimulated Raman scattering excited on resonance, which can generate modes of arbitrary symmetry. Afterward, the theory of two stimulated Raman tensors led to a microscopic interpretation of Raman tensors involved in the generation and scattering processes of a pump-probe experiment [10]. This theory combined impulsive excitations in transparent materials with displacive excitations in absorbing materials under the framework of Raman scattering, and pointed out that the difference in those two scenarios lies in different contributions to the driving force from virtual and real transitions when materials are excited below and above the bandgap. A wavelength dependent measurement of the coherent phonons in Sb revealed the relationship between the permittivity of an opaque material and the Raman tensors involved in a pump-probe experiment. After that, a model incorporating a finite lifetime of the driving forces was developed to explain the starting phases of coherent phonons in Si and some other materials [20]. However, according to that method, the initial phases of the oscillations need to be accurately determined, which is usually obtained with certain errors in a pump-probe experiment due to the ambiguity of the exact temporal overlap between the pump and the probe. At the same time, the resolution of the anisotropic part of electronic excitation is also limited by the pulsewidth used.

In this chapter, by investigating A_{1g} and E_g modes in Sb and Bi, I propose another approach to estimate the lifetime of the carrier density with E_g symmetry. This method is based on the initial amplitudes of coherent phonons, which is more robust against the ambiguity of zero time delay determination. A set of temperature dependent pump-probe data and RS data in Sb and Bi will be shown. Different behaviors of A_{1g} and E_g modes are observed in pump-probe data. Based on the framework of two stimulated Raman tensors and infinite lifetime of the driving force, a discrepancy of deformation potentials derived from pump-probe experiments and RS experiments is observed. As a result, the finite lifetime of the E_g driving force needs to be taken into account. By comparing

results from pump-probe and RS experiments, lifetimes of the E_g driving forces around and below 10fs were resolved with the 70fs laser pulses used. Section 4.1-4.6 will discuss the topic above based on the selection rules, experimental results and relevant symmetry interpretation.

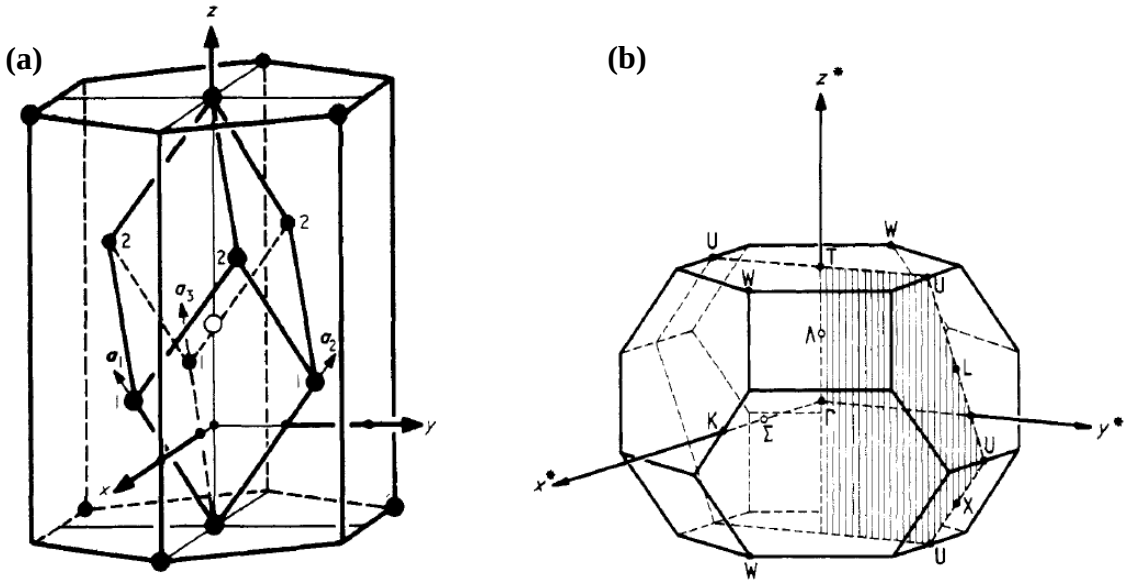

Figure 4.1. (a) A unit cell of Sb [25]. Solid circles correspond to atoms from sublattice one. Only one atom from sublattice two is shown, which is the open circle within the unit cell. The center of inversion symmetry lies at the origin of the orthogonal axis system. The z axis is along the trigonal axis of the crystal. (b) The first Brillouin zone of Sb with high symmetry points and lines [25].

In addition to the work related to the ongoing debate concerning the generation mechanism, some interesting works on other aspects of coherent phonons have also been carried out using ultrafast techniques. One of the intensively studied topics is the nature of phonon chirp in these materials at high fluence [21-24]. In a pump-probe experiment at high fluence, Bi shows a temporally changing frequency, which can be explained by lattice anharmonicity and electronic softening [21,23]. The relative importance of the electronic softening over lattice anharmonicity was confirmed by a double pump-probe experiment on the A_{1g} mode of Bi [24]. However, the chirp of the E_g mode has not been investigated to the best of our knowledge. In section 4.7, fluence dependent data on both

A_{1g} and E_g modes in Sb will be presented. A summary is given in section 4.8.

4.1 Crystal structure of antimony (Sb) and bismuth (Bi)

Sb and Bi are group Vb semimetals with rhombohedral A7 crystal structure and point group $\bar{3}m$ [8]. The crystal can be viewed as derived from two inter-penetrating face centered cubic lattices, with both lattices slightly stretched along the body diagonal (which becomes the trigonal axis of the crystal), and one lattice displaced relative to the other along the trigonal axis. There are two atoms in each unit cell, and the center of inversion symmetry lies midway between these two atoms [25]. The Brillouin zone (BZ) of the rhombohedral crystal is thus a slightly squashed version of the BZ of an fcc crystal. A unit cell of Sb is shown in Fig. 4.1 (a) and its first Brillouin zone is in Fig. 4.1 (b).

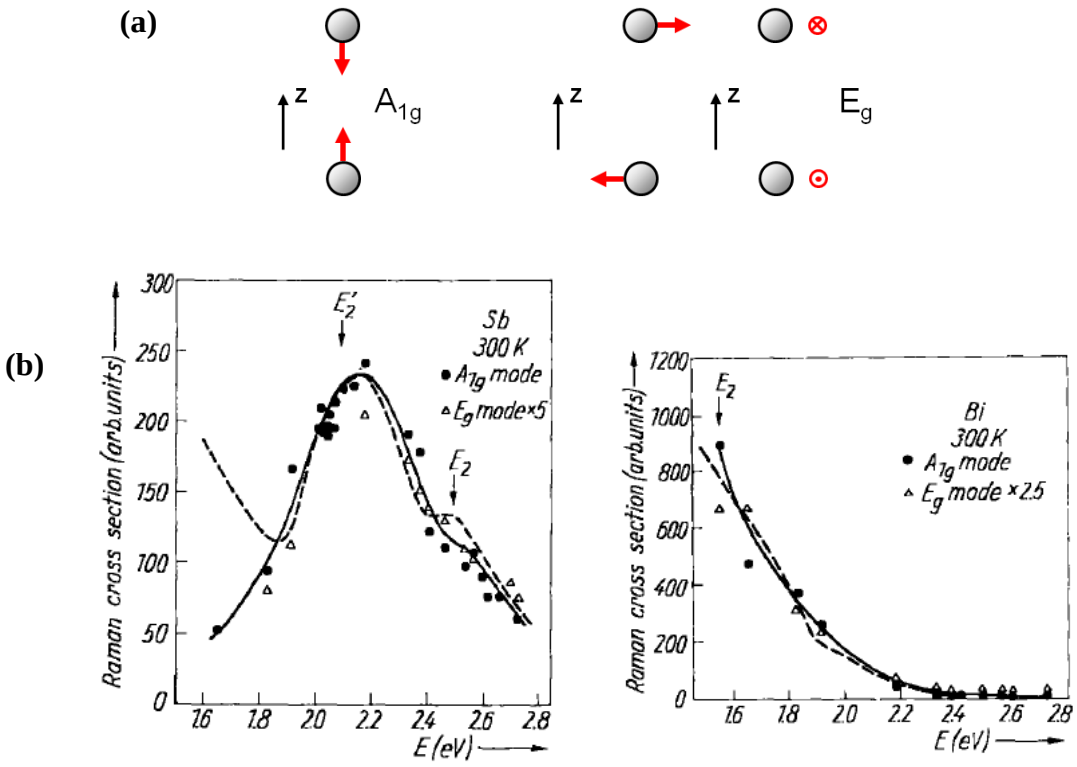

Figure 4.2. (a) Schematic illustrations of atomic motion corresponding to the non-degenerate A_{1g} mode and the doubly degenerate E_g modes. (b) Raman cross section of A_{1g} and E_g modes in Sb and Bi at 300K as a function of incident photon energy [26].

4.2 Phonon modes in Sb and Bi

Having 2 atoms in each unit cell, Sb and Bi have 6 phonon branches, 3 acoustic phonons and 3 optical phonons. Among the 3 Raman active optical phonons, there is one totally symmetric A_{1g} mode and two doubly degenerate E_g modes. The motion of atoms in a unit cell corresponding to each mode are schematically shown in Fig. 4.2 (a). Previous studies showed that two-band processes are dominant in these materials [26]. One evidence is that the ratio of the Raman cross section between A_{1g} and E_g modes in both materials is constant over a large range of incident photon energy, as shown in 4.2 (b). The optical excitation involved is believed to take place in a wide region of the Brillouin zone, rather than confined to any high symmetry points [26]. The Raman tensors for these modes are shown in Table 4.1 [8].

Table 4.1. Raman tensors for the A_{1g} (nondegenerate) and E_g (doubly degenerate) modes in crystals with point group $\bar{3}m$. The trigonal axis of the crystal is oriented in the z direction.

A_{1g} $\begin{pmatrix} a & 0 & 0 \\ 0 & a & 0 \\ 0 & 0 & b \end{pmatrix}$	E_g $\begin{pmatrix} 0 & e & 0 \\ e & 0 & d \\ 0 & d & 0 \end{pmatrix}$	$\begin{pmatrix} e & 0 & -d \\ 0 & -e & 0 \\ -d & 0 & 0 \end{pmatrix}$

4.3 Experimental setups

Our samples are a 1mm thick Sb single crystal and a 100nm Bi single crystal film deposited on a sapphire substrate. They were mounted in a Janis ST-300 cryostat with surfaces perpendicular to the trigonal axis. A surface of good optical quality is important in the successful observation of E_g modes and well-observed selection rules. Temperature dependent pump-probe and RS experiments were performed on these samples.

In the pump-probe experiments, I used the anisotropic detection geometry in Fig. 3.10 (b). A 2.2mW pump and a 0.5mW probe beam were focused to a 200um and 80um

diameter spot respectively on the sample, with incident angles 0^o and 13^o. Sometimes for a sample with an inhomogeneous surface, signals from different spots can be different, so detections of isotropic signals and anisotropic signals from the same spot are important. In our experiment, for detection of the weak E_g signals, both entrances of the photodetector are open; for detection of the A_{1g} signals, only the entrance receiving the vertically polarized beam was open. The reference provided by the optical chopper was 4kHz.

In the RS experiment, I used a continuous wave Ti:sapphire laser operating at 780nm pumped by an Argon gas laser in the multiline mode. A backscattering geometry $z(x,x)\bar{z}$ was employed with a 30mW vertically polarized incident beam. The scattered light was filtered with a vertically polarized analyzer and then sent to a Dilor X-Y Raman spectrometer, with slit size 200um for both S1 and S3.

4.4 Selection rules

According to Eq. (2.71) and Eq. (2.76), the initial amplitude of phonon oscillations in a differential reflectance pump-probe experiment is

$$\frac{\Delta R}{R} \propto \left(\sum_{kl} e^k_{pump} \pi_{kl} e^l_{pump} \right) \left(\sum_{kl} e^k_{probe} \chi_{kl} e^l_{probe} \right) \tag{4.1}$$

where π_{kl} and χ_{kl} are the two stimulated Raman tensors in Chap. 2, $\mathbf{e}_{pump}$ and $\mathbf{e}_{probe}$ are the polarization unit vectors for the pump and the probe fields. For $\mathbf{e}_{pump} = (\cos\alpha, \sin\alpha, 0)$ and $\mathbf{e}_{probe} = (\cos\beta, \sin\beta, 0)$, the signals for A_{1g} mode and E_g mode are

$$A_{1g}: \quad (\Delta R/R)_a \propto \pi_a \chi_a \tag{4.2}$$

$$E_g: \quad (\Delta R/R)_e \propto \pi_e \chi_e \cos\left[2(\alpha - \beta)\right] \tag{4.3}$$

where the subscripts a and e represent A_{1g} and E_g modes respectively. Note that the

A_{1g} signal is independent of the polarization of either beam while the E_g signal is dependent on the angle between the polarizations of the pump and probe beams. Neither phonon signal depends on the angle between the light polarization and the crystal axis in plane. In our specific polarization geometry, the E_g signal obtained is twice the maximum amplitude in Eq. (4.3).

According to Eq. (2.30), the Raman scattering cross section in an RS experiment is

$$\frac{d^2\sigma}{d\Omega_{solid} d\omega_S} \propto \left| \sum_{kl} e_S^k \chi_{kl} e_I^l \right|^2 \tag{4.4}$$

where $\mathbf{e}_I$ and $\mathbf{e}_S$ are the polarization unit vectors for the incident and the scattered fields. Raman cross sections one gets with an incident beam $\mathbf{e}_I = (\cos\gamma, \sin\gamma, 0)$ and scattered light $\mathbf{e}_S = (\cos\psi, \sin\psi, 0)$ are

$$A_{1g}: \quad \left(d^2\sigma / d\Omega_{solid} d\omega_S \right)_a \propto \chi_a^2 \cos^2(\gamma - \psi) \tag{4.5}$$

$$E_g: \quad \left(d^2\sigma / d\Omega_{solid} d\omega_S \right)_e \propto \chi_e^2 \tag{4.6}$$

Again, neither signal depends on the orientation of the axis in plane. The A_{1g} signal depends on the angle between the polarizations of the incident and scattered light while the E_g signal is polarization insensitive.

4.5 Temperature dependent experimental data

Temperature dependent pump-probe signals from Sb and Bi are shown in Fig. 4.3-4.6. An A_{1g} mode with frequency 4.5THz and an E_g mode with frequency 3.4THz are observed in Sb at room temperature. Similarly, an A_{1g} mode at 2.9THz and an E_g mode at 2.1THz are observed in Bi. These frequencies shift to higher values at lower temperature. A large electronic background can be observed in the A_{1g} data in both materials. A flat background is observed in the E_g data due to the cancellation of the isotropic electronic background. The initial amplitude of A_{1g} oscillations in Sb is almost constant from room

temperature to 10K, while the initial amplitude of E_g oscillations increases by a factor of 2.5. Similar behaviors are observed in Bi. The amplitude of the A_{1g} mode stays the same over the entire temperature range except for a slight decrease at 10K while that of the E_g mode increases by a factor of 4.

I fit the oscillatory part of the signal with the linear prediction method with the model

$$\Delta R / R = \sum_i A_i \exp(-b_i t)\cos(\Omega_i t + \varphi_i) \tag{4.7}$$

where the subscripts $i = a, e$ designate the A_{1g} mode and E_g mode respectively. A_i, b_i, Ω_i and φ_i are the initial amplitude, decay rate, angular frequency and initial phase of the oscillations corresponding to phonon mode i. Fig. 4.7 is a summary of the temperature dependent behavior of initial amplitudes A_i in Sb and Bi. In Sb, the initial amplitude of A_{1g} is almost constant over the entire temperature range; the initial amplitude of E_g decreases from 2.9×10^{-5} at 10K to 1.2×10^{-5} at 292K. In Bi, the initial amplitude of A_{1g} is constant except for at very low temperatures; for E_g, similar to the case of Sb, a decrease is observed from 2.6×10^{-5} at 10K to 6.2×10^{-6} at 292K.

The results from the Stokes RS experiment for Sb and Bi at room temperature are shown in Fig. 4.8. Two peaks are observed in each material, with the same frequencies as their counterparts in the pump-probe experiment. I fit the spectra with

$$\frac{d\sigma}{d\omega_S} = \sum_i S_i \frac{W_i / 2\pi}{(\omega - \Omega_i)^2 + (W_i / 2)^2} \tag{4.8}$$

where S_i is the area under peak i and W_i is the FWHM. The fit results are shown in Fig. 4.8. Note that a decaying exponential is used to fit the laser tail showing up in the spectrum of Bi.

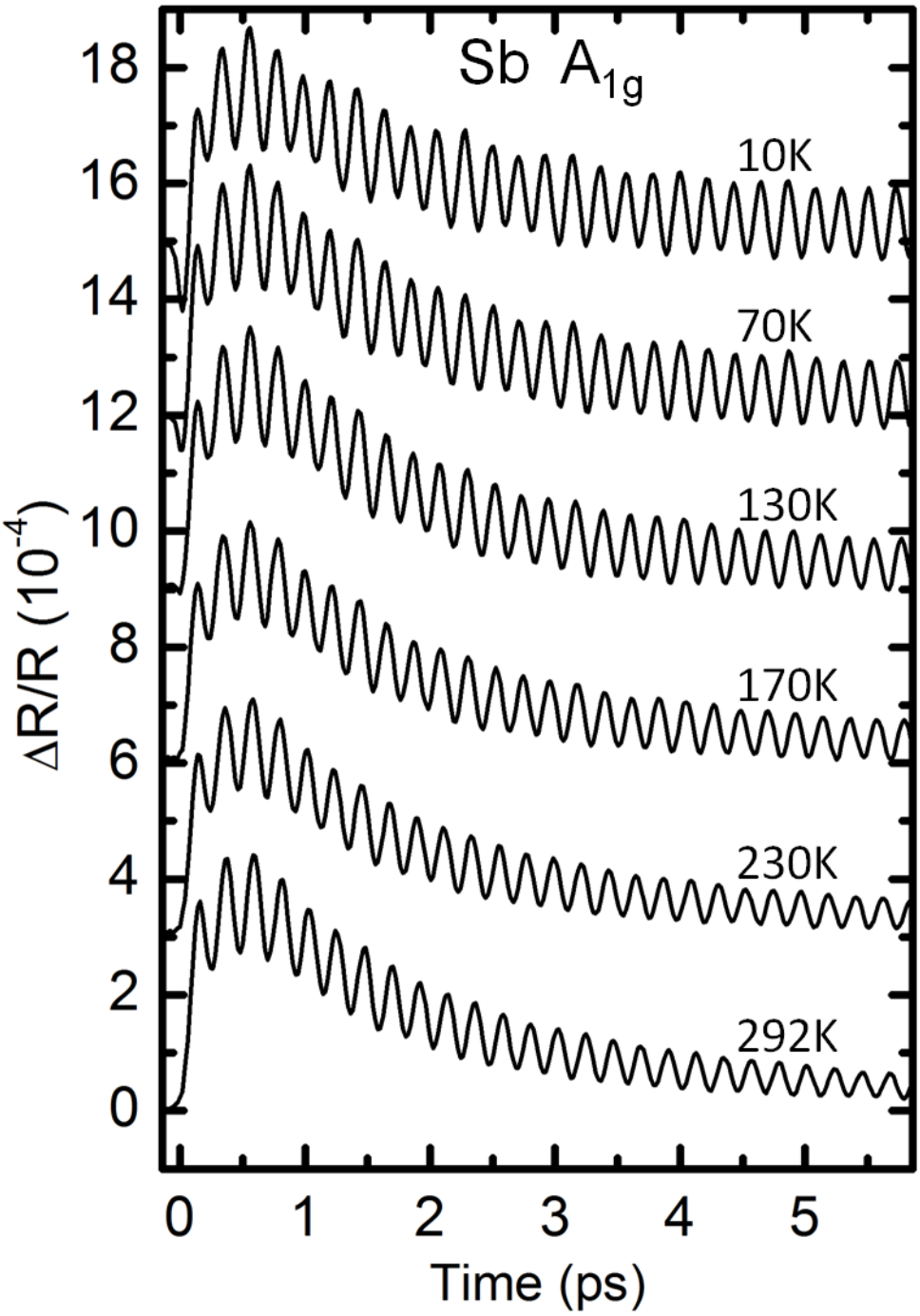

Figure 4.3. Differential reflectance data of the A_{1g} mode in Sb at different temperatures.

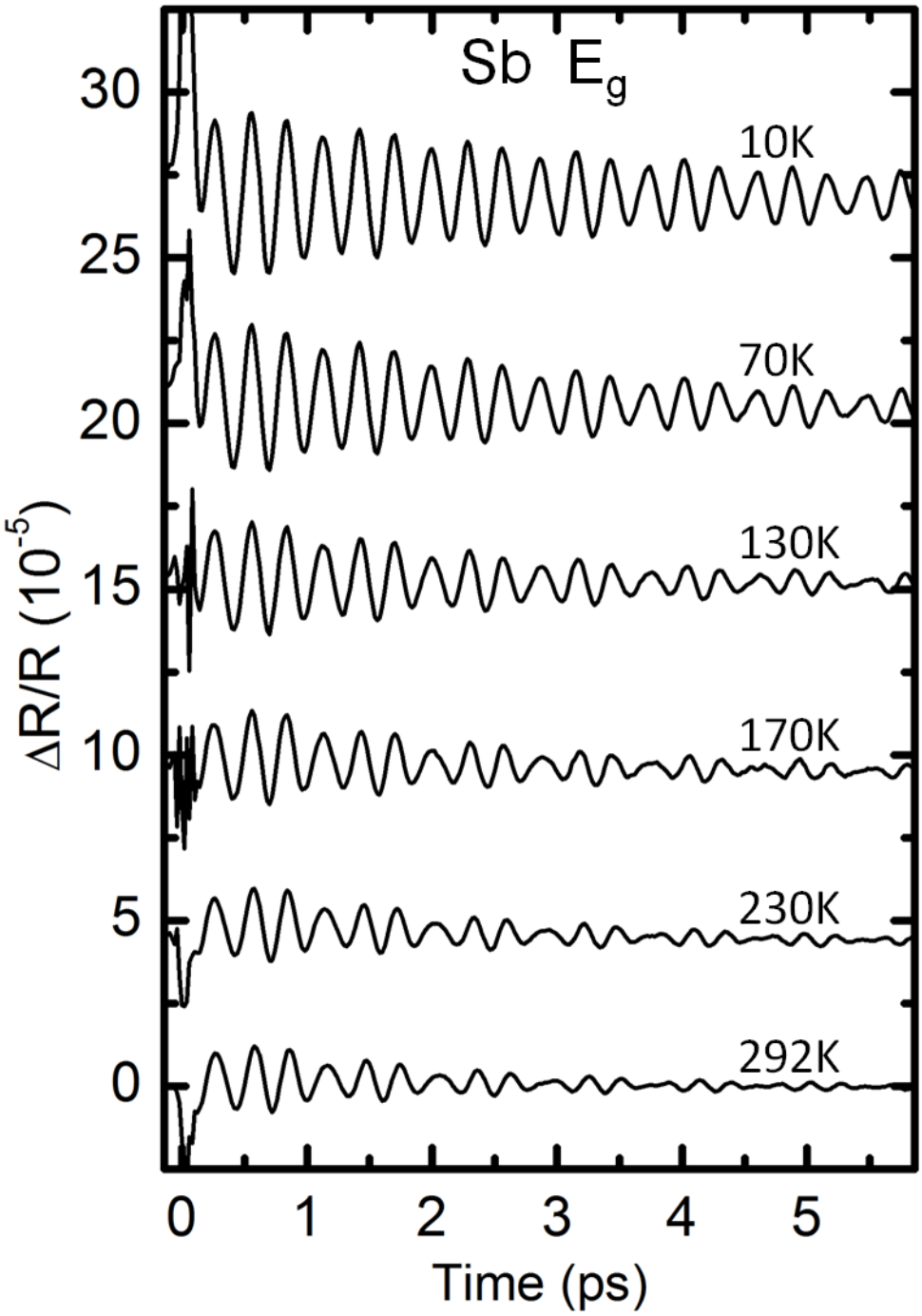

Figure 4.4. Differential reflectance data of the E_g mode in Sb at different temperatures. The feature at zero time delay is an artifact caused by the interference between the pump and the probe.

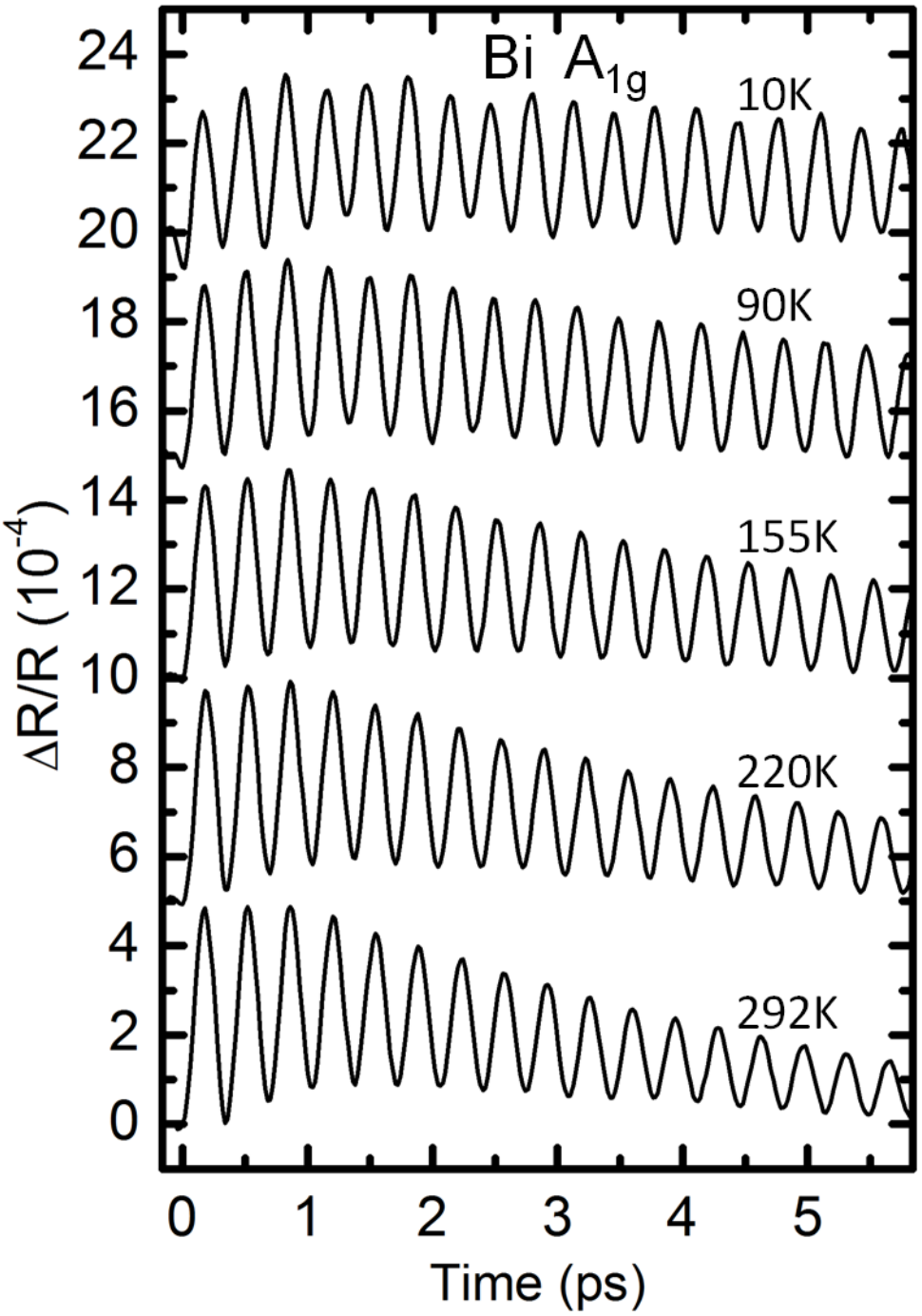

Figure 4.5. Differential reflectance data of the A_{1g} mode in Bi at different temperatures.

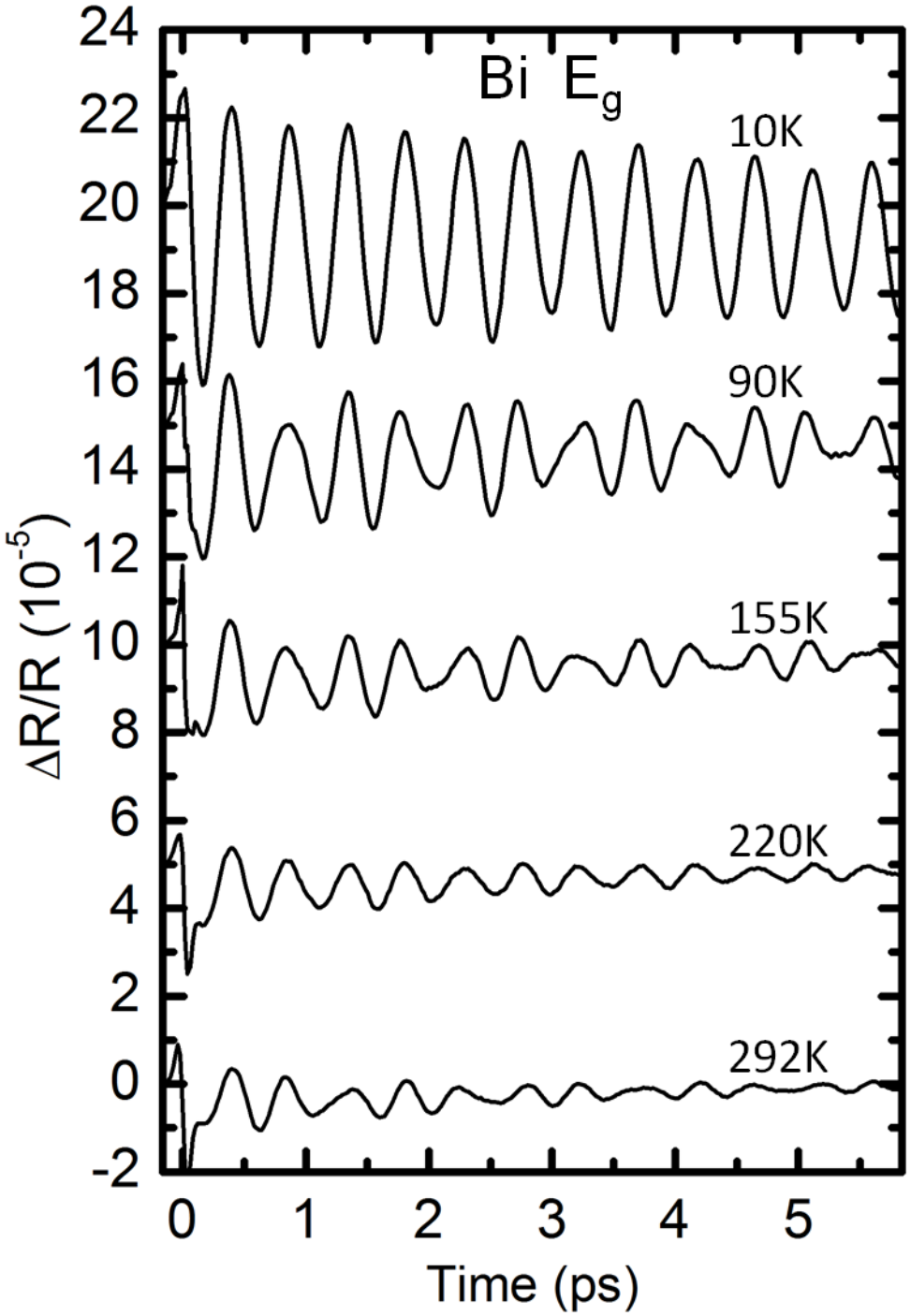

Figure 4.6. Differential reflectance data of the E_g mode in Bi at different temperatures.

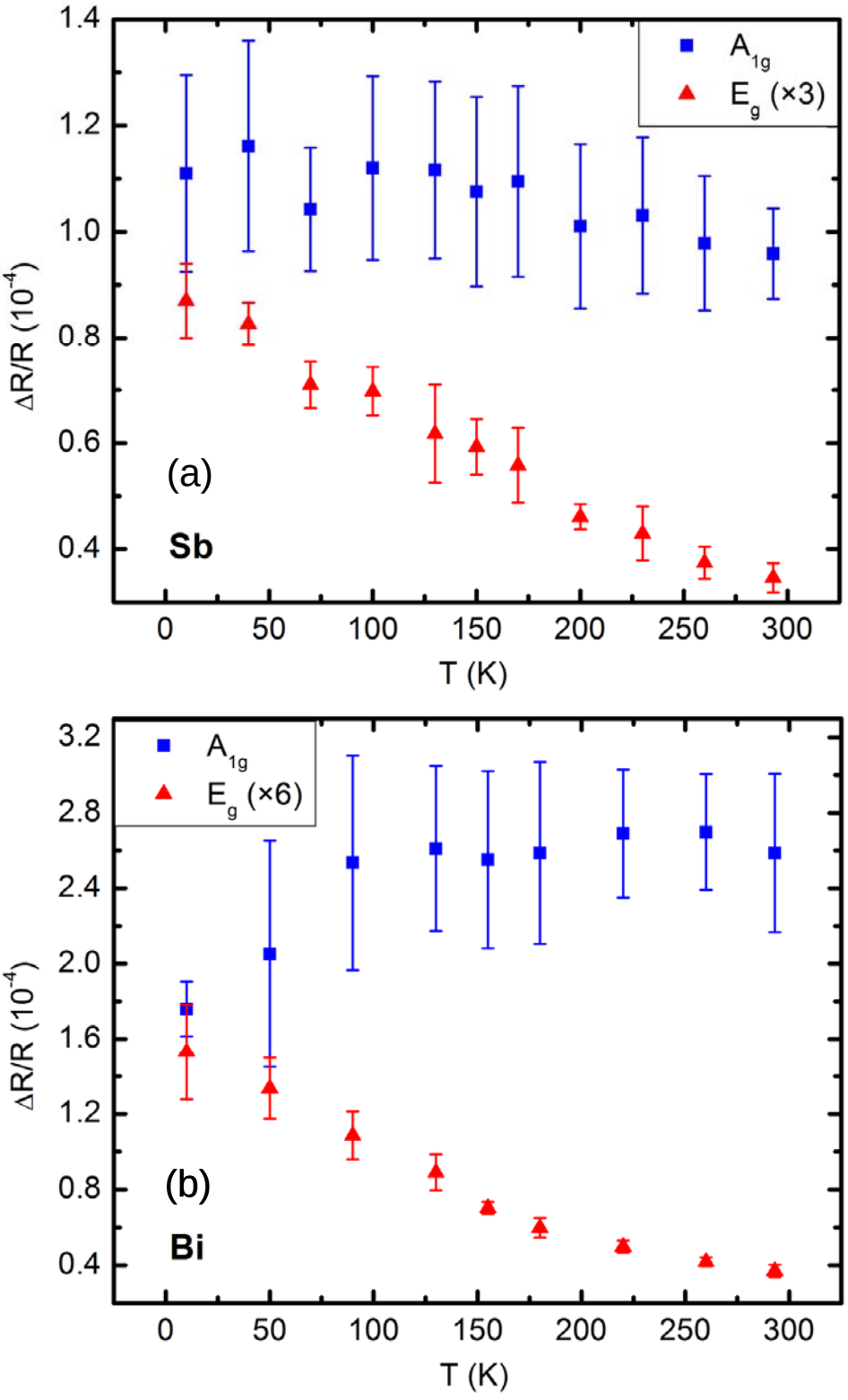

Figure 4.7. Temperature dependence of initial amplitudes of A_{1g} (blue square) and E_g (red triangle) modes in (a) Sb and (b) Bi.

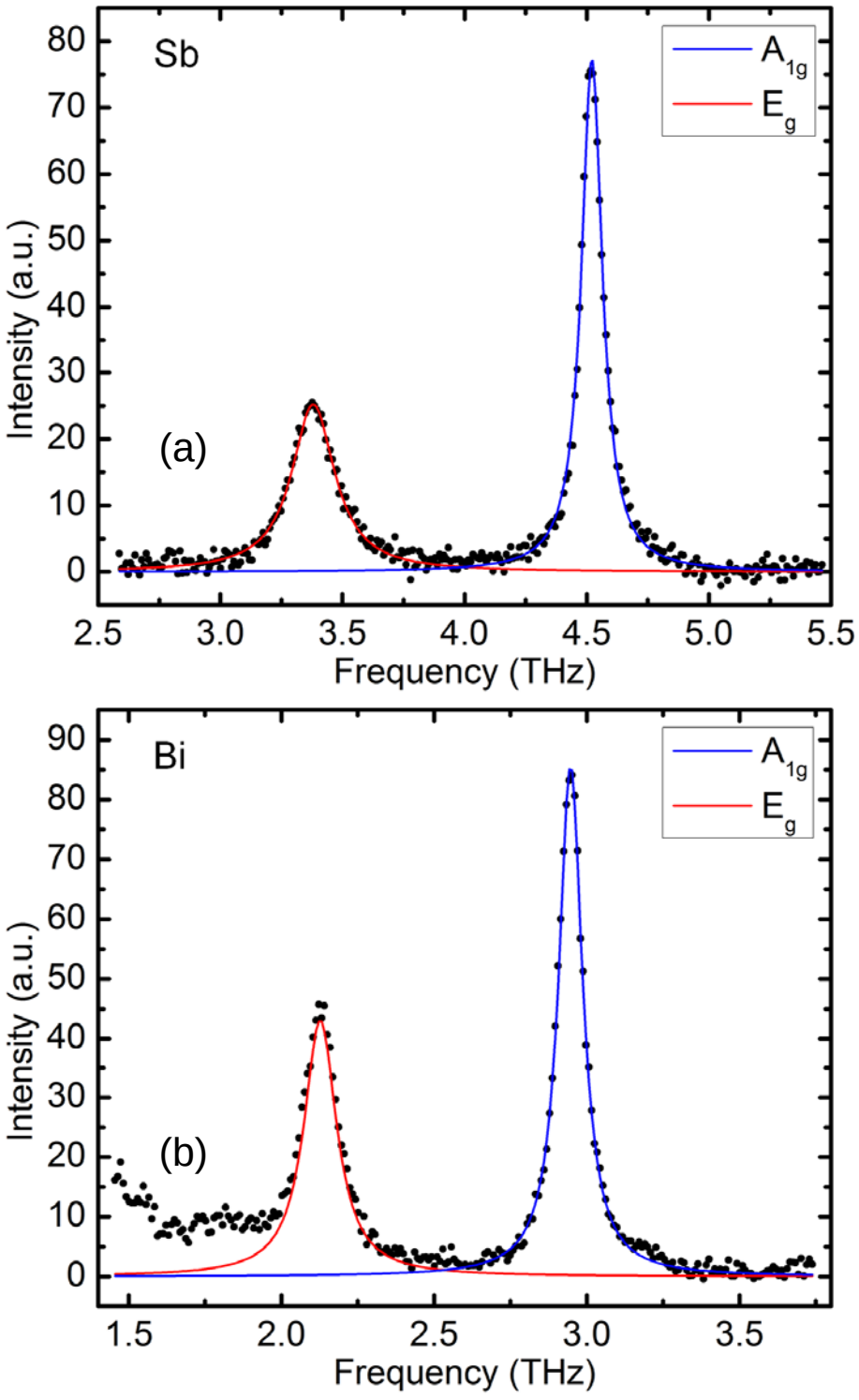

Figure 4.8. Raman spectra at room temperature in (a) Sb and (b) Bi. Dots are experimental data points. Blue and red lines are Lorentzian fits for the A_{1g} mode and the E_g mode respectively.

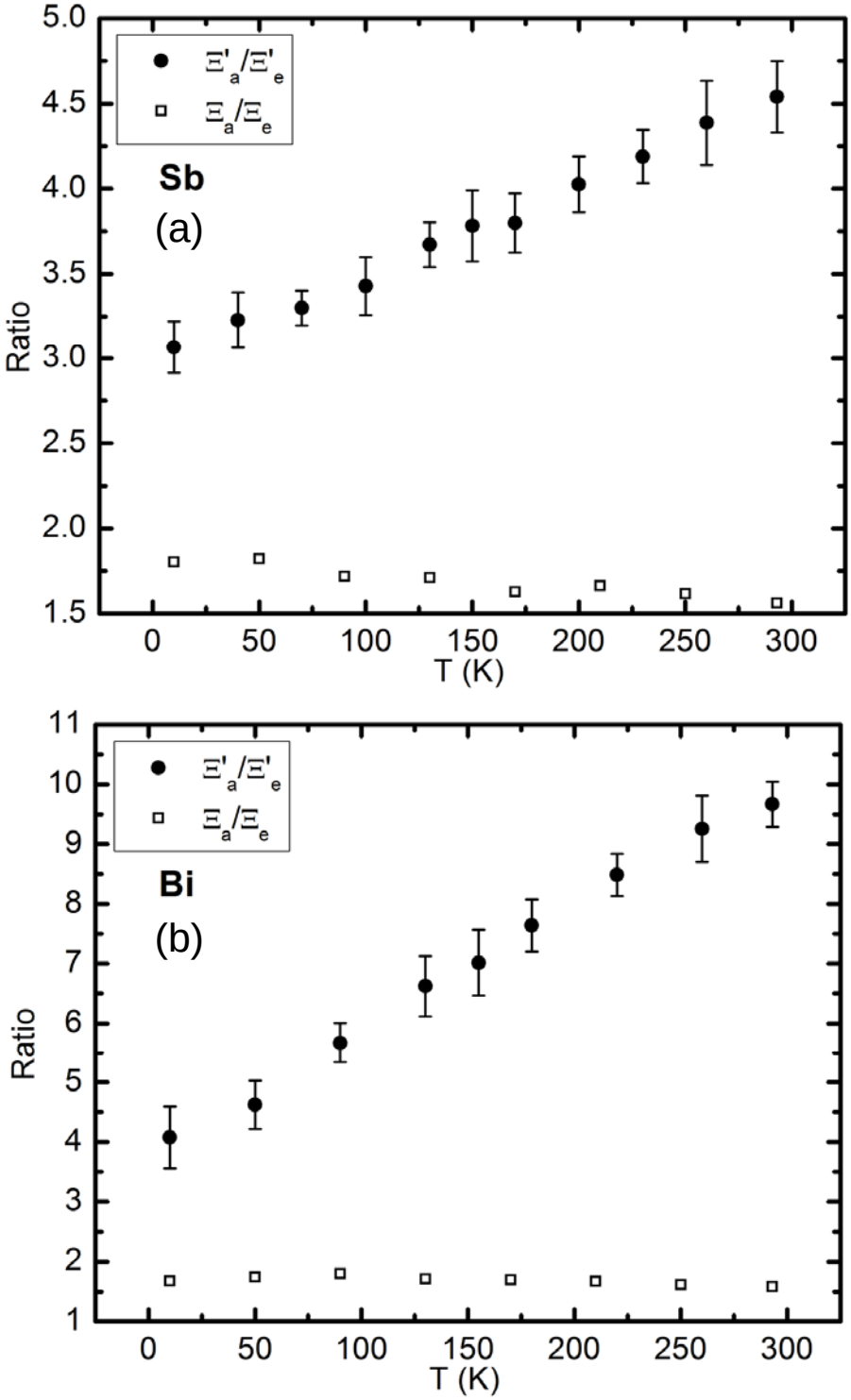

Figure 4.9. Temperature dependence of ratios between deformation potentials in (a) Sb and (b) Bi. Solid circles are ratios between deformation potentials from pump-probe experiments. Hollow squares are ratios from RS experiments.

4.6 Discussion of the temperature dependent experiments

The differential reflectance in pump-probe and scattering cross section in RS are related via the deformation potential. In order to correct for the temperature dependence of permittivity, ratios between deformation potentials of the two modes in the same material are extracted from both pump-probe and RS data.

With Eq. (2.30) and Eq. (2.66), the ratio between deformation potentials of mode i and mode j is

$$\frac{\Xi_i}{\Xi_j} = \left[\frac{S_i \Omega_i \left(n_j + 1 \right)}{S_j \Omega_j \left(n_i + 1 \right)} \right]^{1/2}$$

On the other hand, in a pump-probe experiment, by assuming the decay rate of the driving force $\Gamma \sim 0$ for all modes, with Eq. (2.71), Eq. (2.76), Eq. (2.65) and Eq. (2.66), I have

$$\frac{\Xi_i'}{\Xi_j'} = \left(\frac{A_i \Omega_i^2 e^{\Omega_i^2 \tau_0^2 / 2}}{A_j \Omega_j^2 e^{\Omega_j^2 \tau_0^2 / 2}} \right)^{1/2}$$

The primes designate results from a pump-probe experiment. Although this expression is obtained under the limit $\Gamma \sim 0$, it can be easily extended to cases that Γ is much smaller than Ω. Under this assumption, ratios from a Raman experiment and a pump-probe experiment should be the same.

Fig. 4.9 is a summary of the ratios between the A_{1g} and E_g modes in Sb and Bi. The Ξ_a' / Ξ_e' ratios in the pump-probe experiment have different values from the corresponding Ξ_a / Ξ_e ratios in RS, and they also exhibit different temperature-dependent behaviors. Ξ_a' / Ξ_e' in Sb shows strong temperature dependence, going from 3.1±0.2 at 10K to 4.5±0.2 at room temperature, while Ξ_a / Ξ_e in RS only has weak temperature-dependence, with its value staying in the range 1.6~1.8. Similar

behavior is also observed in Bi. Ξ'_a / Ξ'_e increases from 4.1±0.5 to 9.7±0.4 and Ξ_a / Ξ_e stays around 1.6~1.8.

The temperature dependence of the initial amplitude of each mode can be used to estimate the magnitude of the decay rate Γ of its driving force. As shown in Fig. 2.7, Q_0 manifests different sensitivities on Γ below and above Ω. Considering the weak temperature dependence of the A_{1g} amplitude in Sb and Bi in Fig. 4.7, Γ_a should be relatively smaller compared to Ω_a, so that the influence on the amplitude of the A_{1g} mode is insignificant when Γ_a changes with temperature. This confirms our assumption that the decay rate of the driving force for the A_{1g} modes is very small. On the other hand, the strong temperature dependence of amplitudes of E_g mode in both materials indicates that Γ_e is comparable or larger than Ω_e. This means that the assumption $\Gamma \sim 0$ does not apply to the case of coherent E_g mode, which is the reason for the observed discrepancy between RS and pump-probe ratios in Fig. 4.9.

A_{1g} modes and E_g mode have different Γ's because they are coupled to forces of different symmetries. In a crystal, charge density of a specific symmetry only couples to lattice vibrations of the same symmetry. For a $\mathbf{k}$ point without special symmetry in the Brillouin zone of Sb and Bi, there are 11 other equivalent points, as shown in Fig. 4.1 (b). For simplicity, Fig. 4.10 shows only three equivalent $\mathbf{k}$ points with trigonal symmetry, and situations in other equivalent $\mathbf{k}$ points can be easy inferred by applying the mirror symmetry operation and inversion symmetry operation to the case in Fig. 4.10. As shown in Fig. 4.10 (a), when carriers are initially excited by the pump pulse, electronic transitions around $\mathbf{k}$ points parallel to the electric field are favored owing to a larger dipole transition element compared to other $\mathbf{k}$ points. This anisotropic distribution of carriers in $\mathbf{k}$ space, which breaks the trigonal symmetry of the crystal, is the origin of the force of E_g symmetry, a process similar to the previously reported generation

mechanism for the T_{2g} mode in Si and Ge [20,27]. The driving force of A_{1g} symmetry is also present since it only depends on the total number of photoexcited carriers which shifts the equilibrium position of the ions. When elastic or quasi-elastic scattering quickly redistributes carriers within the equivalent **k** points, all three **k** points are equally populated and the trigonal symmetry of the crystal is restored such that the E_g force no longer exists, as shown in Fig. 4.10 (b). This redistributive process happens in a very short time scale and is temperature dependent. It is possibly caused by scattering with large wavevector thermal phonons, since at higher temperatures, the population of thermal phonons increases and thus raises the electron-phonon scattering rate. After the redistribution process, the carrier density in **k** space becomes isotropic, and the driving force of A_{1g} symmetry still lasts; lifetime of the A_{1g} force depends on the rate of electron-hole recombination. Fig. 4.11 illustrates the symmetry of the charge distribution for the corresponding scenarios in real space around the center of inversion symmetry of a unit cell. The blue cloud is for negative charge density while the red cloud is for positive charge density. As shown in 4.11 (a), the top ion is pushed/pulled to the right by the positive/negative charges while the bottom ion experiences a force in the opposite direction. This characterizes the motion of one of the E_g modes. After the trigonal symmetry is restored, as shown in 4.11 (b), there is no preference for the ions to move in either directions in the plane perpendicular to the trigonal axis. The only motion available is to move along the trigonal axis.

Based on the argument above, I can estimate the decay rates of charge densities of E_g symmetry. I make an approximate Γ_a~0.1/ps, which is close to the timescale of relaxation of the electronic background in the A_{1g} signal. Fig. 4.12 shows the temperature dependent lifetimes $1/\Gamma_e$ of charge densities with E_g symmetry. The lifetime decreases from 15±2fs at 10K to 6±1fs at room temperature in Sb and from 14±3fs to 2.2±0.2fs in Bi. All these time scales are much shorter than the 70fs pulsewidth I used. The reason that such a short time scale can be resolved with a relatively longer pulse is because I am

measuring amplitudes instead of time. When the pump pulse envelope passes through the sample, the driving force from charge density with E_g symmetry decays so fast that a strong coherent force fails to build up, hence rendering a weaker phonon signal.

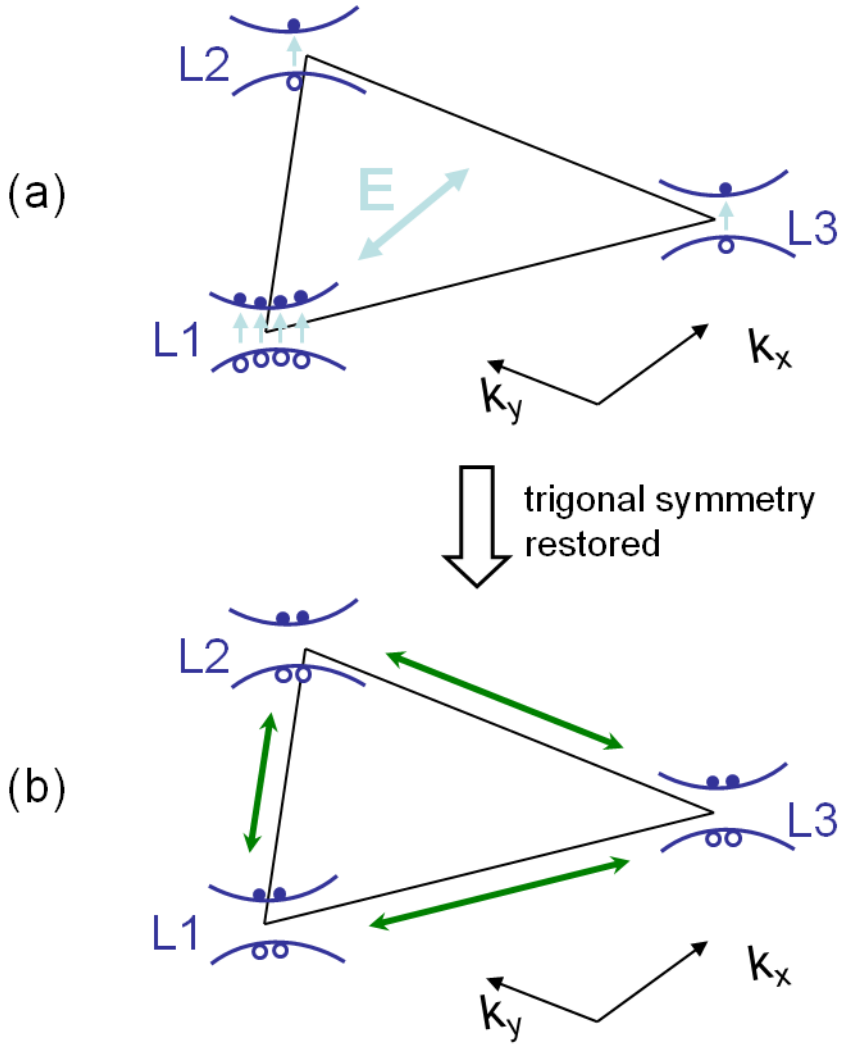

Figure 4.10. Carrier density distributions in three equivalent points L1, L2 and L3 in the Brillouin zone of Sb or Bi after the excitation by an electric field polarized along k_x. (a) More carriers are excited at the L1 point, which is along the polarization of the electric field, compared to L2 and L3. The trigonal symmetry is broken. This starts the E_g driving force. (b) Elastic or quasi-elastic scattering (represented by the green bidirectional arrows) restores the trigonal symmetry of the crystal. Only the A_{1g} driving force is present.

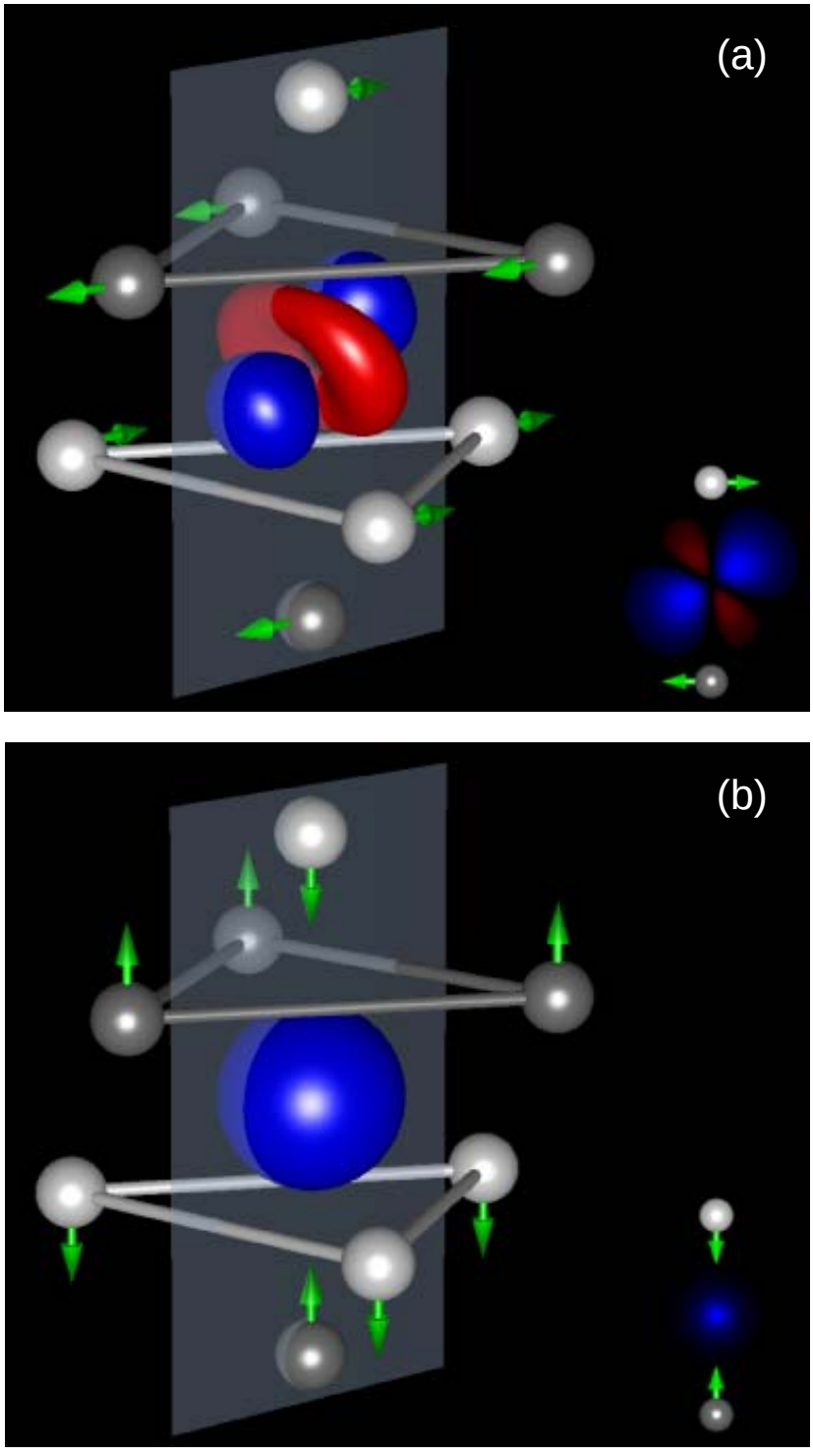

Figure 4.11. Schematic diagram of charge distribution in real space. (a) Charge density distribution of E_g symmetry. (b) Charge density distribution of A_{1g} symmetry. Blue cloud stands for negative charge and red cloud stands for positive charge. Note that the electron and hole clouds only illustrate the symmetry characteristic of the charge densities, not the absolute magnitude.

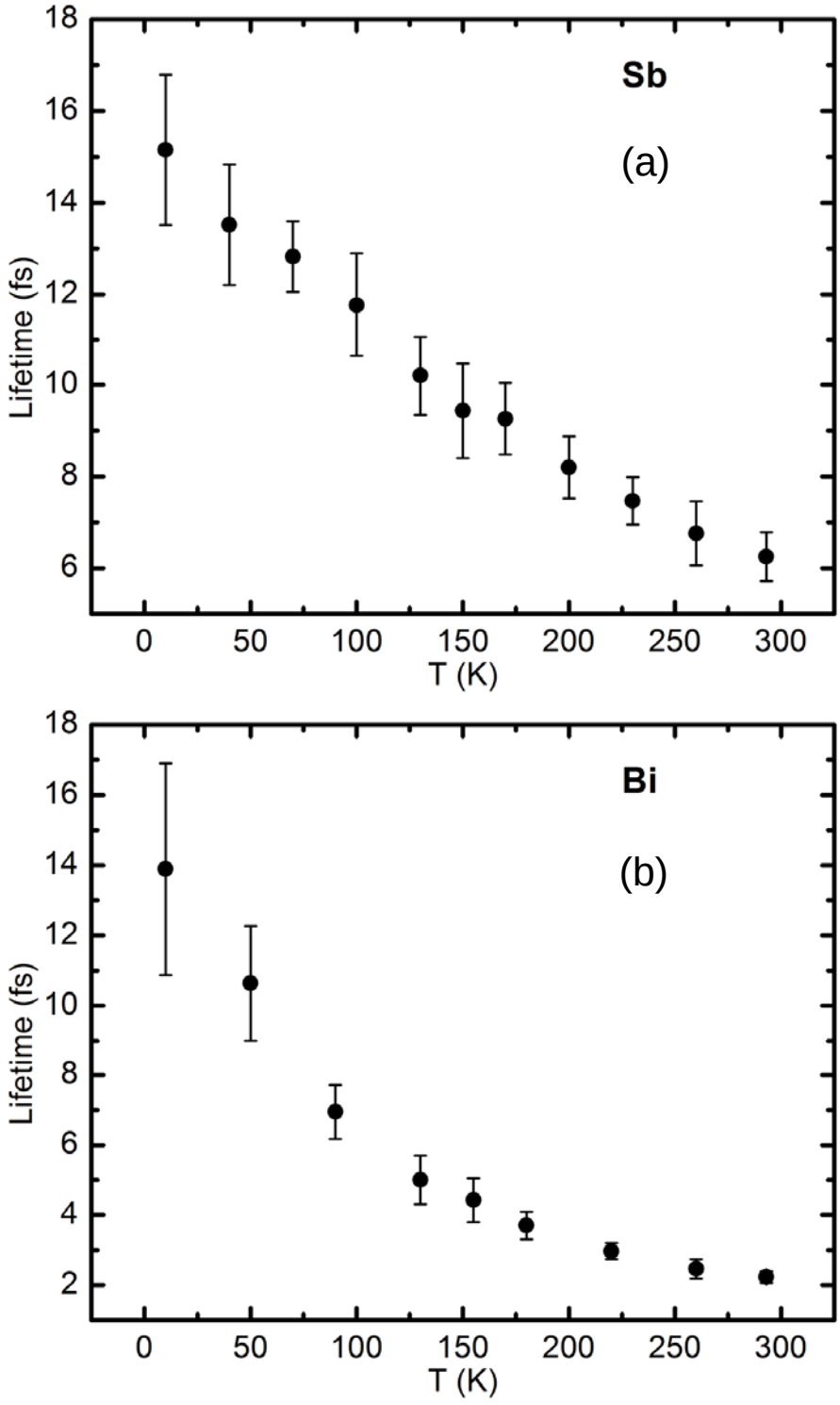

Figure 4.12. Lifetime of carrier density with E_g symmetry in (a) Sb and (b) Bi.

4.7 Fluence dependent experiments in Sb and chirped phonons

The fluence dependent behavior of the A_{1g} mode in Bi has been studied extensively. One of the features that arise at high fluence is the "chirped phonon", which means that the frequency of the phonon oscillations increases with time after the optical excitation. Fig. 4.13 is an example of the "chirped phonons". As is shown in the graph, a harmonic oscillator model fits the data for the first 1.5ps of the signal while it gradually goes out of phase with later oscillations.

Explanations mainly pertain to two aspects. One attributes the time dependent frequency to lattice anharmonicity induced by the high density excitation, stating that when the oscillation amplitude damps with time, the contribution to the frequency originating from the cubic terms in the higher order expansions of the lattice potential becomes less obvious, and hence the potential well restores to the range where harmonic approximation applies and the frequency returns to the natural frequency [21]. The other explanation emphasizes the softening by a diffusive plasma. The screening effect on the bonds between ions by the photoexcited plasma gradually dies out as the carriers on the surface layer diffuse into the bulk [23].

A set of fluence dependent experiments are carried out on Sb at room temperature for both A_{1g} and E_g modes. The conventional analytical tool, the linear prediction method which assumes a harmonic oscillator behavior, tends to give two slightly different frequencies to fit the varying frequency at high fluences, which is not physical. A new model is thus employed to fit the data. A high-pass electronic filter is used to extract the oscillatory part of the signal and then a model taking into account the "chirp" is used to fit the data [28]

$$\frac{\Delta R(t)}{R} = A\exp(-bt)\cos\left[2\pi t\left(f - \frac{2\tau_c}{\sqrt{t}}\right)\right] \tag{4.9}$$

where τ_c is a parameter that characterizes the diffusive rate of photoexcited carriers. The fit result is also shown in Fig. 4.13.

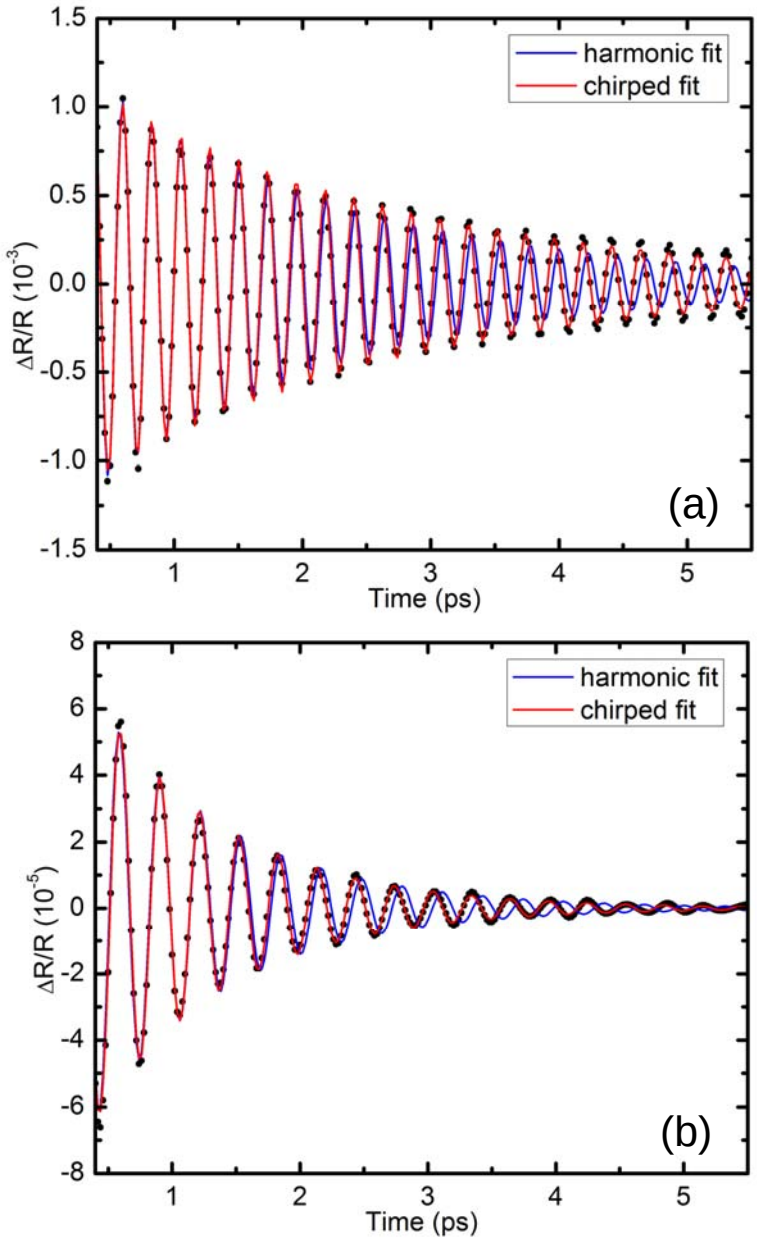

Figure 4.13. Phonon signals of (a) A_{1g} and (b) E_g signals in Sb at 0.17mJ/cm^2. The solid dots are experimental data. The blue curve is a fit with a single frequency harmonic oscillator model from 0.16ps to 1.5ps; the red curve is a fit with a chirped oscillator model. The background in the A_{1g} signal is removed by a high pass filter with a cutoff frequency 3THz; the background and A_{1g} residual oscillations in the E_g signal are removed by a high pass filter and a low pass filter with cutoff frequencies 2THz and 4THz respectively.

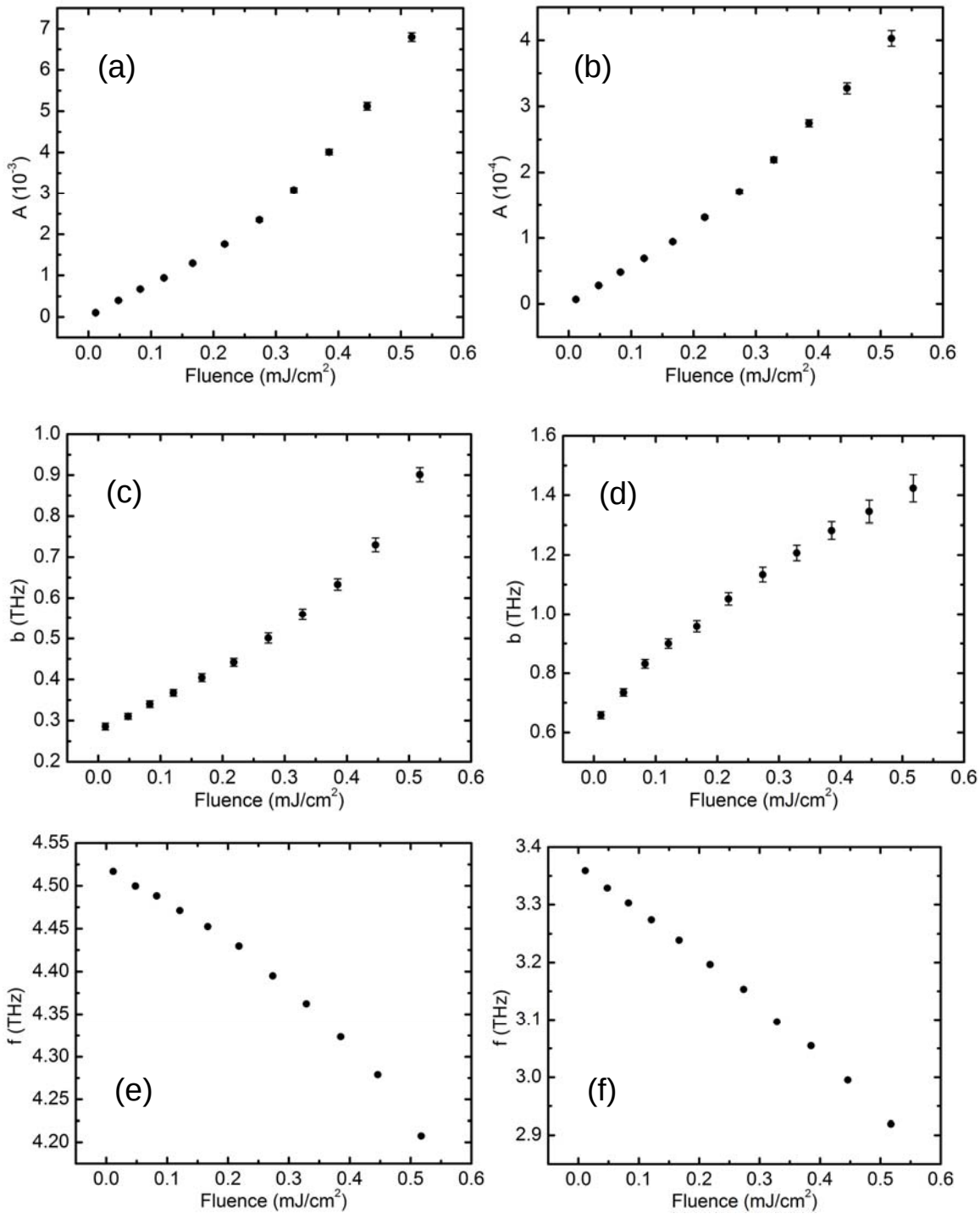
(a)
A (10^{-3})
Fluence (mJ/cm^2)
(b)
A (10^{-4})
Fluence (mJ/cm^2)
(c)
b (THz)
Fluence (mJ/cm^2)
(d)
b (THz)
Fluence (mJ/cm^2)
(e)
f (THz)
Fluence (mJ/cm^2)
(f)
f (THz)
Fluence (mJ/cm^2)

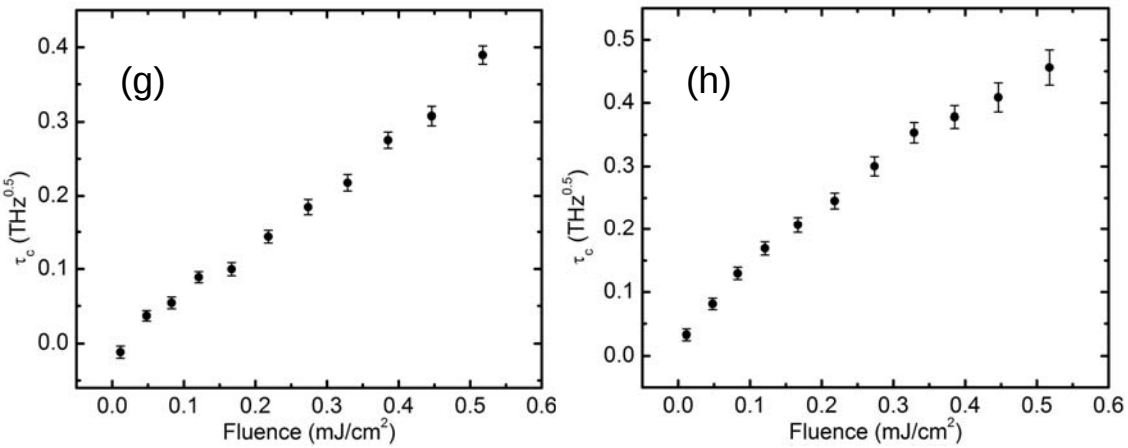

Figure 4.14. Fit results with Eq. (4.9) at different fluencies for A_{1g} (left column) and E_g (right column) modes in Sb. (a), (b) are the initial amplitudes; (c), (d) are the decay rates of the oscillation amplitude; (e), (f) are the frequencies given by linear prediction, which show the averaged frequencies within the 6ps time windows; (g), (h) are the constants characterizing the frequency chirp.

Fluence dependent parameters for both modes are summarized in Fig. 4.14. The initial amplitude, decay rate and chirp constant increase while the averaged frequency decreases with fluence for each mode. Above 0.25mJ/cm^2, the initial amplitudes of A_{1g} and E_g modes start to show nonlinearity with the increase of fluence. The screening effect represented by the second term of the time dependent frequency in Eq. (4.9) is influenced by the photoexcited carrier density, which changes with time as $\propto 1/\sqrt{t}$. Here I am assuming a 1-D diffusion into the bulk and the lateral diffusion is not considered because the spot size around 200μm is much larger than the penetration depth around 10nm. The chirp constant τ_c increases with fluence due to increased injection of photoexcited carriers, which enhances the screening effect. Another notable feature is the different curvatures of the decay rate curves for A_{1g} and E_g modes. Since the decay rate is related to the anharmonicity of the lattice, the laser beam might modify the potential wells of an ion anisotropically along the trigonal axis and in the plane perpendicular to the trigonal axis. The explanation needs further testing from first-principle theoretical calculations and more experimental works.

4.8 Summary

Coherent and incoherent phonons in Sb and Bi have been studied under different temperatures with ultrafast laser spectroscopy and Raman spectroscopy. The different temperature-dependent behaviors of A_{1g} and E_g coherent phonon modes reveal the ultra-short lifetime of the E_g symmetry of the photoexcited carrier density distribution. The experimental results add to the theories on coherent phonons in opaque materials in the aspect that the lifetime of the driving force also influences the amplitude of phonon oscillations.

Fluence dependent studies of the A_{1g} and E_g modes in Sb show how laser power modifies lattice properties. The high laser power softens the lattice vibration owing to the screening by a photoexcited plasma. It also causes nonlinear growth of the phonon amplitudes and increased lattice anharmonicity. Further investigations on different responses of A_{1g} and E_g at high fluences can provide more information about lattice-carrier interaction and lattice-radiation interaction of different symmetries in uniaxial crystals.

References

[1] *Raman Scattering in Materials Science*, edited by W. H. Weber and R. Merlin, Springer Series in Materials Science Vol. 42 (Springer, Berlin, 2000), and references therein.

[2] Y.-X. Yan, E. B. Gamble, Jr., and K. A. Nelson, Journal of Chemical Physics **83**, 5391 (1985).

[3] R. Merlin, Solid Sate Communications **102**, 207 (1997).

[4] W. A. Kütt, W. Albrecht, and H. Kurz, IEEE Journal of Quantum Electronics **28**, 2434 (1992).

[5] L. Dhar, J. A. Rogers, and K. A. Nelson, Chemical Reviews **94**, 157 (1994).

[6] H. J. Zeiger, J. Vidal, T. K. Cheng, E. P. Ippen, G. Dresselhaus, and M. S. Dresselhaus, Physical Review B **45**, 768 (1992).

[7] R. Scholz, T. Pfeifer, and H. Kurz, Physical Review B **47**, 16229 (1993).

[8] G. A. Garrett, T. F. Albrecht, J. F. Whitaker, and R. Merlin, Physical Review Letters **77**, 3661 (1996).

[9] A. V. Kuznetsov, and C. J. Stanton, Physical Review Letters **73**, 3243 (1994).

[10] T. E. Stevens, J. Kuhl, and R. Merlin, Physical Review B **65**, 144304 (2002).

[11] R. Scholz, and A. Stahl, Physica Status Solidi (b) **168**, 123 (1991).

[12] Y. Liu, A. Frenkel, G. A. Garrett, J. F. Whitaker, S. Fahy, C. Uher, and R. Merlin, Physical Review Letters **75**, 334 (1995).

[13] S. Ruhman, A. G. Joly, and K. A. Nelson, IEEE Journal of Quantum Electronics **24**, 460 (1988).

[14] T. Pfeifer, T. Dekorsy, W. Kütt, and H. Kurz, Applied Physics A **55**, 482 (1992).

[15] A. V. Kuznetsov, and C. J. Stanton, Physical Review B **51**, 7555 (1995).

[16] T. K. Cheng, S. D. Brorson, A. S. Kazeroonian, J. S. Moodera, G. Dresselhaus, M. S. dresselhaus, and E. P. Ippen, Applied Physics Letters **57**, 1004 (1990).

[17] T. K. Cheng, J. Vidal, H. J. Zeiger, G. Dresselhaus, M. S. Dresselhaus, and E. P. Ippen, Applied Physics Letters **59**, 1923 (1991).

[18] M. Hase, K. Mizoguchi, H. Harima, S. Nakashima, M. Tani, K. Sakai, and M. Hangyo, Applied Physics Letters **69**, 2474 (1996).

[19] D. Boschetto, E. G. Gamaly, A. V. Rode, B. Luther-Davies, D. Glijer, T. Garl, O. Albert, A. Rousse and J. Etchepare, Physical Review Letters **100**, 027404 (2008).

[20] D. M. Riffe, and A. J. Sabbah, Physical Review B **76**, 085207 (2007).

[21] M. Hase, M. Kitajima, S. Nakashima and K. Mizoguchi, Physical Review Letters **88**, 067401 (2002).

[22] A. Q. Wu and X. Xu, Applied surface science **253**, 6301 (2007).

[23] S. Fahy and D. A. Reis, Physical Review Letters **93**, 109701 (2004).

[24] É. D. Murray, D. M. Fritz, J. K. Wahlstrand, S. Fahy and D. A. Reis, Physical Review B **72**, 060301 (2005).

[25] R. I. Sharp and E. Warming, Jouranl of Physics F **1**, 570 (1971).

[26] J. B. Renucci, W. Richter, M. Cardona and E. Schönherr, Physica Status Solidi (b) **60**, 299 (1973).

[27] T. Pfeifer, W. Kütt, H. Kurz, and R. Scholz, Physical Review Letters **69**, 3248 (1992).

[28] D. M. Fritz, Ph.D. thesis, University of Michigan, 2006.

CHAPTER 5

Optical Phonons in Bi_2Te_3, Bi_2Se_3 and Fabrication of Thin Film Bi_2Te_3

Bi_2Te_3 and its selenide alloys have been well known since the 1950's for their outstanding thermal properties with a large thermoelectric figure of merit and have been widely used in the thermoelectric industry [1-5]. In the meanwhile, the characteristics of chemical bondings and lattice dynamics in these crystals were studied intensively due to their highly anisotropic electronic and other interesting properties, as well as their role as model systems of layered semiconductors [6-12]. In recent years, these materials are gaining increasing interest again due to their special properties as three dimensional topological insulators. Although being narrow-gap semiconductors in the bulk [13], it was proposed that the interface between these materials and the air is metallic and is protected from time-reversal-invariant perturbations such as backscattering by disorders [14,15]. Subsequent angle-resolved photoemission spectroscopy (ARPES) experiments measured the surface electronic energy bands in Bi_2Te_3 and Bi_2Se_3, and confirmed the prediction of the theory [16-18]. An example of the surface electronic band of Bi_2Te_3 is shown in Fig. 5.1 (a). The V-shaped band pair is the dispersion curve of surface states, and it is nearly isotropic in the momentum plane, forming a Dirac cone in the energy-k_x-k_y space [17], as shown in Fig. 5.1 (b). Also, the spin of the surface state is in the surface plane and always perpendicular to k, usually referred to as spin-momentum locking [18,19]. In addition to ARPES, other techniques have been used to investigate the special properties of bulk topological insulators. Reflection second harmonic generation

(SHG) from the surface of a Bi_2Se_3 crystal has been detected with ultrafast lasers [20]. Utilizing the SHG, time-resolved pump-probe experiments were carried out to study photoinduced charge and spin dynamics of the surface state with a linearly and a circularly polarized pump respectively [21]. A recent coherent helium beam surface scattering experiment revealed a Kohn anomaly in the surface phonon dispersion curve of Bi_2Se_3, which is a signature of metallic states [22]. Corresponding theoretical calculation of the surface phonon dispersion curves predicts the possibility of observing surface phonons with a different frequency from the bulk ones in Bi_2Se_3 [22].

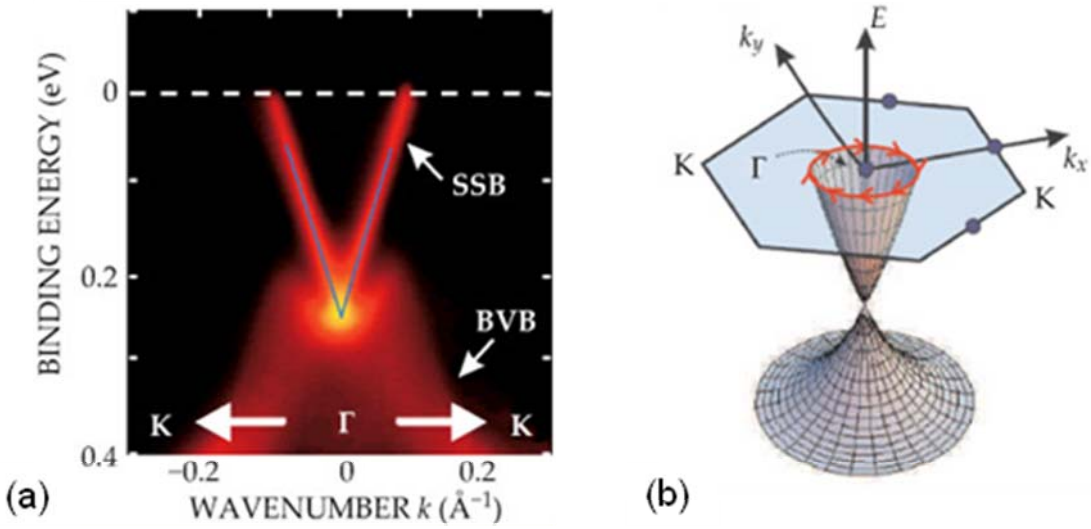

Figure 5.1. (a) The ARPES plot of electronic band dispersion in Bi_2Te_3 along the 2D $\bar{\Gamma}-\bar{K}$ direction shows a linearly dispersing surface-state band (SSB) above the bulk valence band (BVB). The dashed white line stands for the Fermi level [16,19]. (b) The Dirac cone of the surface state and spin-momentum locking in Bi_2Se_3 [18,19].

At the same time of the intensive study of bulk topological insulators, effort has also been invested in fabricating 2D ultrathin films of Bi_2Te_3 and Bi_2Se_3 [23-28]. Since the concept of a metallic surface originates from the interface between a normal insulator such as air and a topological insulator [19], it is intriguing to reduce the thickness of a topological insulator crystal to the limit of a few atomic layers when the distinction between bulk and surface is no longer well defined. A small thickness-dependent gap has

been observed to open up below 6 quintuple layers due to modes on opposite surfaces of Bi_2Se_3 coupled by quantum tunneling [29]. That thickness is characteristic of the crossover of the 3D topological insulator to the 2D limit. Micro-Raman experiments on Bi_2Te_3 films with only a few quintuple layers discovered an additional mode due to the breaking of symmetry and the intensity ratio of the additional mode to the bulk E_g mode increases with decreasing film thickness [26].

Sections 5.1-5.5 focus on temperature dependent behavior of incoherent and coherent phonons in Bi_2Te_3 and Bi_2Se_3. The main purpose of this study is to investigate the two A_{1g} modes in Bi_2Te_3 and Bi_2Se_3 to test if they behave similarly since these two modes are of the same symmetry. Comparisons between the A_{1g} and E_g modes are also made as in Chap. 4 to check if similar phenomena exist in Bi_2Te_3 and Bi_2Se_3. Sections 5.6-5.8 provide a brief summary of some preliminary work in fabricating and characterizing thin film Bi_2Te_3 with mechanical exfoliation, optical microscope and Raman spectroscopy. A summary is given in Section 5.9.

5.1 Crystal structure of Bi_2Te_3 and Bi_2Se_3

Bi_2Te_3 and Bi_2Se_3 have rhombohedral crystal structures with space group $R\bar{3}m$ [30]. The crystal is composed of quintuple layers stacked along the trigonal axis. Each quintuple layer has five atomic planes in the sequence $A_{VI}^{(1)}$-Bi-$A_{VI}^{(2)}$-Bi-$A_{VI}^{(1)}$, where A_{VI} stands for Te (or Se), and the superscripts distinguish the two different positions of Te (or Se) atoms in a quintuple layer. The weak bonding between adjacent quintuple layers is of van der Waals nature, which makes the cleavage between neighbouring quintuple layers easy, while the bondings between atomic planes inside a quintuple layer are covalent or ionic [6,8,9]. Fig. 5.2 shows the crystal structure of Bi_2Se_3.

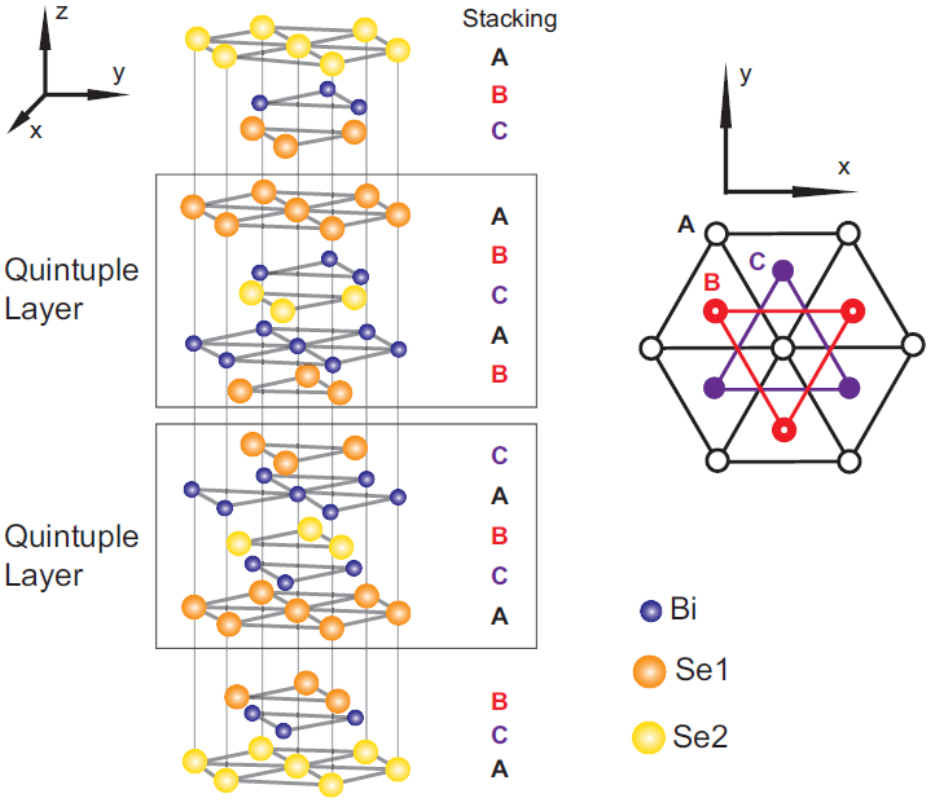

Figure 5.2. Crystal structure of Bi_2Se_3 [22]. The left graph shows quintuple layers stacked along the c axis. There are five fundamental atomic planes in each quintuple layer, among which there are two different positions for a Se atomic plane, represented by Se1 and Se2. The right graph is the top view of the stacking scheme of different planes A, B and C.

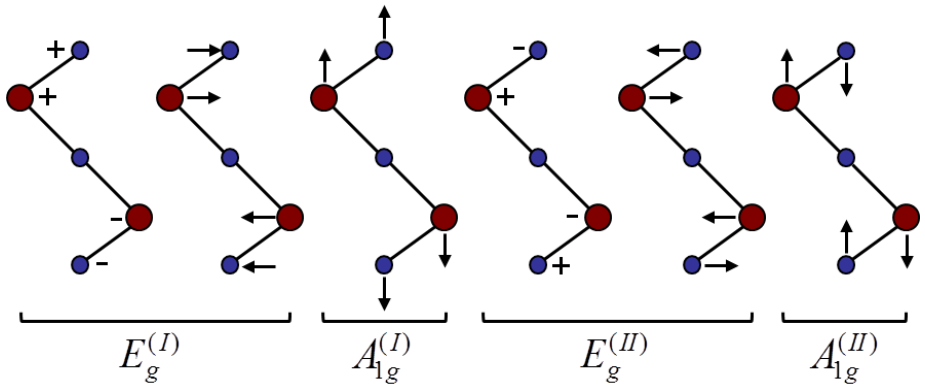

Figure 5.3. Raman-active modes of Bi_2Te_3 and Bi_2Se_3. The two A_{1g} modes are non-degenerate and the two E_g modes are doubly degenerate.

5.2 Phonons in Bi_2Te_3 and Bi_2Se_3

Each primitive cell has five atoms, which gives twelve optic phonon modes at q=0. Among them, there are six Raman active modes: two non-degenerate A_{1g} modes and two doubly degenerate E_g modes [30]. The scheme for the movement of ions in a unit cell for each mode is shown in Fig. 5.3. The lower frequency $A_{1g}^{(I)}$ and higher frequency $A_{1g}^{(II)}$ modes both correspond to ions moving along the c axis, while the lower frequency $E_g^{(I)}$ and higher frequency $E_g^{(II)}$ modes both correspond to ions moving in the plane perpendicular to the c axis. All the modes have inversion symmetry. Raman tensors for modes with A_{1g} and E_g symmetries are the same as those listed in Table 4.1.

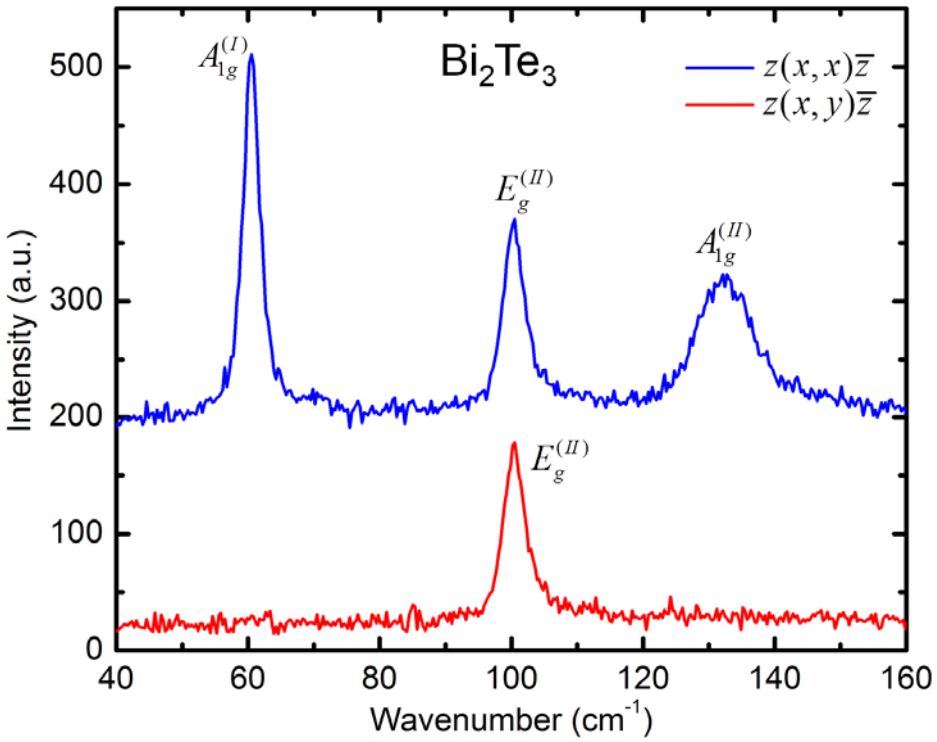

Figure 5.4. Raman signals of Bi_2Te_3 at room temperature follow selection rules.

5.3 Samples and experimental setups

Single crystal bulk Bi_2Te_3 and Bi_2Se_3 samples were grown using the Bridgman technique. They were then mounted in a flow helium cryostat with cleaved surfaces

perpendicular to the trigonal axis. Mechanical exfoliation was performed with an adhesive tape to obtain surfaces with good optical quality. The Raman selection rule was tested and is shown in Fig. 5.4, implying nice crystalline surfaces.

The setups for the pump-probe experiment and the RS experiment are similar to the one used in Chap. 4. In the pump-probe experiment, a 1.5mW pump and a 0.5mW probe were focused to spots with diameters of 90μm and 45μm respectively, spatially overlapped on the sample. The modulation frequency of the optical chopper in the pump path is 2kHz. In the RS experiment, I used a 15mW vertically polarized incident beam and backscattering $z(x,x)\bar{z}$ geometry.

5.4 Temperature dependent experimental data

Temperature dependent differential reflectance signals from the pump-probe experiment for the two A_{1g} modes and the high frequency E_g mode in Bi_2Te_3 and Bi_2Se_3 at different temperatures are shown in Fig. 5.5-5.8. Both A_{1g} modes $A_{1g}^{(I)}$, $A_{1g}^{(II)}$ and only the high frequency $E_g^{(II)}$ mode are observed, a result consistent with previous Raman and pump-probe data [30,31]. In Fig. 5.5 and Fig. 5.7, obvious beatings can be observed demonstrating the coexistence of the two modes with A_{1g} symmetry, while the relatively weaker E_g mode is hard to identify. In Fig. 5.6 and Fig. 5.8, the strong isotropic electronic background and large A_{1g} oscillations in each detection channel are cancelled by the other channel, and twice the reflectance change induced by the E_g mode is collected as a consequence of the specific detection scheme and selection rules.

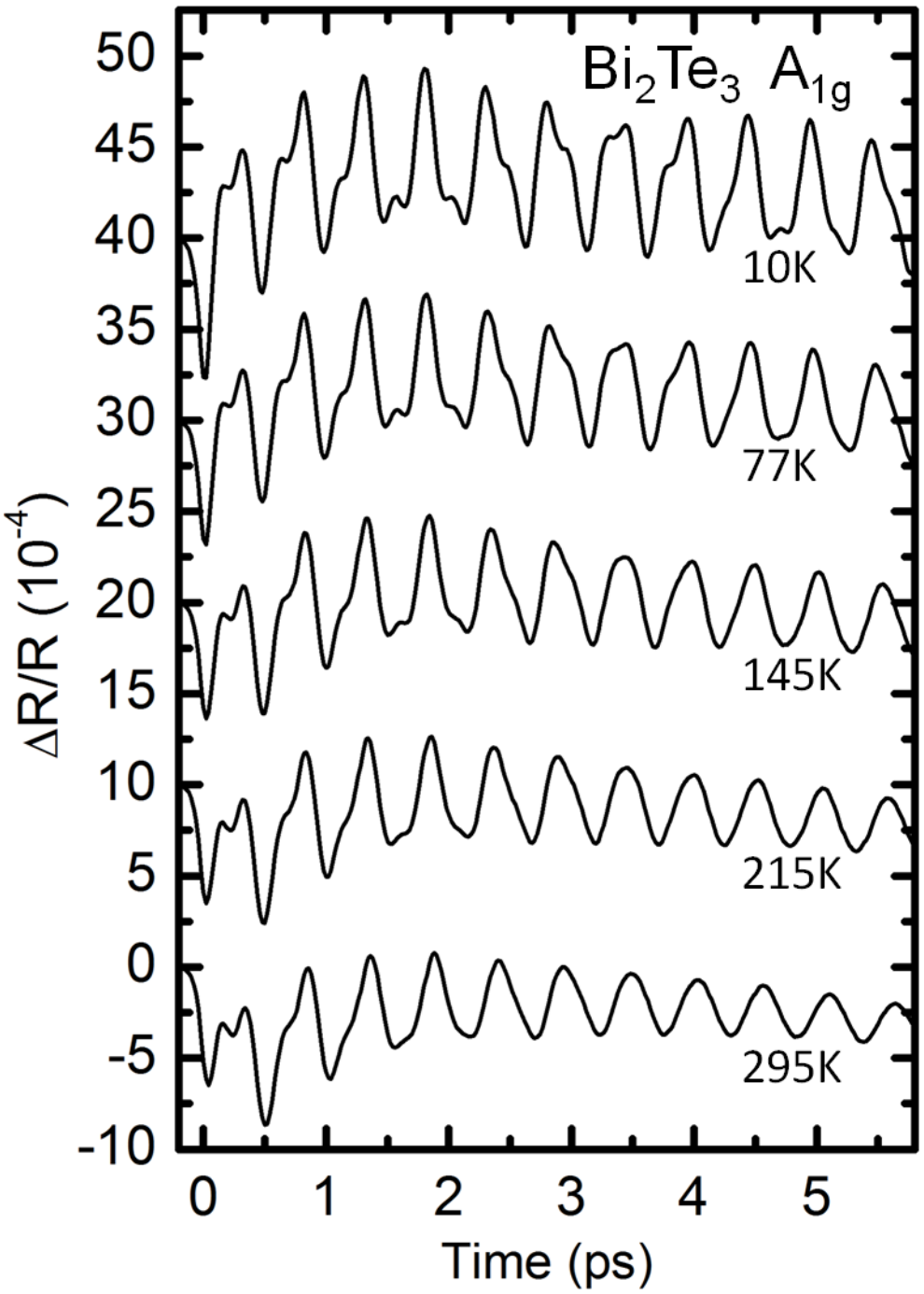

Figure 5.5. Differential reflectance data of the A_{1g} modes in Bi_2Te_3 at different temperatures.

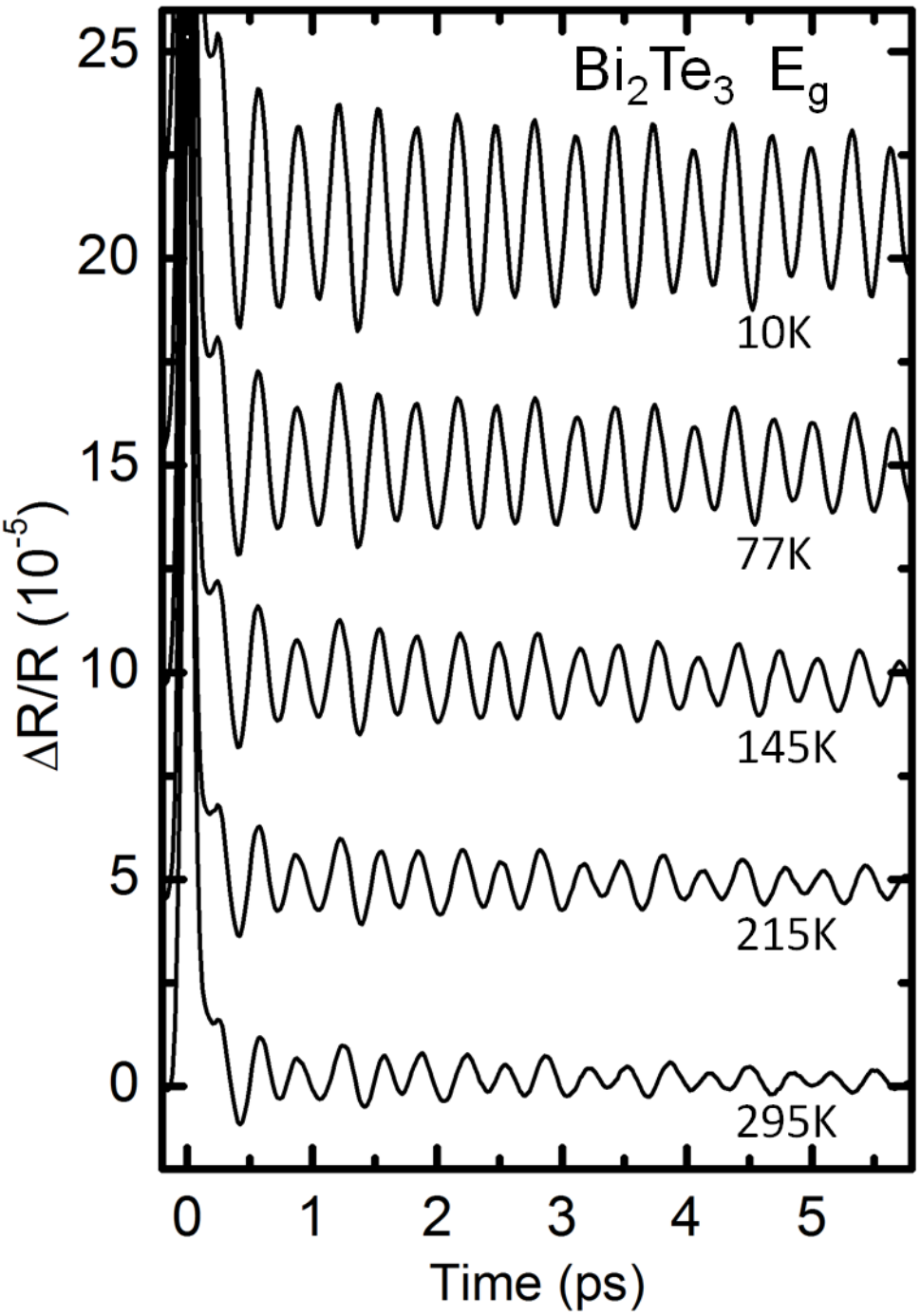

Figure 5.6. Differential reflectance data of the E_g mode in Bi_2Te_3 at different temperatures.

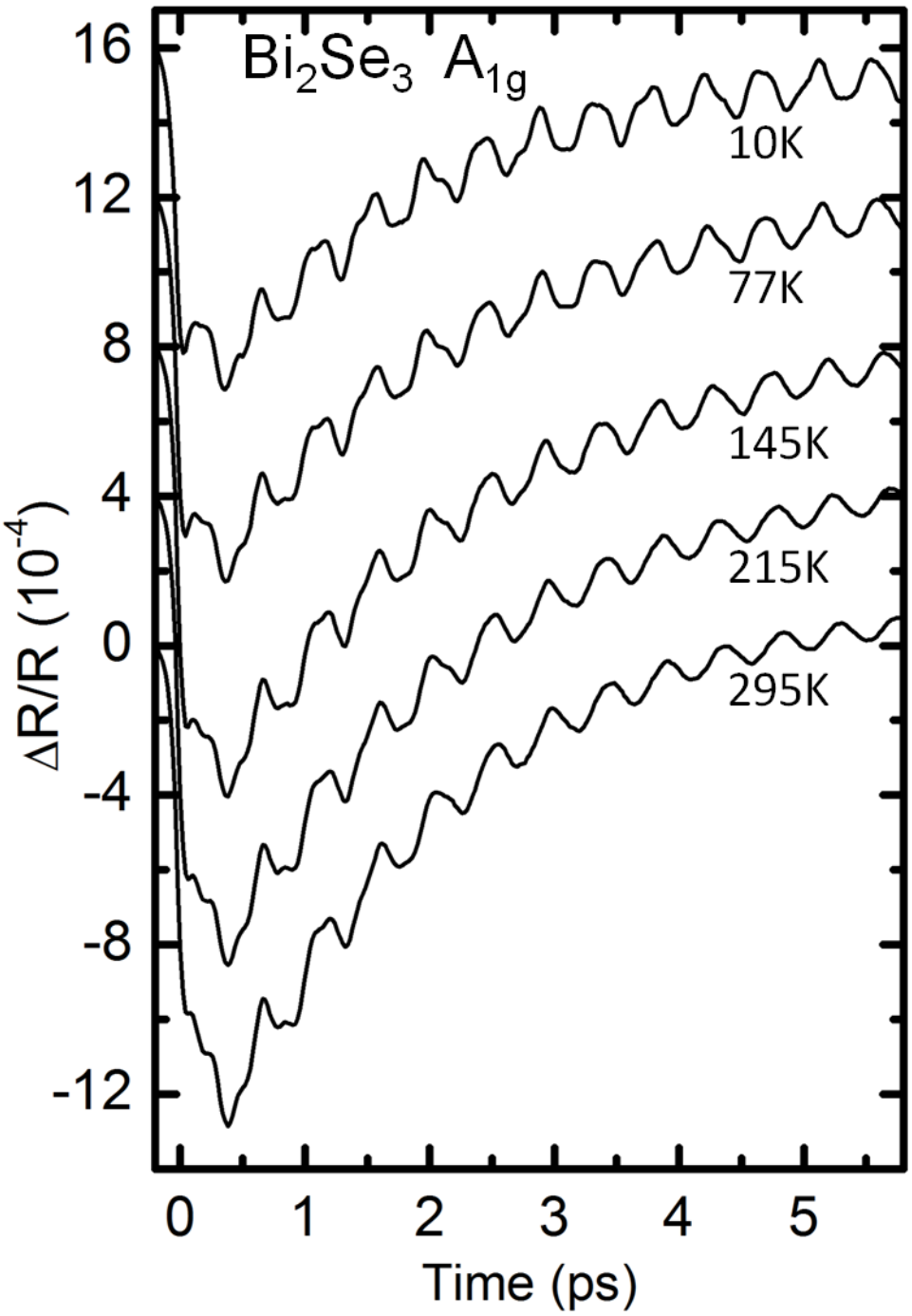

Figure 5.7. Differential reflectance data of the A_{1g} modes in Bi_2Se_3 at different temperatures.

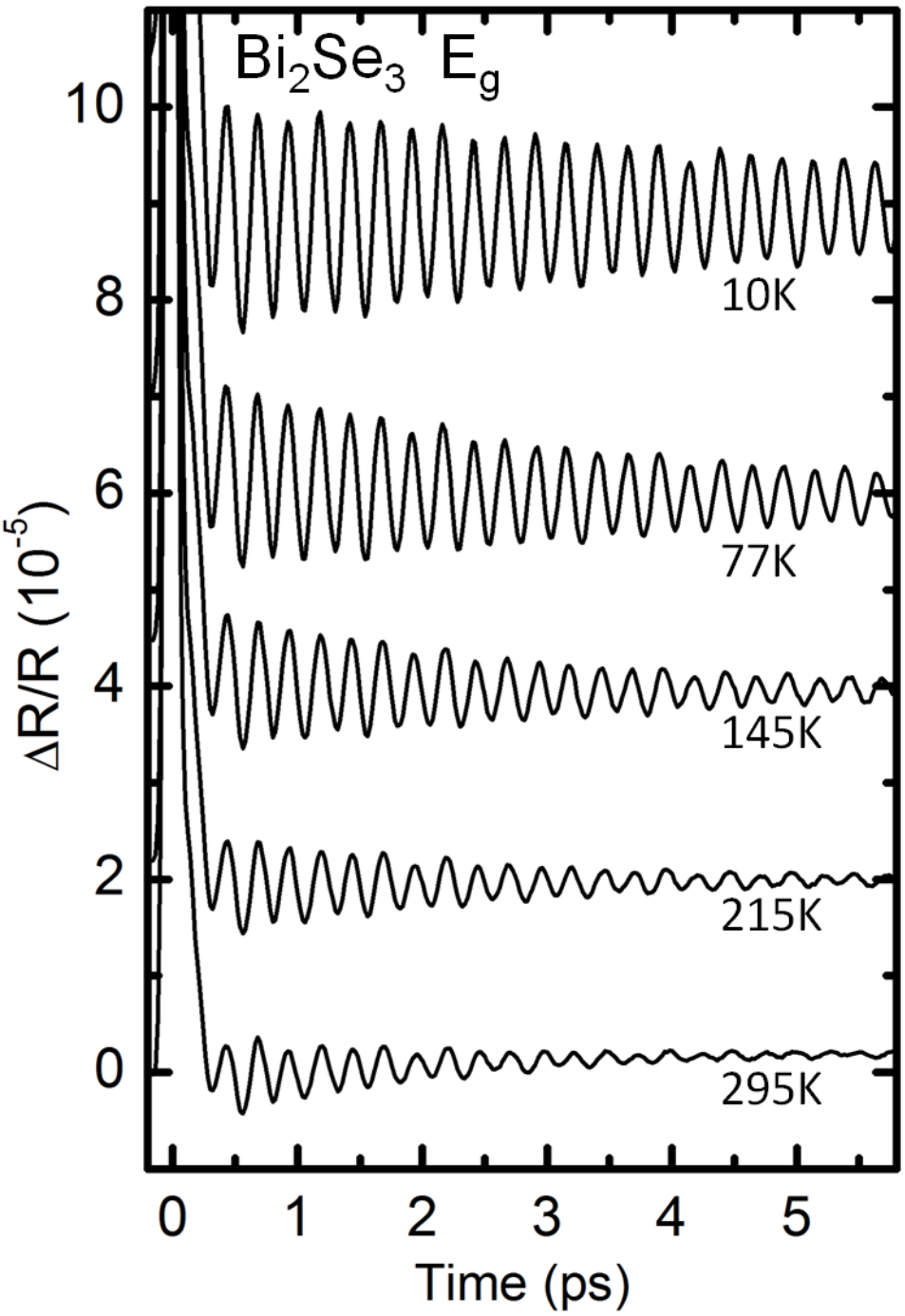

Figure 5.8. Differential reflectance data of the E_g mode in Bi_2Se_3 at different temperatures.

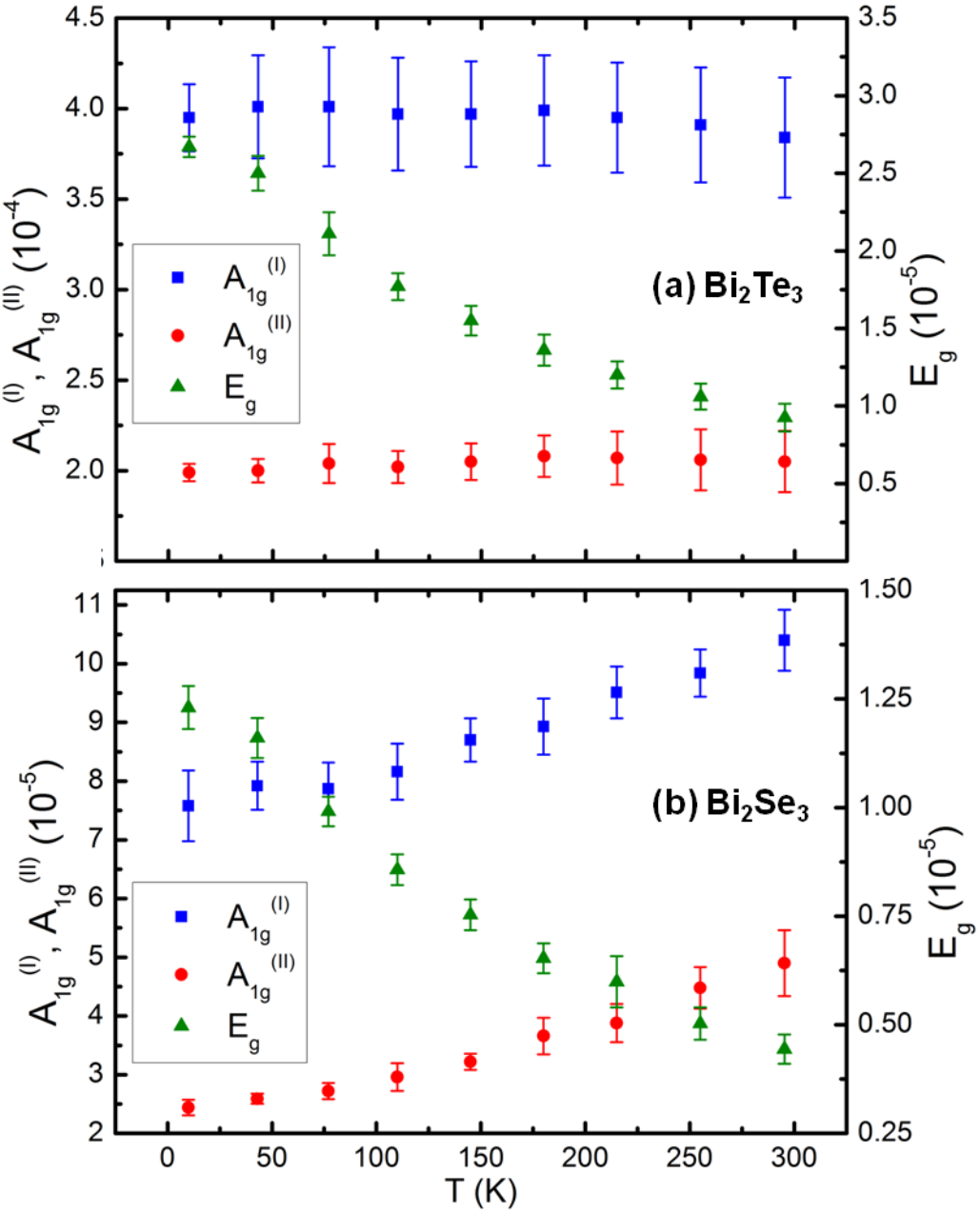

Figure 5.9. Temperature dependence of initial amplitudes of $A_{1g}^{(I)}$ (blue square), $A_{1g}^{(II)}$ (red dot) and E_g (green triangle) modes in (a) Bi_2Te_3 and (b) Bi_2Se_3. Left y-axis is for amplitudes of the two A_{1g} modes and right y-axis is for the amplitude of the E_g mode.

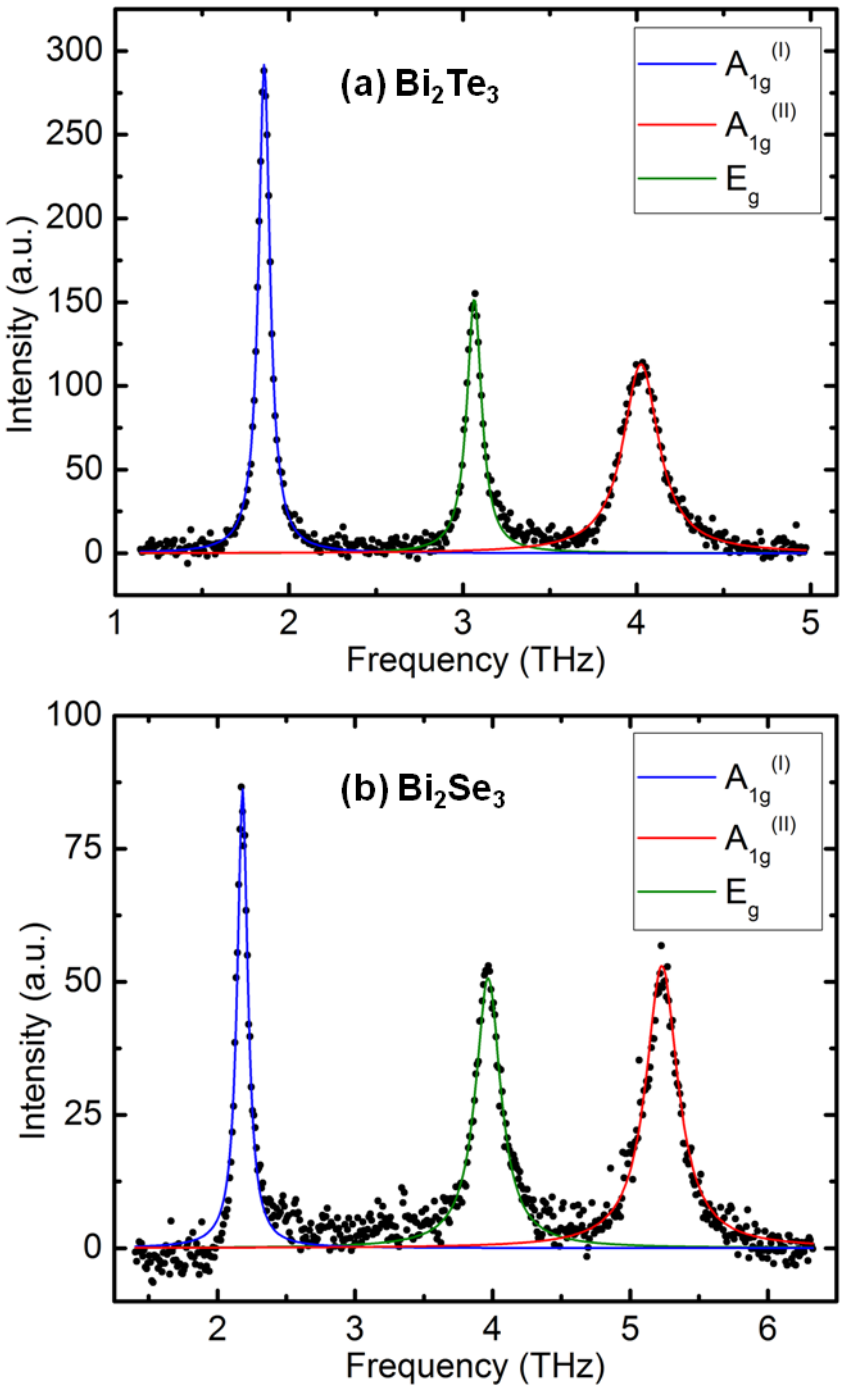

Figure 5.10. RS signals at room temperature in (a) Bi_2Te_3 and (b) Bi_2Se_3. Dots are experimental data with background removed. Blue, red and green curves are Lorentzian fits for $A_{1g}^{(I)}$, $A_{1g}^{(II)}$ and E_g peaks respectively.

I fit the oscillatory part of the signal with the linear prediction method according to Eq. (4.7). The summary of the initial amplitudes of all three modes at different temperatures for Bi_2Te_3 and Bi_2Se_3 is shown in Fig. 5.9. In Bi_2Te_3, the initial amplitudes of $A_{1g}^{(I)}$ and $A_{1g}^{(II)}$ are almost constant over the entire temperature range; the initial amplitude of E_g decreases from 2.7×10^{-5} at 10K to 9×10^{-6} at 295K. In Bi_2Se_3, the initial amplitudes of $A_{1g}^{(I)}$ and $A_{1g}^{(II)}$ exhibit slight increases from low to high temperature; for E_g, similar to the case of Bi_2Te_3, a decrease is observed from 1.2×10^{-5} at 10K to 4×10^{-6} at 295K.

The results from the Stokes RS experiment for Bi_2Te_3 and Bi_2Se_3 at room temperature are shown in Fig. 5.10. Three peaks are observed in each material, with the same frequencies as their counterparts in the pump-probe experiment. The lower frequency $E_g^{(I)}$ mode has been observed before in Bi_2Te_3 [9], but is missing in our experiment probably because of the low strength of the peak and the high laser background at small wavenumbers. I fit the spectra with Eq. (4.8). The fit results are shown in Fig. 5.10. To correct for the deviation of the peaks from Lorentzian shape at low temperatures, numerical integration of the area under each peak is also performed to get the spectrally integrated scattering cross section S_i.

5.5 Discussion of the temperature dependent experiments

Ratios in pump-probe experiments and Raman experiments are analyzed in the same way as in Chap. 4. The new feature in Bi_2Te_3 and Bi_2Se_3 compared with Sb and Bi is that the former two materials have two A_{1g} modes. I can thus use these phonon pairs to test whether the driving forces of two modes with the same symmetry have the same decay rate.

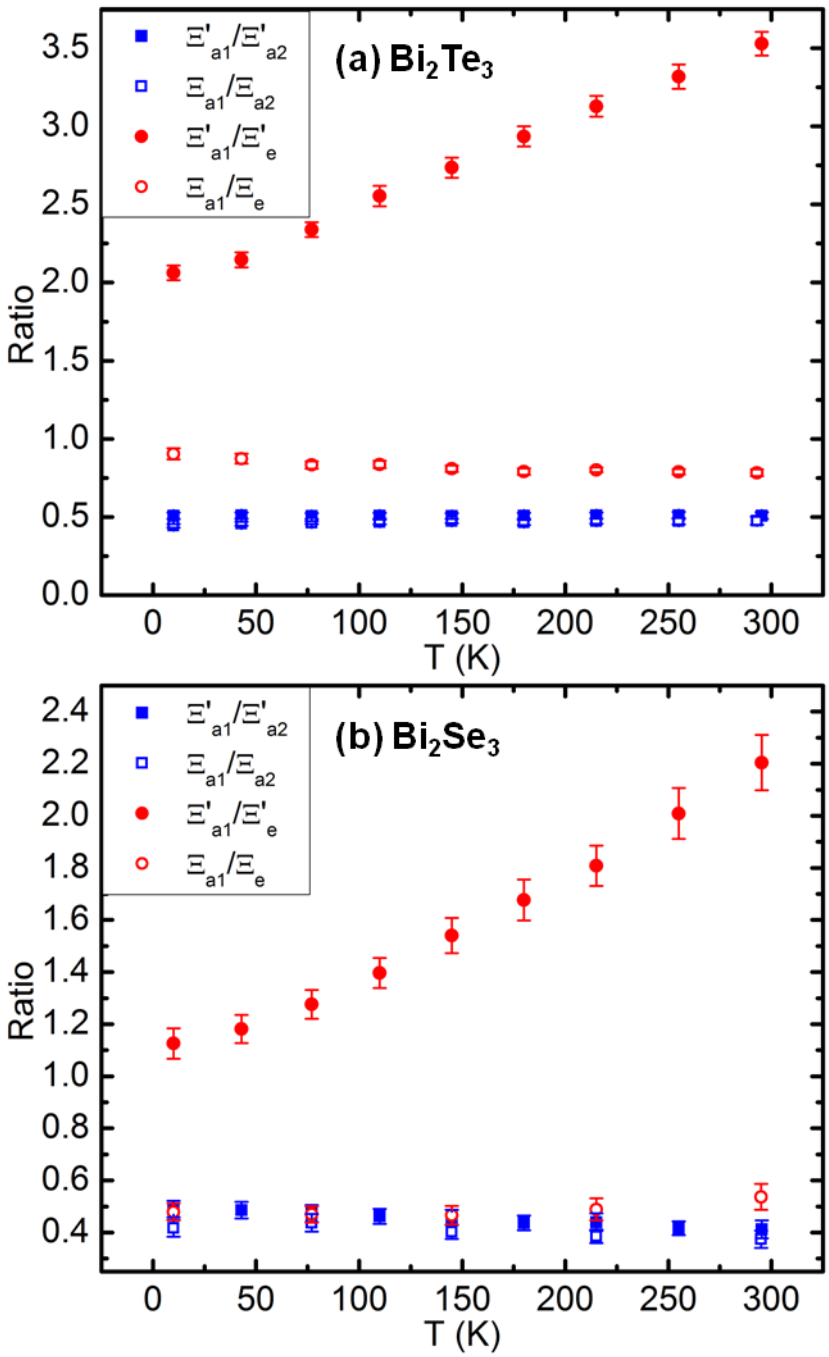

Figure 5.11. Temperature dependence of ratios between deformation potentials in (a) Bi_2Te_3 and (b) Bi_2Se_3. Blue squares are ratios between deformation potentials of $A_{1g}^{(I)}$ and $A_{1g}^{(II)}$. Red circles are ratios between deformation potentials of $A_{1g}^{(I)}$ and E_g modes. Solid symbols and notations with primes are for ratios from pump-probe experiments; hollow symbols and notations without primes are for ratios from RS experiments.

Fig. 5.11 is a summary of the ratios between the two A_{1g} modes as well as ratios between $A_{1g}^{(I)}$ and E_g in Bi_2Te_3 and Bi_2Se_3. I used shorthand notations $a1, a2, e$ to stand for $A_{1g}^{(I)}$, $A_{1g}^{(II)}$ and E_g modes. There are two notable features in the results. First, Ξ'_{a1}/Ξ'_{a2} ratios in both materials in pump-probe experiment have similar values to the corresponding Ξ_{a1}/Ξ_{a2} ratios in RS within the error range. At room temperature, Ξ'_{a1}/Ξ'_{a2} in Bi_2Te_3 is 0.51±0.02 and Ξ_{a1}/Ξ_{a2} is 0.48±0.03. In the case of Bi_2Se_3, Ξ'_{a1}/Ξ'_{a2} is 0.41±0.03 and Ξ_{a1}/Ξ_{a2} is 0.37±0.03. Over the entire temperature range, Ξ'_{a1}/Ξ'_{a2} in Bi_2Te_3 shows weak temperature dependence while Ξ'_{a1}/Ξ'_{a2} in Bi_2Se_3 shows a slight decrease from 0.49±0.03 at 10K to 0.41±0.03 at room temperature. Their counterparts in RS exhibit similar trends, keeping close track of the pump-probe ratios except for small deviations at low temperatures. These results are consistent with the theoretical prediction at $\Gamma \sim 0$, and indicate that our assumption of the long-lived driving force for the A_{1g} modes is valid.

Second, the Ξ'_{a1}/Ξ'_{e} ratios in the pump-probe experiment have different values from the corresponding Ξ_{a1}/Ξ_{e} ratios in RS, and they also exhibit different temperature-dependent behaviors. Ξ'_{a1}/Ξ'_{e} in Bi_2Te_3 shows strong temperature dependence, going from 2.06±0.05 at 10K to 3.53±0.08 at room temperature, while Ξ_{a1}/Ξ_{e} in RS only has weak temperature-dependence, with its value staying in the range 0.8~0.9. Similar behavior is also observed in Bi_2Se_3. Ξ'_{a1}/Ξ'_{e} increases from 1.13±0.06 to 2.20±0.11 and Ξ_{a1}/Ξ_{e} stays around 0.5. This implies that the assumption $\Gamma \sim 0$ does not apply to the case of coherent E_g mode.

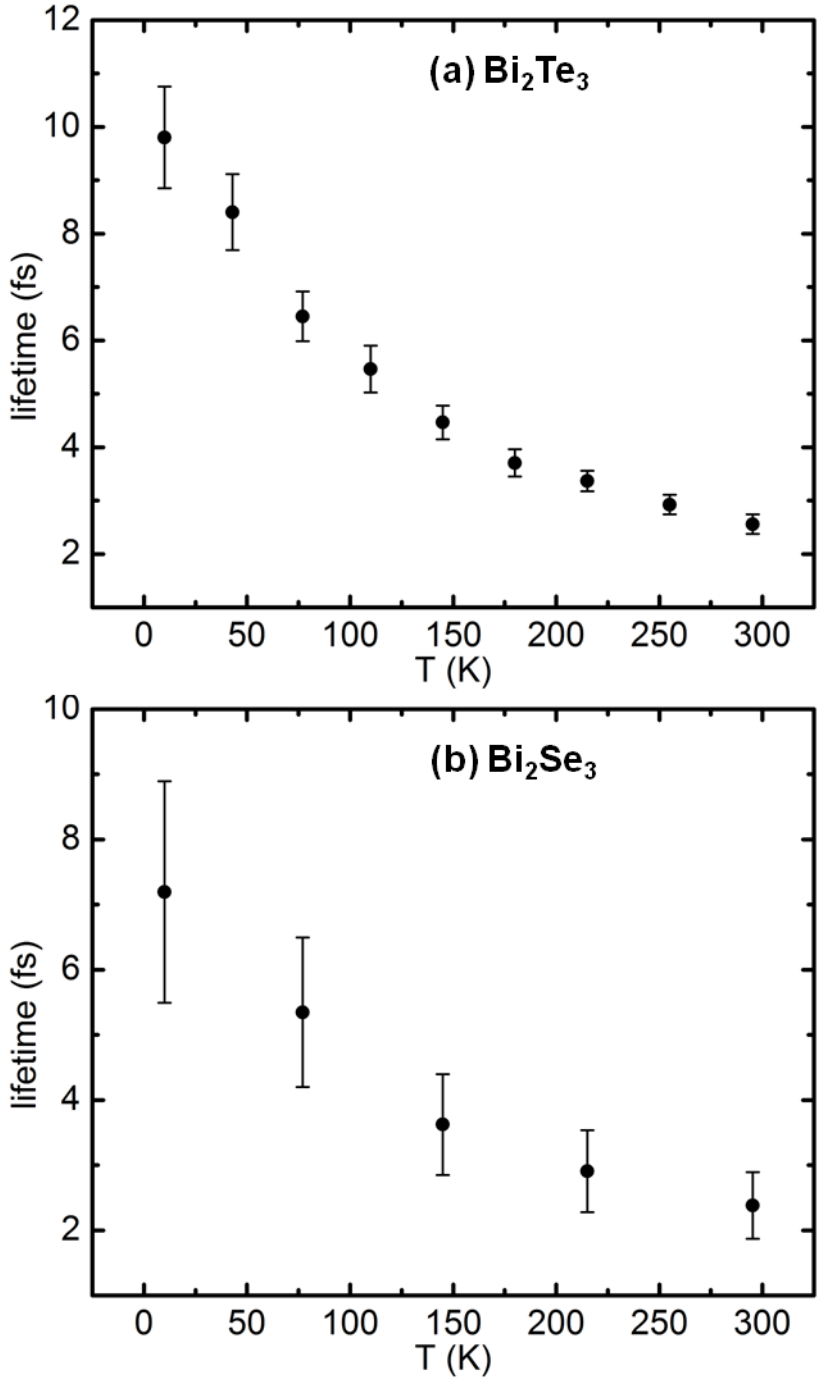

Figure 5.12. Lifetime of carrier density with E_g symmetry in (a) Bi_2Te_3 and (b) Bi_2Se_3.

Similar to Chap. 4, I can also draw information about the decay rate of the driving force with E_g symmetry. I make an approximation of Γ_{a1}~0.1/ps which is close to the interband electron-hole recombination rate in Bi_2Se_3 [21]. Fig. 5.12 shows the

temperature dependent lifetimes $1/\Gamma_e$ of charge densities with E_g symmetry. The lifetime decreases from 10±1fs at 10K to 2.5±0.2fs at room temperature in Bi_2Te_3 and from 7±2fs to 2.4±0.5fs in Bi_2Se_3. These timescales are of the same order as those in Sb and Bi.

5.6 Fabrication of ultrathin Bi_2Te_3 films

A variety of fabrication techniques have been utilized by several groups to obtain ultrathin topological insulators. Nanoribbons of Bi_2Se_3 which show smooth surfaces with 1nm step edges have been synthesized using Au-catalyzed vapor-liquid-solid mechanism [32]. Catalyst-free vapor-phase deposition on oxidized silicon substrate has produced Bi_2Te_3 and Bi_2Se_3 nanoplates with thickness as thin as 3nm [23]. The same technique is applied in obtaining an epitaxial heterostructure of a single quintuple Bi_2Se_3 layer on graphene [24]. Molecular beam epitaxy (MBE) has shown capability to grow atomically smooth Bi_2Se_3 films with controllable thickness down to one quintuple layer on Si [33]. A mechanical exfoliation technique is also employed to obtain Bi_2Te_3 flakes with thickness of 4nm [26] or thinner [27].

I used mechanical exfoliation to fabricate ultrathin Bi_2Te_3 films similar to the method used in preparing graphene [34]. An adhesive tape was used to peel off a thin layer of Bi_2Te_3 from a bulk crystal. The front side of the tape with the Bi_2Te_3 layer was then pressed against a Si wafer substrate. The Si wafer usually has a thin layer of SiO_2 on top with thickness on the order of hundreds of nanometers. I rubbed the tape from the back side and lift it off. This produced numerous thin Bi_2Te_3 pieces of a variety of thicknesses and sizes left behind on the substrate, adhering to the SiO_2 via van der Waal's force. The goal was to get pieces with thickness below 10nm, corresponding to only a few quintuples.

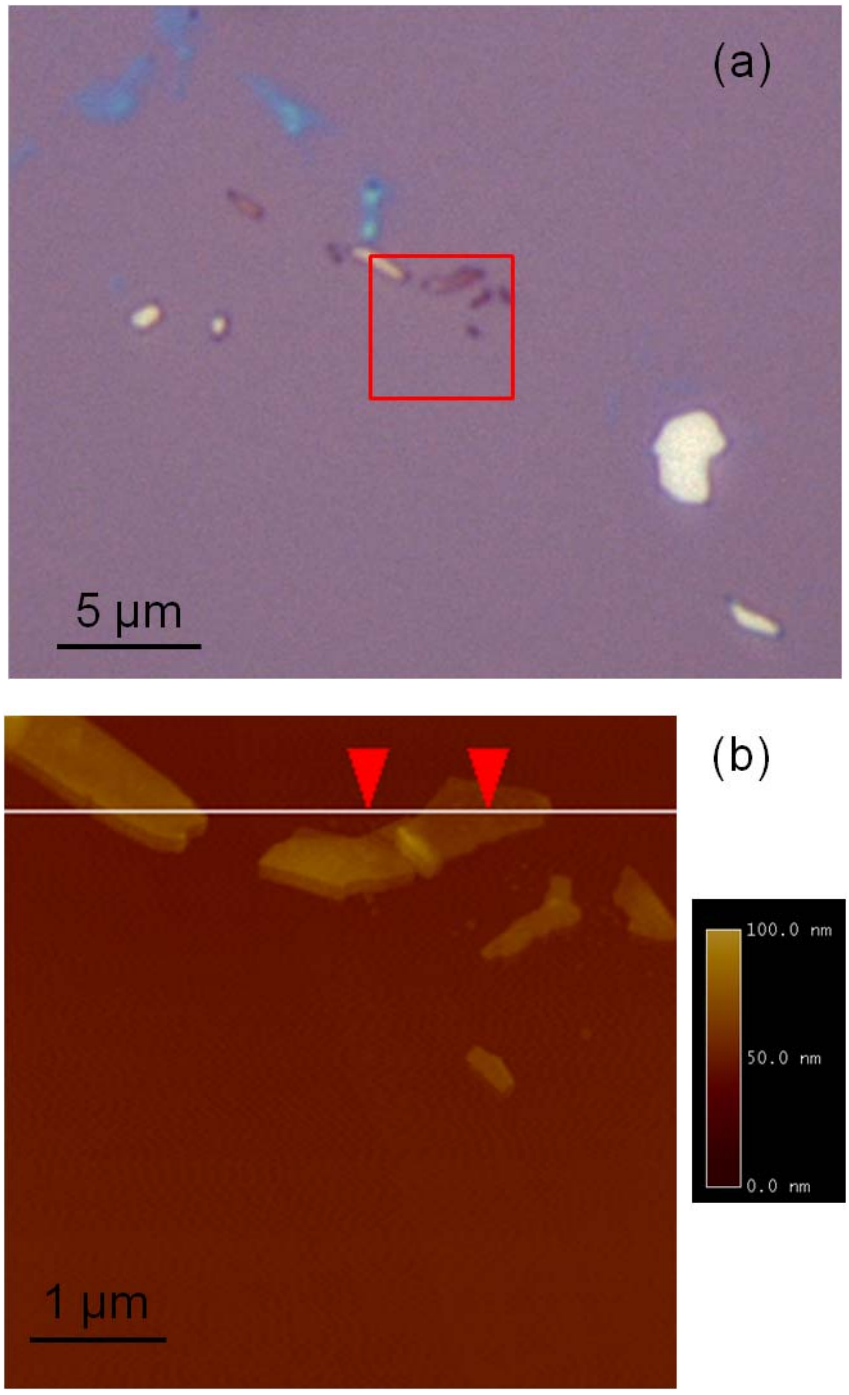

Figure 5.13. Bi_2Te_3 ultrathin films. (a) Optical image taken by a Nikon Optiphot microscope. (b) AFM image of the area inside the red square in (a). The height difference between the two points specified by the red arrows is 10nm.

In the case of graphene, which is also a layered material, an optical microscope is usually used to identify and characterize thin films. One looks for pieces with certain

color, a result due to the interference between the light reflected from the top and bottom surfaces of the graphene with a phase difference added by that thin layer [35]. Thin films with different thicknesses thus tend to demonstrate different colors, which can be employed as a rough tool to quickly identify small pieces of interest in a sea of flakes on the substrate. Once a desirable piece is located, more accurate measurements can be performed in a smaller range with an atomic force microscope (AFM) or a scanning electron microscope (SEM).

I followed similar procedures described above to fabricate and characterize ultrathin Bi_2Te_3 films on a 300nm SiO_2/Si substrate. However, due to the high absorption of Bi_2Te_3 [13], I was not able to observe ultrathin films with various colors under an optical microscope. The most common colors found on the SiO_2 surface demonstrated either highly metal-like reflective features as a bulk Bi_2Te_3 crystal, or a purple color as a bare SiO_2/Si substrate, with few other colors. The thinnest piece I managed to find has thickness of around 10nm, whose optical image shows a dark red hue. Fig. 5.13 is an example of a typical optical microscope image of our samples taken by a Nikon Optiphot and an AFM image of a piece with thickness 10nm. Sub-10nm layers remained elusive.

5.7 Optical visibility of Bi_2Te_3 ultrathin films

In order to determine an optical setup optimized for finding the missing pieces below 10nm, I used a transfer matrix method and treated the sample as a layered structure composed of air-Bi_2Te_3-SiO_2-Si. Assuming normal incidence propagating along z, the electric field in layer j is [36]

$$E = \alpha_j e^{ik_j(z-z_j)-i\omega t} + \beta_j e^{-ik_j(z-z_j)-i\omega t} \tag{5.1}$$

For adjacent layers j and $j+1$

$$\begin{bmatrix} \alpha_{j+1} \\ \beta_{j+1} \end{bmatrix} = \begin{bmatrix} P_+ & 0 \\ 0 & P_- \end{bmatrix} \cdot \begin{bmatrix} T_+ & T_- \\ T_- & T_+ \end{bmatrix} \cdot \begin{bmatrix} \alpha_j \\ \beta_j \end{bmatrix} \tag{5.2}$$

where $P_{\pm} = e^{\pm ik_{j+1}\Delta_{j+1}}$ describes the phase shift when the wave propagates through thickness Δ_j, and $T_{\pm} = (1 \pm k_j / k_{j+1})/2$ describes transmission and reflection at the interface. After multiplying all the matrices, I have

$$\begin{bmatrix} \alpha_n \\ \beta_n \end{bmatrix} = \begin{bmatrix} M_{11} & M_{12} \\ M_{21} & M_{22} \end{bmatrix} \cdot \begin{bmatrix} \alpha_0 \\ \beta_0 \end{bmatrix} \tag{5.3}$$

where indices 0, 1, 2, 3 stand for air, Bi_2Te_3 film, SiO_2 and Si respectively.

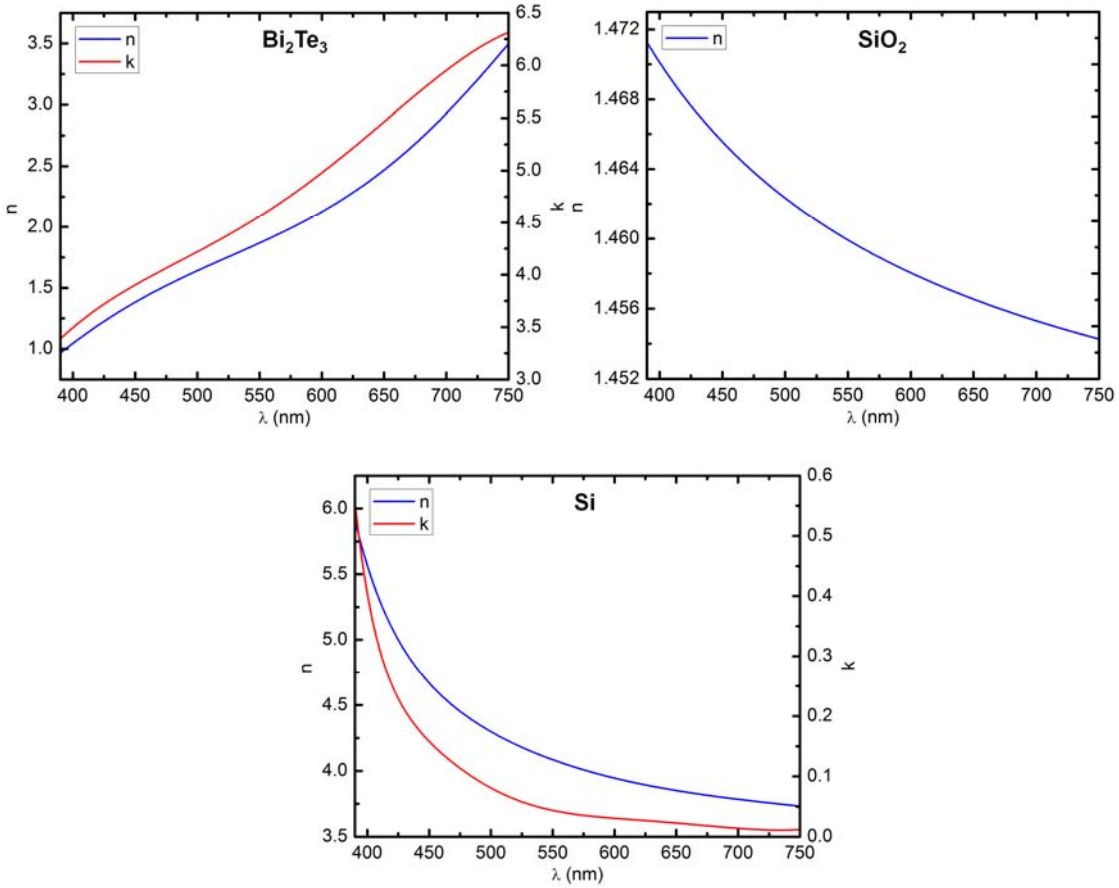

Figure 5.14. Optical constants of Bi_2Te_3, SiO_2 and Si from 390nm to 750nm.

Setting $\alpha_0 = 1$ to account for unitary incident along positive z and $\beta_3 = 0$ to account for zero incidence coming from the other side, the reflectance is

$$R = |\beta_0|^2 = |-M_{21} / M_{22}|^2 \tag{5.4}$$

The thickness of air and Si are semi-infinite, and the thickness of SiO_2 is 300nm. Si and Bi_2Te_3 have wavelength dependent complex optical constants, while SiO_2 only has a real wavelength dependent optical constant. The optical parameters were sampled from relevant references [13,37,38] and fit with polynomials, all of which are shown in Fig. 5.14 as a function of wavelength in the visible range.

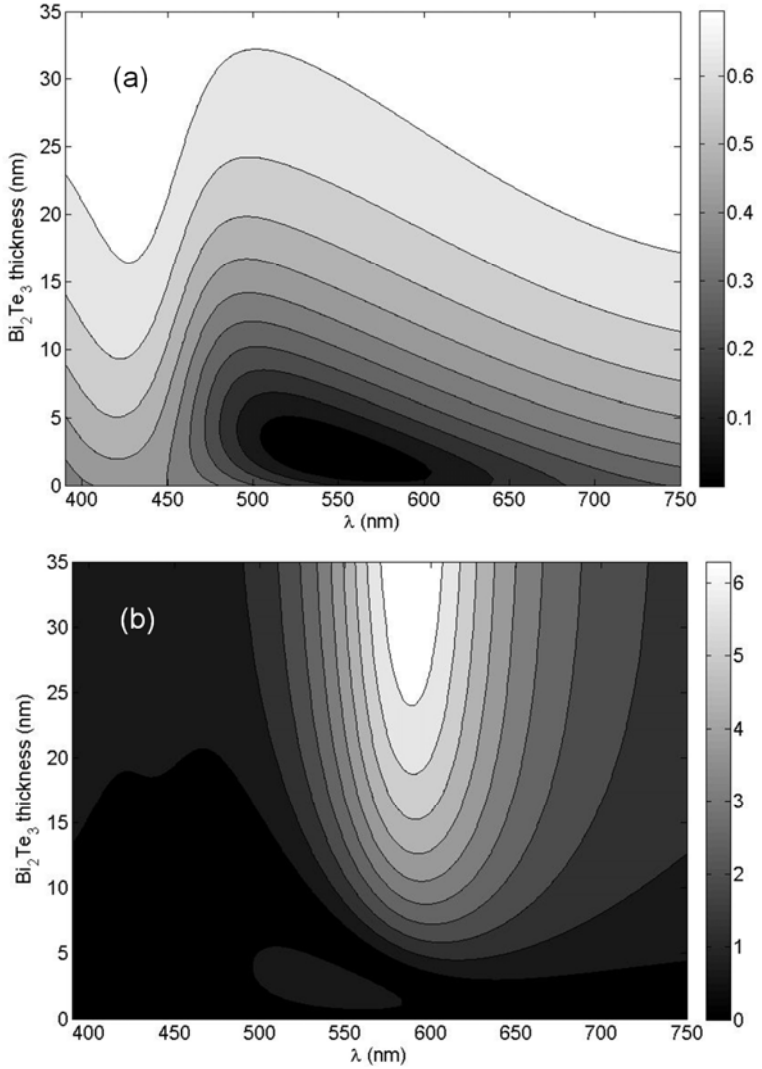

Figure 5.15. (a) Contour plot of reflectance at different wavelengths and Bi_2Te_3 thicknesses. (b) Contour plot of the absolute value of contrast at different wavelengths and Bi_2Te_3 thicknesses.

A contour plot for reflectance is shown in Fig. 5.15 (a) for Bi_2Te_3 film thickness

from 0 to 35nm and wavelength from 390nm to 750nm. The reflectance above 30nm is around 0.7, consistent with the highly reflective features of the layers commonly observed with an optical microscope. Below 30nm, the reflectance decreases over the entire optical range and the relative strength varies with wavelength. The prediction of colors at different layer thicknesses based on the RGB components is a standard and complicated process which involves considering the spectrum of the light source, the reflectance from the sample, and the response of human eyes to different colors [36]. An alternative approach is to use a narrow band filter on the reflected light and simply check its intensity. For a small piece on a large background, contrast can be defined as [39]

$$C = \frac{R(\Delta_1) - R(\Delta_1 = 0)}{R(\Delta_1 = 0)} \tag{5.5}$$

where $R(\Delta_1 = 0)$ is the background reflectance from the bare substrate. A contour plot of the absolute value of C is shown in Fig. 5.15 (b). To get high contrast, a bandpass filter around 590nm can be used to aid the observer to find ultrathin pieces down to 5nm, and a bandpass filter around 535nm can be helpful with pieces below 5nm. According to the positive sign of C in the 590nm filter case and the negative sign in the 535nm case, one should look for brighter features in the former and darker feature in the latter compared with the background. Similar analysis can be performed with different SiO_2 thicknesses to further optimize the experimental conditions.

5.8 Raman characterization of Bi_2Te_3 films

Raman spectroscopy has become a useful tool for determing the number of layers in graphene according to the lineshape or position of the G' peak [40]. I also used Raman spectrometers to characterize ultrathin Bi_2Te_3 films.

Fig. 5.16 shows the Raman spectrum of a Bi_2Te_3 ultrathin film on SiO_2/Si taken with backscattering geometry at excitation wavelength 514.5nm. Since the spot size of 100μm is much larger than the few micron size of a Bi_2Te_3 flake, signals from both the

Bi_2Te_3 film and the substrate are detected. The strongest peak around 521cm^{-1} and the small bump around 303 cm^{-1} are attributed to a first-order optical phonon and a second order transverse acoustic phonon overtone of Si respectively [41]. The much weaker signal from a Bi_2Te_3 film contains an $A_{1g}^{(II)}$ peak at 136cm^{-1}, an E_g peak at 104cm^{-1} and an additional peak at 125cm^{-1}. This extra peak has been observed in ultrathin Bi_2Te_3 films before, and is assigned to a Raman forbidden A_{1u} mode in the bulk [26].

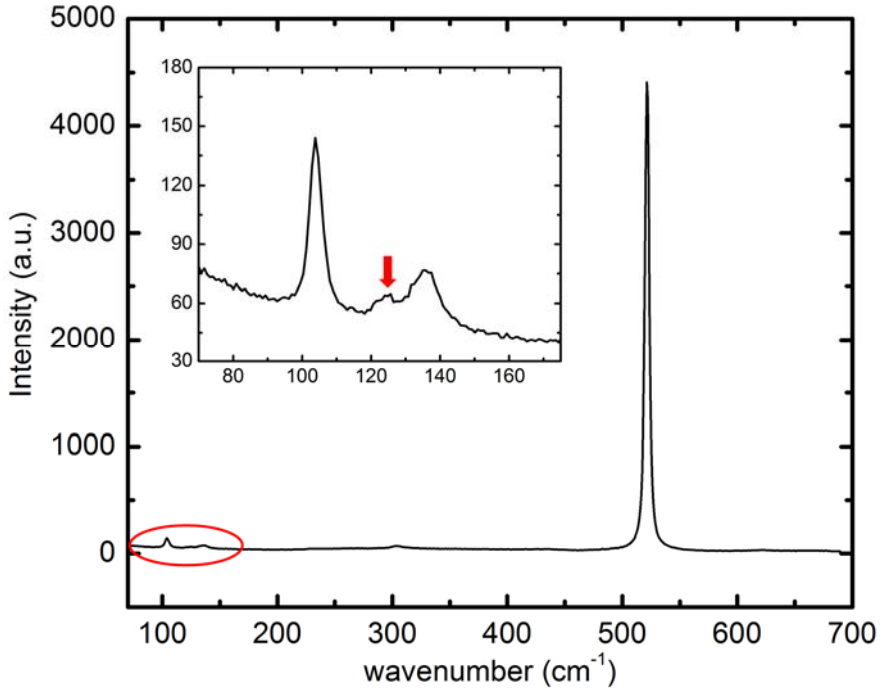

Figure 5.16. Raman spectrum of a Bi_2Te_3 ultrathin film on SiO_2/Si with excitation wavelength 514.5nm. The inset is a spectrum in the range specified by the red circle in the main figure. The red arrow indicates an additional peak.

Further study of the Raman spectra in ultrathin Bi_2Te_3 films was restricted by two factors. The first one is the size of the film. Most of the Bi_2Te_3 films fabricated by mechanical exfoliation reported so far are of the size around or below 10μm, which requires a tight focus of the incident light to guarantee that signals collected are from an area with a single and uniform thickness. That can be realized with a microscope objective lens with high magnification which functions as both the focusing lens and the

collimating lens, as in a micro-Raman spectrometer. The second factor is the availability of Bi_2Te_3 ultrathin films with various thicknesses to make systematic investigation possible. Sample fabrications with MBE [29] or other techniques to provide ultrathin Bi_2Te_3 films with uniform and controllable thickness in larger areas would solve both of the above problems.

5.9 Summary

Coherent and incoherent phonons in Bi_2Te_3 and Bi_2Se_3 have been studied under different temperatures with ultrafast laser spectroscopy and Raman spectroscopy. Similar temperature dependent behavior of the two A_{1g} modes confirms that the lifetime of the driving force with A_{1g} symmetry has $\Gamma \sim 0$. Different temperature dependent behaviors of A_{1g} and E_g coherent phonon modes give an ultrashort lifetime of the E_g driving force around or below 10fs, a range close to those in Sb and Bi.

Attempts to fabricate ultrathin Bi_2Te_3 films using mechanical exfoliation have been made. Films with thickness around 10nm were obtained but thinner ones were absent. A transfer matrix procedure was carried out to characterize the reflectance as a function of wavelength and Bi_2Te_3 thickness, so as to give guidance to improving detection schemes which can potentially increase the visibility of ultrathin films. Raman spectra for Bi_2Te_3 films were taken and an additional peak has been observed, which might be attributed to breaking of symmetry.

References

[1] H. J. Goldsmid and R. W. Douglas, British Journal of Applied Physics **5**, 386 (1954).

[2] D. A. Wright, Nature **181**, 834 (1958).

[3] S. K. Mishra, S. Satpathy and O. Jepsen, Journal of Physics: Condensed Matter **9**, 461 (1997).

[4] M. S. Dresselhaus, G. Dresselhaus, X. Sun, Z. Zhang, S. B. Cronin and T. Koga, Physics of the Solid State **41**, 679 (1999).

[5] R. Venkatasubramanian, E. Siivola, T. Colpitts and B. O'Quinn, Nature **413**, 597 (2001).

[6] J. R. Drabble and C. H. L. Goodman, Journal of Physics and Chemistry of Solids **5**, 142 (1958).

[7] J. O. Jenkins, J. A. Rayne and R. W. Ure, Physical Review B **5**, 3171 (1972).

[8] V. Wagner, G. Dolling, B. M. Powell and G. Landwehr, Physica Status Solidi (b) **85**, 311 (1978).

[9] W. Kullmann, J. Geurts, W. Richter, N. Lehner, H. Rauh, U. Steigenberger, G. Eichhorn and R. Geick, Physica Status Solidi (b) **125**, 131 (1984).

[10] H. Rauh, R. Geick, H. Köhler, N. Nücker and N. Lehner, Journal of Physics C **14**, 2705 (1981).

[11] P. Dato and H. Köhler, Journal of Physics C **17**, 3711 (1984).

[12] P. Pecheur and G. Toussaint, Physics Letters A **135**, 223 (1989).

[13] D. L. Greenaway and G. Harbeke, Journal of Physics and Chemistry of Solids **26**, 1585 (1965).

[14] H. Zhang, C. X. Liu, X. L. Qi, X. Dai, Z. Fang and S. C. Zhang, Nature Physics **5**, 438 (2009).

[15] M. Z. Hasan and C. L. Kane, Reviews of Modern Physics **82**, 3045 (2010).

[16] Y. L. Chen, J. G. Analytis, J. H. Chu, Z. K. Liu, S. K. Mo, X. L. Qi, H. J. Zhang, D. H. Lu, X. Dai, Z. Fang, S. C. Zhang, I. R. Fisher, Z. Hussain and Z. X. Shen, Science **325**, 178 (2009).

[17] Y. Xia, D. Qian, D. Hsieh, L. Wray, A. Pal, H. Lin, A. Bansil, D. Grauer, Y. S. Hor, R. J. Cava and M. Z. Hasan, Nature Physics **5**, 398 (2009).

[18] D. Hsieh, Y. Xia, D. Qian, L. Wray, F. Meier, J. H. Dil, J. Osterwalder, L. Patthey, A. V. Fedorov, H. Lin, A. Bansil, D. Grauer, Y. S. Hor, R. J. Cava and M.Z. Hasan, Physical Review Letters 103, 146401 (2009).

[19] X. L. Qi and S. C. Zhang, Physics Today **63**, 33 (2010).

[20] D. Hsieh, J. W. McIver, D. H. Torchinsky, D. R. Gardner, Y. S. Lee and N. Gedik, Physical Review Letters **106**, 057401 (2011).

[21] D. Hsieh, F. Mahmood, J. W. McIver, D. R. Gardner, Y. S. Lee and N. Gedik, Physical Review Letters **107**, 077401 (2011).

[22] X. Zhu, L. Santos, R. Sankar, S. Chikara, C. Howard, F. C. Chou, C. Chamon and M. El-Batanouny, Physical Review Letters **107**, 186102 (2011).

[23] D. Kong, W. Dang, J. J. Cha, H. Li, S. Meister, H. Peng, Z. Liu and Y. Cui, Nano Letters **10**, 2245 (2010).

[24] W. Dang, H. Peng, H. Li, P. Wang and Z. Liu, Nano Letters **10**, 2870 (2010).

[25] D. Teweldebrhan, V. Goyal and A. A. Balandin, Nano Letters **10**, 1209 (2010).

[26] K. M. F. Shahil, M. Z. Hossain, D. Teweldebrhan and A. A. Balandin, Applied Physics Letters **96**, 153103 (2010).

[27] D. Teweldebrhan, V. Goyal, M. Rahman and Z. Z. Balandin, Applied Physics Letters **96**, 053107 (2010).

[28] S. Y. F. Zhao, C. Beekman, L. J. Sandilands, J. E. J. Bashucky, D. Kwok, N. Lee, A. D. LaForge, S. W. Cheong and K. S. Burch, Applied Physics Letters **98**, 141911 (2011).

[29] Y. Zhang, K. He, C. Z. Chang, C. L. Song, L. L. Wang, X. Chen, J. F. Jia, Z. Fang, X. Dai, W. Y. Shan, S. Q. Shen, Q. Niu, X. L. Qi, S. C. Zhang, X. C. Ma and Q. K. Xue, Nature Physics **6**, 584 (2010).

[30] W. Richter, H. Köhler and C. R. Becker, Physica Status Solidi (b) **84**, 619 (1977).

[31] A. Q. Wu, X. Xu, and R. Venkatasubramanian, Applied Physics Letters **92**, 011108 (2008).

[32] D. Kong, J. C. Randel, H. Peng, J. J. Cha, S. Meister, K. Lai, Y. Chen, Z. X. Shen, H. C. Manoharan and Y. Cui, Nano Letters **10**, 329 (2010).

[33] G. Zhang, H. Qin, J. Teng, J. Guo, Q. Guo, X. Dai, Z. Fang and K. Wu, Applied Physics Letters **95**, 053114 (2009).

[34] K. S. Novoselov, A. K. Geim, S. V. Morozov, D. Jiang, Y. Zhang, S. V. Dubonos, I. V. Grigorieva and A. A. Firsov, Science **306**, 666 (2004).

[35] K. S. Novoselov, D. Jiang, F. Schedin, T. J. Booth, V. V. Khotkevich, S. V. Morozov and A. K. Geim, Proceedings of the National Academy of Sciences **102**, 10451 (2005).

[36] S. Roddaro, P. Pingue, V. Piazza, V. Pellegrini and F. Beltram, Nano Letters **7**, 2707 (2007).

[37] H. R. Philipp, in *Handbook of Optical Constants of Solids*, edited by E. D. Palik (Academic Press, Inc. , Orlando, 1985).

[38] D. F. Edwards, in *Handbook of Optical Constants of Solids*, edited by E. D. Palik (Academic Press, Inc. , Orlando, 1985).

[39] P. Blake, E. W. Hill, A. H. Castro Neto, K. S. Novoselov, D. Jiang, R. Yang, T. J. Booth and A. K. Geim, Applied Physics Letters **91**, 063124 (2007).

[40] L. M. Malard, M. A. Pimenta, G. Dresselhaus and M. S. Dresselhaus, Physics Reports **473**, 51 (2009).

[41] J. B. Renucci, R. N. Tyte and M. Cardona, Physical Review B **11**, 3885 (1975).

CHAPTER 6

Conclusions

In Chapter 4 and Chapter 5, a temperature dependent study of coherent phonons of different symmetries and the same symmetry in four materials, Sb, Bi, Bi_2Te_3 and Bi_2Se_3, have been carried out. The theory on coherent phonons has been expanded to include the scenario of a driving force with limited lifetime. Although there are many theoretical and experimental efforts before this work that investigated the generation mechanism of coherent phonons in opaque materials from various aspects [1-8], it is the first time that the influence of the lifetime of the coherent driving force on the amplitude of the coherent phonons it excites is emphasized and systematically studied to the best of my knowledge. What is more, the physical origin of the driving force has been proposed in this work, which provides insights about the significance of the role that carrier densities of different symmetries play in phonon excitation. Further, the experiments in this dissertation serve as good examples to manifest the fundamental connection between RS and ISRS. Last but not least, the extremely short-lived E_g driving force on the order of a few femtoseconds offers an approach to measure short timescales with longer laser pulses.

The next step is to study two E_g modes in the same materials, and to test whether two driving forces of E_g symmetry have equally fast decay rates. This will function as a strong experimental evidence to the theory in this dissertation, and it will also complete the entire experimental framework on the generation mechanism of coherent phonons with different symmetries.

In Chapter 4, coherent phonons in Sb have been studied at high laser fluences. The

A_{1g} and E_g modes both demonstrate chirped frequencies, nonlinear amplitudes and different curvatures for the fluence dependent decay rate. There has been theoretical works which used first-principle density functional calculation to study the effect of lattice anharmonicity and phonon softening by the electron-hole plasma on the A_{1g} phonon dynamics in Bi [9,10]. The results on A_{1g} and E_g modes in this dissertation provide plenty of experimental data for future theoretical works about phonon behaviors and anisotropic property of Sb within a wide range of fluence.

Femtosecond lasers can generate large density of photoexcited carriers which lead to bond softening, nonthermal melting and ablation [11]. The high fluence can also reveal phases which are usually not accessible under equilibrium conditions [12]. Pulsed laser has been shown to induce element segregation in semiconductor compounds such as Sb_2Te_3 [13]. These questions provoke many challenging directions for future researchers interested in high fluence phenomena. On the other hand, with the availability of ultrafast X-rays, lattice displacements can be mapped directly in real time [14], and other physical quantities such as carrier density-dependent inter-atomic potentials can be inferred from the X-ray diffraction data, too [15]. The combination of pulsed lasers and pulsed X-rays offers a powerful tool to study ultrafast phenomena in materials from a more comprehensive scope.

In Chapter 5, attempts have been made to fabricate and characterize ultrathin films of topological insulator Bi_2Te_3 with mechanical exfoliation, optical microscopy, AFM and Raman spectroscopy. The thinnest pieces found were 10nm. An additional peak was observed in spontaneous Raman scattering which may be related to the breaking of symmetry in ultrathin films. Samples with uniform and controllable thickness in larger areas are needed for further exploration in this exciting field.

In addition to the fabrication of ultrathin films, bulk topological insulators have been studied with (ARPES) [16], helium atom surface scattering (HASS) [17] and optical techniques [18] recently. Calculations predict that the surface phonon has a different

frequency from the bulk one in Bi_2Se_3 [17], as shown in Fig. 6.1. Note that at the center of Brillouin zone, the surface phonon has a lower frequency than the bulk one around 3.5 THz. This surface mode has not been observed in regular optical experiments before. By changing experimental parameters such as temperature, pressure, etc., some surface phonon modes might appear. One example is a set of high pressure Raman experiments on Bi_2Te_3 crystals, which revealed a new mode near 107cm^{-1} showing up around 3.6GPa, at the onset of electronic topological transition (ETT) [19].

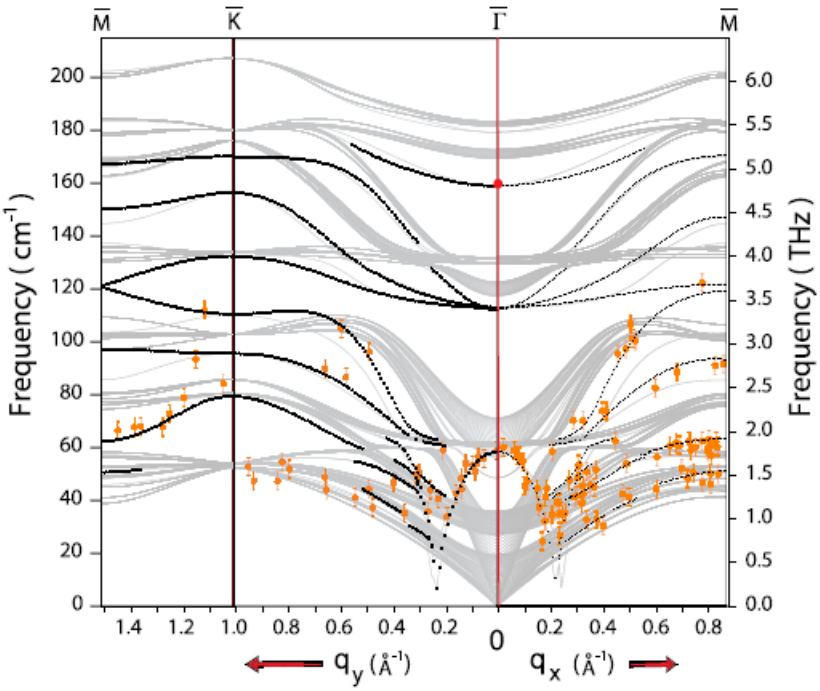

Figure 6.1. Phonon dispersion curves of Bi_2Se_3. The orange dots are HASS experimental data. The black curves are calculated surface phonon dispersion curves and the grey areas are projection of 3D bulk phonon dispersion bands on the surface Brillouin zone. From Ref. [17].

Some Raman data taken with a 780nm CW laser source are shown in Fig. 6.2. A new mode with symmetry property similar to A_{1g} mode at 153cm^{-1} has been observed at 10K, as shown in Fig. 6.2 (a). The mode gradually becomes weaker with increasing temperature and finally disappears above 100K, as shown in Fig. 6.2 (b). The property of

this new mode at low temperature and its relationship with the surface states is an interesting topic for further investigation.

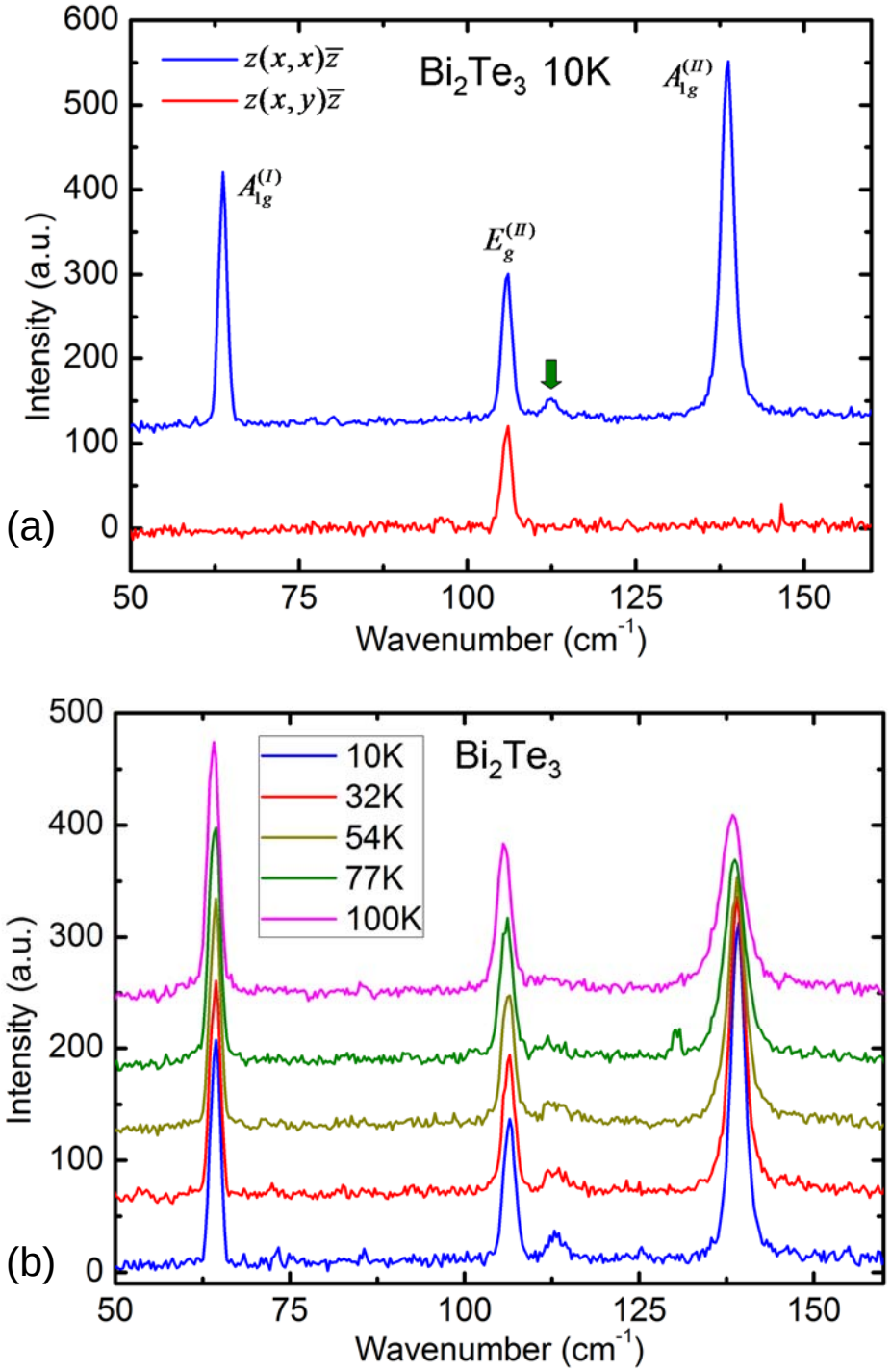

Figure 6.2. Low temperature Raman spectra of Bi_2Te_3. (a) Selection rule of a new peak indicated by the green arrow. (b) Temperature dependence of the Raman peaks.

References

[1] G. A. Garrett, T. F. Albrecht, J. F. Whitaker, and R. Merlin, Physical Review Letters **77**, 3661 (1996).

[2] T. E. Stevens, J. Kuhl, and R. Merlin, Physical Review B **65**, 144304 (2002).

[3] T. K. Cheng, S. D. Brorson, A. S. Kazeroonian, J. S. Moodera, G. Dresselhaus, M. S. dresselhaus, and E. P. Ippen, Applied Physics Letters **57**, 1004 (1990).

[4] T. K. Cheng, J. Vidal, H. J. Zeiger, G. Dresselhaus, M. S. Dresselhaus, and E. P. Ippen, Applied Physics Letters **59**, 1923 (1991).

[5] M. Hase, K. Mizoguchi, H. Harima, S. Nakashima, M. Tani, K. Sakai, and M. Hangyo, Applied Physics Letters **69**, 2474 (1996).

[6] D. Boschetto, E. G. Gamaly, A. V. Rode, B. Luther-Davies, D. Glijer, T. Garl, O. Albert, A. Rousse and J. Etchepare, Physical Review Letters **100**, 027404 (2008).

[7] H. J. Zeiger, J. Vidal, T. K. Cheng, E. P. Ippen, G. Dresselhaus, and M. S. Dresselhaus, Physical Review B **45**, 768 (1992).

[8] D. M. Riffe, and A. J. Sabbah, Physical Review B **76**, 085207 (2007).

[9] E. D. Murray, S. Fahy, D. Prendergast, T. Ogitsu, D. M. Fritz, and D. A. Reis, Physical Review B **75**, 184301 (2007).

[10] E. D. Murray, D. M. Fritz, J. K. Wahlstrand, S. Fahy, and D. A. Reis, Physical Review B **72**, 060301 (2005).

[11] D. A. Reis, K. J. Gaffney, G. H. Gilmer, and B. Torralva, MRS Bulletin **31**, 601 (2006).

[12] A. Cavalleri, Cs. Tóth, C. W. Siders, J. A. Squier, F. Ráksi, P. Forget and J. C. Kieffer, Physical Review Letters **87**, 237401 (2001).

[13] Y. Li, V. A. Stoica, L. Endicott, G. Wang, C. Uher, and R. Clarke, Applied Physics Letters **97**, 171908 (2010).

[14] A. Cavalleri, S. Wall, C. Simpson, E. Statz, D. W. Ward, K. A. Nelson, M. Rini, and R. W. Schoenlein, Nature **442**, 664 (2006).

[15] D. M. Fritz *et al.*, Science **315**, 633 (2007).

[16] Y. L. Chen, J. G. Analytis, J. H. Chu, Z. K. Liu, S. K. Mo, X. L. Qi, H. J. Zhang, D. H. Lu, X. Dai, Z. Fang, S. C. Zhang, I. R. Fisher, Z. Hussain and Z. X. Shen, Science **325**, 178 (2009).

[17] X. Zhu, L. Santos, R. Sankar, S. Chikara, C. Howard, F. C. Chou, C. Chamon and M. El-Batanouny, Physical Review Letters **107**, 186102 (2011).

[18] D. Hsieh, J. W. McIver, D. H. Torchinsky, D. R. Gardner, Y. S. Lee and N. Gedik,

Physical Review Letters **106**, 057401 (2011).

[19] G. K. Pradhan, A. Bera, P. Kumar, D. V. S. Muthu, and A. K. Sood, Solid State Communications **152**, 284 (2012).